# Czech Technical University in Prague
## Faculty of Nuclear Sciences and Physical Engineering

**DISSERTATION**

# Influence of gain medium birefringence on temporal pulse contrast in high peak power laser amplifiers

**Prague 2022**

**Ing. Josef Cupal**

## Bibliografický záznam

| | |
|---|---|
| Autor: | Ing. Josef Cupal, České vysoké učení technické v Praze, Fakulta jaderná a fyzikálně inženýrská, Katedra fyzikální elektroniky |
| Název práce: | Vliv dvojlomu aktivního prostředí na časový kontrast impulzu v laserových zesilovačů s vysokým špičkovým výkonem |
| Studijní program | Aplikované vědy |
| Studijní obor | Fyzikální inženýrství |
| Školitel: | Prof. Ing. Václav Kubeček, DrSc., České vysoké učení technické v Praze, Fakulta jaderná a fyzikálně inženýrská, Katedra fyzikální elektroniky |
| Školitel specialista: | Roman Antipenkov, Akademie věd České Republiky, Fyzikální ústav v.v.i, centrum ELI Beamlines |
| Akademický rok: | 2021/2022 |
| Počet stran: | 118 |
| Klíčová slova: | Dvojlomné aktivní prostředí, titan safír, laserový kontrast, zesilování rozmítnutých impulzů, petawattový laser |

## Bibliographic Entry

| | |
|---|---|
| Author: | Ing. Josef Cupal, Czech Technical University in Prague, Faculty of Nuclear Sciences and Physical Engineering, Department of Physical Electronics |
| Title of Dissertation: | Influence of gain medium birefringence on temporal pulse contrast in high peak power laser amplifiers |
| Degree Programme | Applied Sciences |
| Field of Study | Physical Engineering |
| Supervisor: | Prof. Ing. Václav Kubeček, DrSc., Czech Technical University in Prague, Faculty of Nuclear Sciences and Physical Engineering, Department of Physical Electronics |
| Supervisor specialist: | Roman Antipenkov, Academy of Sciences of the Czech Republic, Institute of Physics, ELI Beamlines centre |
| Academic Year: | 2021/2022 |
| Number of Pages: | 118 |
| Keywords: | Birefringent active medium, titanium-sapphire, pre-pulse contrast, chirped pulse amplification, petawatt laser |

# Abstrakt

Hlavním tématem předložené práce je časový kontrast impulzů generovaných v laserových systémech s vysokou fokusovanou intenzitou. Časový kontrast je důležitou charakteristikou petawattových laserových systémů, a spolu s fokusovatelností laserového svazku a komprimovatelností impulzu určuje použitelnost laserového systému pro interakční experimenty.
V první části práce je diskutován vliv dvojlomu aktivního prostředí v laserových systémech produkujících impulzy se špičkovým výkonem od 100 TW do 10 PW. Hlavním diskutovaným mechanizmem degradace kontrastu je vznik postpulzů v dvojlomném prostředí v důsledku rozladění polarizace svazku při dopadu na polarizačně citlivé optické prvky. Tyto postpulzy následně přispívají ke vzniku prepulzů kvůli přenosu modulace intenzity do modulace spektrální fáze během šíření impulzu prostředím s nelinearitou indexu lomu. Za účelem studia zpoždění a relativní intenzity takto generovaných prepulzů byl sestaven numerický model. V závislosti na tloušťce a typu dvojlomného aktivního prostředí vznikají prepulzy v časovém rozsahu několika desítek pikosekund před hlavním impulzem. Jejich relativní intenzita v zesilovačích s vícediskovým uspořádáním dosahuje $10^{-7}$ při rozladění jednotlivých disků o úhel menší než $1^{\circ}$. Nehomogenita směru optické osy v dvojlomném aktivním prostředí vede ke vzniku prepulzů i v případě dokonalého vzájemného nastavení jednotlivých disků. Několik titan safírových disků s aperturou 10 cm bylo charakterizováno metodou měření mezi zkříženými polarizátory, která byla uzpůsobena pro měření orientace optické osy v jednoosých krystalech v krystalografickém řezu a. Tato měření odhalila nehomogenitu směru optické osy v důsledku růstových defektů při pěstování krystalů. Oblast nehomogenity pokrývala přibližně 5% plochy disku, přičemž odchylka směru optické osy v rovině disku dosahovala hodnoty $0.7^{\circ}$. Přítomnost nehomogenit směru optické osy vede ke snížení časového kontrastu v důsledku generace prepulzů s relativní intenzitou $10^{-9}$ i při dokonalém vzájemném nastavení jednotlivých disků. Dopad přítomnosti nehomogenity na časový kontrast je možné snížit umístěním nehomogenního disku do jedné z krajových pozic ve vícediskovém uspořádání.
Ve druhé části práce jsou popsána jednotlivá zlepšení časového kontrastu laseru L3-HAPLS. Původní nedokonalosti v nanosekundovém časovém rozsahu před hlavním impulzem byly charakterizovány a odstraněny, případně sníženy na přijatelnou úroveň. Zlepšení umožnilo částečně uvést do provozu výzkumná uspořádání v experimentálních halách E3 a E4 centra ELI Beamlines. V Beta zesilovači byly odhaleny značné ztráty způsobené rozptylem na nedokonalostech magneto-rheologického opracování povrchu titan safírových krystalů. Tyto ztráty dosahují 10.8% na každý průchod hlavou zesilovače a významně snižují výstupní energii zesilovače. Díky rozptylu je v zesilovači generován prepulz se zpožděním -56.4 ns vzhledem k hlavnímu impulzu. Dopad tohoto prepulzu na interakční experimenty byl snížen na přijatelnou úroveň úpravou multiplexování průchodů zesilovačem. Dalším vylepšením časového kontrastu laseru L3-HAPLS byla úprava potlačení prepulzů z prvního zesilovače front-endu optimalizací XPW. Zesílená spontání emise a její nárůst před hlavním impulzem byly sníženy optimalizací druhého zesilovače front-endu a instalací rychlé Pockelsovy cely. Díky zmíněným úpravám byla zvýšena dosažitelná energie urychlených protonů v experimentu E4-ELIMAIA z 3 MeV na více než 24 MeV.

# Abstract

The main topic of this thesis is the pre-pulse contrast of high-focused-intensity laser systems. The pre-pulse contrast is an important quality of petawatt laser systems, defining their utility for the laser-matter interaction experiments and applications.

In the first part, the impact of birefringence of the gain medium in the amplifiers of laser systems producing pulses with peak power of 100 TW to 10 PW is studied. The main mechanism of the contrast degradation is from generation of post-pulses in the birefringent gain medium due to misalignment of the pulse polarization on polarizing optical components and in the gain medium, which are subsequently transformed to pre-pulses due to transfer of intensity modulation to the spectral phase of the pulse through nonlinearity of refractive index. A numerical model is developed and used to evaluate the delay and relative intensity of the pre-pulses. Depending on the thickness and type of the gain medium, the pre-pulses appear within few tens of picoseconds from the main pulse. The relative intensity in amplifiers with multi-slab configuration can be as high as $10^{-7}$ for misalignment of the individual slabs smaller than 1°. Inhomogeneity of the crystallographic c-axis direction of the birefringent gain medium degrades the pre-pulse contrast even with ideal crystal alignment. A cross-polarized imaging method was extended to the measurement of the local c-axis direction in the plane of large aperture a-cut Ti:sapphire crystals. Several 10 cm diameter crystals were characterized using this method, showing inhomogeneity of the c-axis direction due to crystal growth imperfections. The relative area of the c-axis inhomogeneity was 5% of the slab area, and the deviation of the c-axis direction in the plane of the slab was 0.7°. The presence of such crystal domains leads to generation of pre-pulses with relative intensity up to $10^{-9}$ in ideally aligned systems. The impact of the domains can be minimized by positioning of the inhomogeneous slabs at the outer positions in the multi-slab laser head.

In the second part of the thesis, the improvement of the pre-pulse contrast of the L3-HAPLS laser system is described. The initial nanosecond pre-pulse contrast defects were identified and optimized, enabling the commissioning of the experimental setups in the E3 and E4 experimental halls of the ELI Beamlines facility. Significant scattering loss was identified on the crystals of the Beta amplifier head, originating from imperfection of magneto-rheological finishing. The loss of 10.8% per amplification pass degrades the performance of the amplifier by reducing the achievable output pulse energy and producing a pre-pulse at 56.4 ns before the main pulse. The impact of this pre-pulse was reduced to acceptable level by adjustment of the amplifier multiplexing. Another improvement was made on the reduction of nanosecond pre-pulses from the front-end by improving the performance of the XPW stage. The rising nanosecond pedestal from ASE of the second front-end amplifier was reduced by optimization of the amplifier and by installation of fast pulse picker. The reported improvements consequently increased the achievable proton energy of the E4-ELIMAIA accelerated proton source from 3 MeV to >24 Mev.

# Acknowledgements

I would like to acknowledge the support of Thomas Spinka, Emily Sistrunk, and Petr Hříbek, and thank them for their guidance and for the long and fruitful technical discussions. I would also like to thank to my supervisor, professor Václav Kubeček, and to my advisor, Roman Antipenkov, for their patience and for their support throughout my studies. The work on the L3-HAPLS laser system was a great experience thanks to the great team of people, namely Jiří Thoma, Lucia Koubíková, Jeff Jarboe, Samuel Buck, Jiří Weiss, Petr Szotkowski, Davorin Peceli, Martin Cuhra, and Tárcio de Castro Silva. I would also like to appreciate the technical leadership of Daniel Kramer and Bedřich Rus.
A special thanks belongs to my mother Jiřina, father Josef and brother Ondřej for supporting me, and to my two dearest friends Michal Rychlík and Zbyněk Hubka for asking the right questions that stimulate my interest and broaden my horizons. They have all undoubtedly contributed to the quality of my work and to my personal development.

I would also like to acknowledge the following funding:

| Funding agency | Grant number |
|---|---|
| Ministerstvo školství, mládeže a tělovýchovy | LM2018141 |
| Ministerstvo školství, mládeže a tělovýchovy | CZ.1.05/1.1.00/02.0061 |
| Ministerstvo školství, mládeže a tělovýchovy | CZ.1.07/2.3.00/20.0091 |
| Ministerstvo školství, mládeže a tělovýchovy | CZ.02.1.01/0.0/16_019/0000789 |
| České vysoké učení technické v Praze | RVO68407700 |

# Declaration

I hereby declare that except where specific reference is made to the work of others, the contents of this dissertation are original and have not been submitted in whole or in part for consideration for any other degree or qualification in this, or any other university. This dissertation is my own work and contains nothing which is the outcome of collaboration with others, except as specified in text and Acknowledgements.

Josef Cupal

March 2022

# Contents

# List of Figures

# List of Acronyms

| | | |
|---|---|---|
| **AOPDF** | acousto-optic programmable dispersive filter | 48 |
| **ASE** | amplified spontaneous emission | 12 |
| **CPA** | chirped pulse amplification | 8 |
| **DFT** | discrete Fourier transform | 69 |
| **GDD** | group delay dispersion | 23 |
| **HCF** | hollow-core fibre | 95 |
| **HR** | high reflectivity | 17 |
| **LIDT** | laser-induced damage threshold | 108 |
| **LLNL** | Lawrence Livermore National Laboratory | 18 |
| **MOPA** | master oscillator power amplifier | 83 |
| **MRF** | magneto-rheological finishing | |
| **NIF** | National Ignition Facility | 14 |
| **OAP** | off-axis parabola | 12 |
| **OPA** | optical parametric amplification | 15 |
| **OPCPA** | optical parametric chirped pulse amplification | 15 |
| **PMT** | photomultiplier tube | 104 |
| **SPM** | self-phase modulation | 28 |
| **TASE** | transverse amplified spontaneous emission | 86 |
| **TOXC** | third-order cross correlator | 17 |
| **XPM** | cross-phase modulation | 28 |
| **XPW** | cross-polarized wave generation | 17 |

# Introduction

Since the first successful demonstration of a ruby laser by Thomas Maiman in 1960, the field of laser physics and engineering has undergone tremendous evolution. A variety of lasers have been developed and constructed for a large range of applications in industry, scientific research, telecommunication, medicine, military, and other areas. Further developments in laser technology increase the range of available laser light parameters, and consequently enable new applications for lasers.

A range of applications in fundamental and applied research utilizes interaction of high-intensity laser pulses with matter in solid or gaseous phase in ultra-relativistic regime (intensity $> 10^{18}$ W/cm$^2$) [1–5, B3]. The matter is positioned in a form of a target (thin foil, gas jet, etc.) at the focal plane of an off-axis parabola (OAP). The OAP focuses a laser pulse with high peak power to a spot with the size of several $\mu$m [6]. As a result, the incident laser pulse converts the irradiated matter of the target into high-temperature dense plasma which is a source of x-ray radiation and accelerated particles [7–10].

The interaction of the high intensity laser pulse with the target may be impacted by any modification of the target by light arriving before the primary pulse [11, 12]. Any light with sufficient intensity, typically $> 10^{10} - 10^{12}$ W/cm$^2$ [13], ionizes the target and generates pre-plasma, modifying or completely destroying the target. The target may be also modified by thermal effects from longer exposure to light below the ionization threshold. The final impact of pre-pulse light on the interaction depends on delay with respect to the primary pulse, on the intensity of the pre-pulse, on the parameters of the target, and on the type of experiment.

Many sources of the pre-pulse contrast degradation in high-focused-intensity laser systems have been identified and well understood. Design and specification of the optical components plays an important role in the development of petawatt-class laser systems. Using high-surface-quality mirrors and diffraction gratings can reduce coherent pedestals from stretcher optics [14]. Minimizing parasitic reflections reduces the impact of mirroring of post-pulses to pre-pulses [15]. Careful design of amplifiers and optimization of geometry of the gain medium can reduce the impact of amplified spontaneous emission (ASE) [16]. Other sources of contrast degradation and their impact on the performance of high-focused-intensity laser systems are not yet fully understood.

The main goal of this thesis is to investigate the impact of birefringence of the gain media most commonly used in the current high-focused-intensity laser systems on the pre-pulse contrast of the output pulse. The main criteria for evaluation of the impact are the time range within which the contrast imperfections appear, and their relative intensity with respect to the main pulse. The results of this work should provide better understanding of how the contrast defects from birefringence can be minimized during design and development of high repetition rate petawatt-class laser systems.

The method that was selected for fulfilling the main goal of the thesis was analytical and numerical evaluation, combined with experimental verification and benchmarking of the numerical models.

The secondary goal of the thesis is to provide initial improvements of the pre-pulse contrast of the L3-HAPLS laser system after installation in ELI Beamlines and integration with petawatt compressor. The approach to reaching this goal includes evaluation of the current pre-pulse contrast by measurement, identification of origin of pre-pulses and pedestals, selection of the mitigation method, implementation of the improvement, and verification with proton acceleration experiment in the E4 experimental hall of the ELI Beamlines facility.

The content of the thesis is separated into six chapters. The first part of the thesis provides the required theoretical background. The first chapter contains the introduction into the topic and summary of the current state of the development of high-focused-intensity laser systems. Chapter 2 focuses on the description of properties of the pulse amplified in CPA amplifiers. The mathematical description of the stretched pulse and the impact of dispersion are discussed, followed by the description of pulse polarization and the mathematical approach to calculating the impact of polarizing optical components on the polarization of the pulse. At the end of chapter 2, the primary nonlinear optical effects occurring during the amplification of the CPA pulse are discussed. Chapter 3 contains the description of the mechanism of degradation of the pre-pulse contrast due to birefringence of the gain medium. Generation of post-pulse in birefringent medium is explained, and mathematical description of the mirroring of such post-pulse to pre-pulses is provided. Attention is given to the impact of individual optical components and parameters of the laser beam on the resulting relative intensity contrast of the pre-pulses.

The practical part of the thesis consists of three chapters. Chapter 4 is dedicated to the description of the measurement of local orientation of the c-axis in large aperture Ti:sapphire crystals. The extended cross-polarized imaging technique used for the measurement and the method for extracting the c-axis orientation data are discussed, followed by the results of the measurements. Chapter 5 contains an extensive description of the implementation of numerical model which was used to evaluate the impact of gain medium birefringence on the pre-pulse contrast. The results of this evaluation are summarized at the end of this chapter. Chapter 6 is dedicated to the summary of the effort to improve the pre-pulse background of the L3-HAPLS laser system. This chapter includes the description of the initial pre-pulse contrast and the changes to the amplifier system that were implemented in order to limit the pre-pulses and ASE background.

The main results and the impact of the work performed within this thesis are provided in the Conclusions chapter at the end of the thesis.

# Chapter 1

# Current state of high-focused-intensity lasers development

The high intensity of light required for reaching laser-matter interaction in ultra-relativistic regime is typically achieved by focusing a pulse with high peak power to a very small spot. Since the peak power is the ratio of the pulse energy to its duration, such lasers must by definition generate pulses that are energetic and very short. The former is achieved by amplification of the initially weak pulses from a mode-locked [17–19] laser oscillator in multiple amplification stages. The latter requires utilizing gain materials with large gain bandwidth to support amplification of the wide spectrum needed for a very short pulse. Safe amplification of the pulse to energies required for achieving high peak power is possible with CPA [20]. In 1996, the peak power of 1 petawatt was demonstrated for the first time [21]. The unique properties and applications of the pulses with peak power $> 0.1$ PW have driven the development of the required technology. Currently, there are approximately 90 laser systems around the world delivering peak power greater than 100 TW in operation, under construction, or in the conceptual phase [22]. An extensive overview of the progress in the field of petawatt-class lasers is summarized in [23, 24].

The state of the art petawatt-class laser systems are capable of producing optical pulses with peak power of up to 10 PW [25] and focused intensity of $1.1 \cdot 10^{23}$ W/cm$^2$ [6]. The repetition rate of the current petawatt-class systems is typically below 1 Hz, and in most cases such systems are single-shot. The main trends in the development of petawatt-class lasers include the increase of peak power to enable new scientific applications, and the increase of repetition rate in order to transform the high-intensity particle and x-ray sources generated in scientific experiments into true applications.

Increasing the peak power requires amplification to higher energies and/or decreasing the output pulse duration. Increasing the energy is demanding due to technological limitations on size of the optical components, and a multi-beam approach may be required, similar to the National Ignition Facility (NIF) facility [24]. A significant challenge of this approach will be the synchronization of the femtosecond pulses from the individual beams. Decreasing the pulse duration requires manufacturing and use of optical components with performance optimized for larger bandwidth, optimization of the dispersion in the CPA system over larger frequency range, optimizing frequency-dependent gain and loss, and limiting spatio-temporal couplings.

The increase of repetition rate of the petawatt-class lasers mainly requires an improvement in thermal management and overall conversion efficiency. The excess heat per shot stored in the laser system needs to be removed by cooling before the next shot in order to maintain thermal stability of the system and avoid performance degradation due to gradual overheating. In both conventional and OPCPA based systems, the pump lasers are typically the limitation for achievable repetition rate. The current systems operating at one shot per 20 minutes or longer typically utilize flash lamps in their pump lasers. New systems are being built which utilize the diode pumping technology for its better efficiency and improved thermal management [26, B4]. Additionally, operating the amplifiers of the repetition rate petawatt-class system requires optimization of the wavefront properties to the new thermal equilibrium, which is different from the single-shot operation.

## 1.1 Common architectures of high-focused-intensity lasers

High-focused-intensity laser systems rely on the CPA technique. The pulse is stretched in time before amplification, reducing the intensity of the pulse and consequently minimizing nonlinear optical effects and risk of damage to the optical components. After amplification, the pulse is compressed close to its original pulse duration. Stretcher and compressor introduce large amount of dispersion to provide the stretch factors of $10^3$-$10^5$ typically used. The amount of dispersion in the stretcher must match the dispersion of the compressor and the optical components passed during the amplification in order to ensure re-compression of the pulse. The most commonly used stretcher and compressor architectures are the Offner type stretcher [27] and Treacy type compressor [28], utilizing reflective diffraction gratings. Other types of stretchers and compressors may be used, e.g. for the first stage of double CPA architectures.

For laser systems generating high-energy pulses shorter than 100 fs, typically either Ti:sapphire [29,30] is used as a gain medium, or the optical parametric chirped pulse amplification (OPCPA) technique is employed [31]. Laser amplifiers utilizing neodymium and ytterbium doped glasses and crystals, often combined with OPCPA pre-amplifiers, are used in petawatt systems producing pulses longer than 100 fs [32–35]. Within the last decade, the peak power of pulses generated by PW-class laser systems has increased from ≈1 PW to over 10 PW [24, 36–41].

The amplification of the stretched pulse is realized either by conventional laser amplifiers with gain from stimulated emission, or by nonlinear optical process of optical parametric amplification (OPA). The conventional laser amplifiers require the seed pulse to pass through the gain medium several times in order to efficiently extract the stored energy. Common amplifiers utilize either regenerative or multi-pass configuration. The former requires locating the gain medium inside an optical resonator. The pulse is injected to the resonator cavity through a polarizer, and a Pockel's cell is used to control the polarization of the pulse in order to lock the pulse inside the resonator cavity. The number of amplification passes can be adjusted by the high voltage of the Pockel's cell. Once the maximum amplification is achieved, the pulse is extracted from the amplifier cavity. The multi-pass amplifier configuration uses mirrors that do not form a resonator to return the pulse to the gain medium. The pulse is amplified by a fixed number of amplification passes defined by the beam path or by polarization multiplexing.

In stimulated emission process, the energy transfer from the pumping to the amplified pulse is a two step process. The energy is first stored in the gain medium, and then extracted by the amplified pulse. In OPA, the energy is transferred to the amplified pulse directly through the nonlinear optical interaction [42]. The nonlinear optical crystal used for OPA facilitates the optical nonlinearity, and allows for optimization of phase matching required for efficient amplification. Since the gain is present only during the propagation of the pump pulse through the nonlinear crystal, each pass through nonlinear crystal requires a dedicated pump pulse. The single pass gain in OPA can be higher than in conventional laser amplifiers.

In order to amplify the pulse from the nJ energies at the output of the oscillator to the range of J to kJ needed for reaching petawatt peak power, several stages of amplification are required. As the energy of the pulse increases, the size of the beam in the amplifiers and the size of the gain medium needs to be increased. The beam is expanded between individual amplifiers by refractive or reflective telescopes. The telescopes typically provide imaging of the spatial intensity beam profile and wavefront from one amplifier to the other.

## 1.2 Pre-pulse contrast

One of the key characteristics of every high-focused-intensity laser system is its pre-pulse contrast. Most commonly, the pre-pulse contrast is expressed as the relative intensity of light appearing within the laser beam before the main pulse. The pre-pulse contrast defined in this way is referred to as the intensity contrast. Alternatively, energy contrast can be expressed as a ratio of the pre-pulse energy to the energy of the main pulse. The contrast of the laser system has crucial impact on the laser-matter interaction experiments and applications. Pre-pulses with enough energy or intensity can modify the target before the arrival of the main pulse, altering the interaction or making it impossible. The two main mechanisms of pre-pulse light influencing the interaction are thermal and ionization. The thermal effects are present if the pre-pulse light has intensity below the threshold for ionization of the target material, but the integrated energy of the pre-pulse is significant. Above the ionization threshold the pre-pulse produces pre-plasma. The interaction of the main pulse is then influenced by the presence of the pre-plasma, and the impact depends, among others, on the amount of time the pre-plasma has to expand.

Illustration of the typical intensity contrast at different times before the main pulse is shown in figure 1.1. The typical high-focused-intensity laser system generates pre-pulse light that can be separated into several categories [24]. Individual pre-pulses produced from insufficient suppression of the oscillator pulse train and by nonlinearity-induced pre-pulses from multiple-reflection post-pulses [15] are typically present within hundred nanoseconds before the main pulse. The delay of such pre-pulses depends on the extra path length from multiple reflections, and on the repetition rate of the oscillator. Pedestals produced by ASE from laser amplifiers based on stimulated emission [16] and by parametric fluorescence from amplifiers utilizing OPCPA [43] may extend over the range of tens of nanoseconds. In the picosecond range, coherent pedestals from scattering of stretcher mirrors and gratings are dominant [14]. Such pedestals are typically symmetrical before and after the main pulse, and may extend over tens or hundreds of picoseconds.

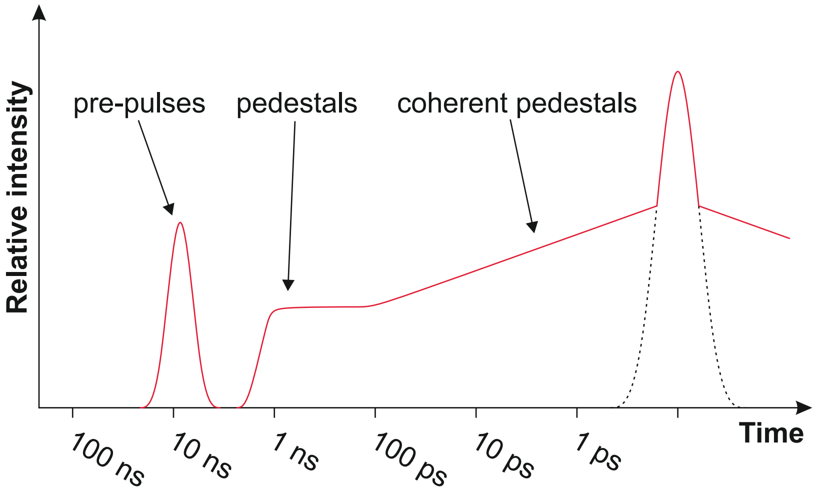

**Figure 1.1:** Illustration of typical pre-pulse contrast defects in high focused intensity lasers.

### 1.2.1 Methods for measurement of the pre-pulse contrast

Measuring the pre-pulse contrast and interpreting the measurements is not always straight forward. A first order evaluation can be performed using a photodiode and oscilloscope. This method is relatively simple in principle, since it requires only inserting the photodiode in the beam - typically a leak through high reflectivity (HR) mirror. Any pre-pulses with high enough energy for the dynamic range of the photodiode are readily visible. The disadvantages of this method are nonlinearity of the photodiode response and low dynamic range. The dynamic range required for lasers with 1-10 PW peak power is $10^{10}$-$10^{12}$, while the maximum dynamic range of a photodiode is $10^{7}$-$10^{8}$. To achieve the highest possible dynamic range, the photodiode needs to be saturated by the main pulse. Relative energy contrast can be measured using calibrated neutral-density filters and attenuating the main pulse to the same signal level as the pre-pulse. The interpretation of the measurement by photodiodes can be ambiguous, since the photodiode is highly sensitive and easily measures scattered signals from the surroundings.

A more rigorous method for the measurement of intensity contrast is a scanning third-order cross correlator (TOXC), such as e.g. Sequoia (Amplitude Technologies) or Tundra (UltraFast Innovations) [44,45]. Both devices operate on the same principle - mixing of the fundamental and second harmonic frequency to produce third harmonic signal through sum frequency generation. Sequoia uses collimated beam, while the sum frequency generation in Tundra is performed with focused beams. Both the Sequoia and Tundra offer dynamic range $>10^{10}$, and with reduction of noise by optimization of sum frequency generation, the dynamic range can be up to $10^{14}$ [46]. The range of delays depends on the construction of the TOXC, and the commercial solutions offer 500 ps to 4 ns. The main disadvantage of the scanning TOXC is the need to scan the delay to measure a full pre-pulse contrast background. High resolution measurement within the full range may then take tens of minutes to several hours on a laser with $>1$ Hz repetition rate. For single shot systems, the full contrast is typically measured on a front-end, and the final output is measured on the full system only at the identified delays containing pre-pulses. Single shot TOXC was developed and offers promissing results for on-shot characterization of the pre-pulse contrast near the main pulse [47].

### 1.2.2 Methods for improving the pre-pulse contrast

Due to the complexity of the high intensity laser systems, generating high peak power laser pulses with pre-pulse contrast that satisfies the requirements of the laser-matter interaction experiments for clean interaction is challenging. Several techniques for contrast enhancement have been developed and are being employed to meet the experimental requirements.

A typical mode-locked oscillator operates at repetition rate corresponding to the round trip time in the oscillator cavity - typically tens or hundreds of MHz. Pulse picking with Pockel's cell is used to suppress the remaining pulses that are not amplified in the CPA system. The limiting factors for the contrast enhancement with pulse pickers are the extinction ratio of the polarizers, and the switching speed of the Pockel's cell and high voltage driver.

A double CPA configuration is used in combination with nonlinear processes to improve the contrast of the pulses generated by the oscillator and amplified in the first amplification stages [48]. In this method, the pulse is first amplified in a first CPA system. After it is re-compressed, cross-polarized wave generation (XPW) [49–51], saturable absorber [52], or other method are used to enhance the pre-pulse contrast. The pulse is then stretched again and amplified in the second CPA system.

Other systems utilize OPCPA instead of conventional laser amplifiers to mitigate ASE pedestals [53]. In gain media based on stimulated emission, ASE is generated from the moment when population inversion is established for up to the period of the medium fluorescence life time. For the OPCPA process, the gain is present in the nonlinear medium only during the propagation of the pump pulse, and parametric fluorescence is produced within the time window corresponding to the pump pulse duration. The resulting nanosecond pedestals are reduced to approximately 1 ns and below without utilizing a fast pulse picker.

The pre-pulse contrast might be additionally improved after the compression of the pulse by the use of plasma mirrors [54–58]. Plasma mirror uses the increase in reflectivity of a low-reflectivity optical surface by producing a plasma. The plasma is initiated by the increasing intensity in the pre-pulse background, and the operating point can be optimized to limit the reflection of pre-pulses and maximize the reflection of the main pulse. Typically, the improvement of the pre-pulse contrast by a plasma mirror is at the cost of the energy in the main pulse.

## 1.3 Architecture of the L3-HAPLS laser system

The L3-HAPLS laser is a laser system designed to deliver pulses with peak power of 1 PW at a repetition rate of 10 Hz. The system was designed and built in Lawrence Livermore National Laboratory (LLNL) for the ELI Beamlines project in the Czech Republic, where it serves as one of the laser sources for laser-matter interaction experiments. The laser is currently commissioned to operate at 3.3 Hz repetition rate and 0.5 PW peak power. The integration and commissioning of the laser with the experimental setups in the E3 and E4 experimental halls is currently ongoing. The laser was used as the model laser for the work presented in this thesis, however, the results of this work apply to other lasers with similar architecture.

The L3-HAPLS is unique for being the first all diode pumped petawatt-class laser system with focus on applications rather than basic research of laser-matter interactions. The utilization of diode pumping dramatically reduces the amount of heat stored in the amplifier heads of the pump lasers, enabling the operation at 10 Hz with room temperature He gas cooling of the main amplifiers without any thermal issues.

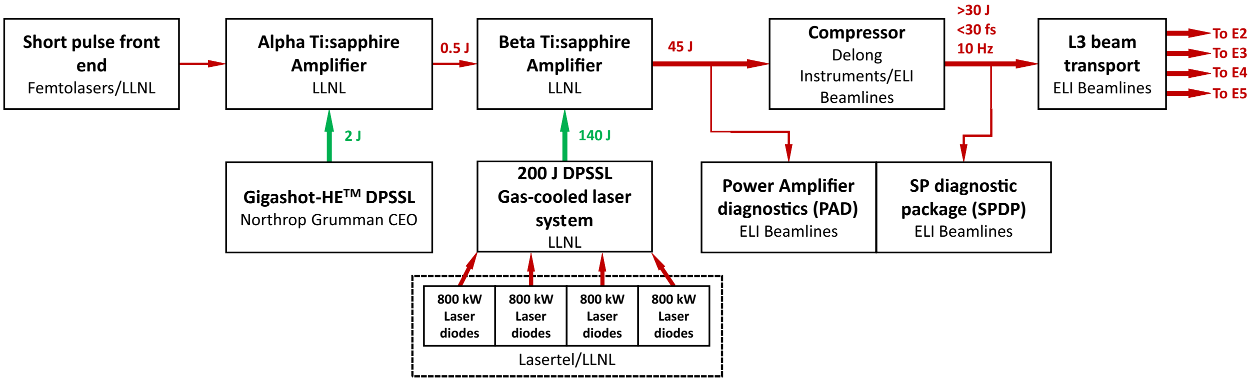

**Figure 1.2:** Block diagram of the L3-HAPLS laser system containing the main optical laser building blocks.

The top level building blocks of the laser amplifier system are shown in figure 1.2. The broadband section of the system utilizes CPA, and Ti:sapphire is used as gain medium in the oscillator and all of the amplifiers. The front end of the system is a commercial double-CPA system delivered by Femtolasers, with an Offner stretcher designed by LLNL. It contains a femtosecond Ti:sapphire oscillator, two multi-pass amplifiers, and an XPW for contrast cleaning. The pulses generated in the front-end are amplified in two multi-pass power amplifiers - Alpha and Beta. After amplification, the pulse is re-compressed in a four-grating compressor and injected into the beam transport to the experimental halls. The two power amplifiers with the optical path in between are fully relay-imaged up to the final grating of the compressor. The two power amplifiers are pumped by two frequency-doubled pump lasers. The pump laser for the Alpha amplifier is a commercial laser system developed by Northrop-Grumman. The pump laser for the Beta amplifier was developed by LLNL. Its front-end contains a fiber system based on the architecture of the front-end of the NIF laser, a regenerative amplifier, and a ring-cavity amplifier. The output of this front-end seeds the main gas cooled, diode pumped amplifier. This amplifier is pumped by diode array modules designed and manufactured specifically for the L3-HAPLS laser by Lasertel. The output pulse from the gas cooled amplifier is frequency doubled and split in two pulses that pump the Beta amplifier head.

An upgrade is planned on the L3-HAPLS laser to increase the peak power and repetition rate from the currently commissioned 0.5 PW at 3.3 Hz to 1 PW at 10 Hz. The commissioning experiments of the experimental setups that will be available to the international user community are currently ongoing and will be continued in parallel with the upgrade.

# Chapter 2

# Properties of the stretched pulse in a CPA amplifier

In a CPA laser amplifier, the pulse is stretched in time prior to amplification to reduce nonlinear optical effects and avoid damage to the optical components. This chapter contains the description of the properties of the stretched pulse that are essential for the theory and numerical calculations presented in the following chapters.

## 2.1 Mathematical description of laser pulses

Laser pulse is an electromagnetic wave of optical frequency, finite in time, emitted by a laser. Lasers emitting laser pulses are called pulsed lasers. The time evolution of the real electric field intensity $\mathcal{E}(t)$ of a general laser pulse in a dielectric medium can be described by its temporal amplitude $A(t)$ and phase $\varphi(t)$ as

$$\mathcal{E}(t) = A(t) \cos\left[\omega_0 t - \varphi(t)\right] \tag{2.1}$$

where $\omega_0$ is the angular frequency of the carrier harmonic electromagnetic wave [59]. The electric and magnetic field of the pulse, propagating in a form of a laser beam, transfers power which can be described by the intensity $I(t)$ related to the amplitude of the electric field intensity as

$$I(t) = \frac{1}{2} c \varepsilon_0 n \left|A(t)\right|^2 \tag{2.2}$$

where $c$ is the speed of light in vacuum, $\varepsilon_0$ is the vacuum permittivity, and $n$ is the refractive index of the medium. In the calculations presented in this thesis, the rapid oscillations of the electric field can be neglected, and the calculations can be simplified by substituting the real electric field intensity $\mathcal{E}(t)$ with the complex electric field intensity $E(t)$ defined as

$$E(t) = A(t) e^{-i\varphi(t)} \tag{2.3}$$

The real electric field intensity can be calculated at any time from the complex equivalent using the formula

$$\mathcal{E}(t) = \frac{1}{2} E(t) e^{i\omega_0 t} + \text{c.c.} \tag{2.4}$$

When the electromagnetic wave passes from a dielectric medium with refractive index $n_1$ to a dielectric medium with refractive index $n_2$, the conservation of energy requires that the integral of the intensity over time and space is preserved. The electric field intensity inside the medium therefore scales with the refractive index as

$$E_2 = \sqrt{\frac{n_1}{n_2}} E_1 \tag{2.5}$$

The dependence of the intensity on the refractive index in equation (2.2) can be omitted when performing calculations for optical systems containing only dielectric materials, vacuum, and air.

The laser pulse can be equivalently described in frequency domain by its spectrum $S(\omega)$ and spectral phase $\phi(\omega)$. Fourier transform $\mathcal{F}$ and inverse Fourier transform $\mathcal{F}^{-1}$ are used to transfer between the time and frequency domain. The definition of the direct and inverse Fourier transform used throughout this thesis is

$$\tilde{f}(\omega) = \mathcal{F}\left[f(t)\right](\omega) = \int_{-\infty}^{\infty} f(t) e^{-i\omega t} dt \tag{2.6a}$$

$$f(t) = \mathcal{F}^{-1}\left[\tilde{f}(\omega)\right](t) = \frac{1}{2\pi}\int_{-\infty}^{\infty} \tilde{f}(\omega) e^{i\omega t} dt \tag{2.6b}$$

Transforming the complex electric field intensity to spectral domain yields

$$\tilde{E}(\Omega) = \tilde{A}(\Omega) e^{-i\phi(\Omega)} \tag{2.7}$$

where the frequency $\Omega$ is the relative frequency with respect to the carrier wave frequency $\omega_0$ of the compressed pulse

$$\Omega = \omega - \omega_0 \tag{2.8}$$

It is important to use the absolute frequency $\omega$ when the considered quantity depends on absolute frequency, such as e.g. wave number and spectral phase modulation corresponding to delay of the pulse in time. This dependence is typically expressed in the equations further in the text explicitly as $\Omega + \omega_0$. The real spectral electric field intensity of the pulse can be written as

$$\tilde{\mathcal{E}}(\omega) = \frac{1}{2}\tilde{E}(\omega - \omega_0) + \frac{1}{2}\tilde{E}^*(-\omega - \omega_0) \tag{2.9}$$

The description of the pulse in time domain is useful for evaluating processes that depend on the evolution of the electromagnetic field in time, such as amplification in gain medium. In spectral domain, it is easier to apply dispersion to the pulse.

## 2.2 Dispersion

Any laser pulse generated in any laser system must at some point propagate through a medium that is different than vacuum - air filling the resonator/amplifier cavity, glass substrate of a mirror or a window, doped crystal forming the gain medium, etc. During the propagation through any transparent medium, the different frequencies within the spectrum of the pulse interact with the medium differently, since the properties of the medium are frequency-dependent. The most common manifestation of the frequency dependence of material properties in optics is material dispersion - the dependence of phase velocity $v_{ph}$ in a medium on frequency $\omega$. The phase velocity can be expressed through a ratio to the vacuum speed of light $c$ as

$$v_{ph}(\omega) = \frac{c}{n(\omega)} \tag{2.10}$$

where $n(\omega)$ is the refractive index of the medium. In this thesis, the term dispersion is also used to denote the phenomenon of different frequencies obtaining different phase from propagating through the pulse stretcher and compressor.

The influence of propagation of a laser pulse through a medium with dispersion is best expressed in frequency domain. The spectral phase $\phi(\Omega, z)$ of the pulse at the relative frequency $\Omega$ and distance $z$ can be written as

$$\phi(\Omega, z) = \phi_0(\Omega) + \delta\phi(\Omega) z \tag{2.11}$$

where $\phi_0(\Omega) = \phi(\Omega, 0)$ is the initial spectral phase of the pulse at the input to the medium. The second term in equation (2.11) contains the contribution of the material dispersion to the spectral phase of the pulse. The spectral electric field intensity $\tilde{E}(\Omega, z)$ of the pulse after propagating through the medium of thickness $z$ with dispersion is then

$$\tilde{E}(\Omega, z) = \tilde{E}_0(\Omega) e^{-i\phi(\Omega, z)} \tag{2.12}$$

with $\tilde{E}_0(\Omega) = \tilde{E}(\Omega, 0)$ being the spectral electric field intensity at the input to the medium. It is important to note that dispersion does not impact the shape of the pulse spectrum and it modifies only the spectral phase.

Since the process of dispersion is linear, it is practical to normalize the contribution of the propagation through each specific material to the unit length. The total dispersion in the path of the pulse through the laser chain is then the sum of the dispersion obtained from the total thickness of each material in the system. The phase $\delta\phi(\omega)$ obtained from the propagation through the unit length of the medium can be expanded into Taylor series, yielding

$$\delta\phi(\Omega) = \sum_{m=0}^{\infty} \frac{1}{m!} D_m(\omega_0) \Omega^m \tag{2.13}$$

where

$$D_m(\omega_0) = \left. \frac{d^m}{d\omega^m} \frac{\omega n(\omega)}{c} \right|_{\omega = \omega_0} \tag{2.14}$$

is the $m$-th dispersion order coefficient at the center frequency of the pulse.

The different dispersion orders impact the pulse in a different way. Assuming the pulse is initially compressed, the spectral phase $\phi_0(\omega) = 0$. This means that all the frequency components of the pulse are in phase at $t = 0$, and the pulse is represented by the transform limited temporal intensity

$$I_0(t) = \left[ \mathcal{F}^{-1}\{\sqrt{\tilde{A}(\Omega)}\}(t) \right]^2 \tag{2.15}$$

The electric field intensity is then

$$E_i(t) = A_i(t) e^{i\omega_0 t} \tag{2.16}$$

The first two dispersion orders do not impact the temporal shape of the pulse. The term $D_0(\omega_0)$ introduces a constant phase offset, and consequently changes the absolute phase of the carrier electromagnetic wave under the pulse envelope in time. The term $D_1(\omega_0)$ introduces linear phase shift over the spectrum, which corresponds to a delay $T$ of the pulse at distance $z$ in the medium. The spectral components are in phase at time $t = T$, and the amplitude can be written as

$$A(t, z) = A_i(t - T) \tag{2.17}$$

The first order dispersion term is therefore inversely proportional to the group velocity $v_g(\omega_0)$ of propagation of the pulse through the medium

$$D_1(\omega_0) = \frac{1}{v_g(\omega_0)} \tag{2.18}$$

Higher order dispersion terms modify the temporal shape of the pulse. The second order term introduces linear chirp, and is discussed in more details in relation to the CPA amplifiers in the following section.

## 2.3 Chirped pulse in a CPA system

In a CPA amplifier system, the pulse is stretched in time prior to the amplification process, and it is re-compressed once the desired pulse energy is obtained. The stretcher and compressor introduce significant dispersion to the pulse in order to achieve the large stretch factors required in petawatt-class lasers. The dispersion management of the CPA system requires matching of the stretcher and material dispersion to the dispersion of the compressor in order to achieve transform limited pulse at the compressor output. Presence of higher order dispersion terms at the output of the CPA laser systems limits the minimum pulse duration achievable after re-compression.

The stretcher and compressor introduce spectral phase $\Phi_s(\omega)$ and $\Phi_c(\omega)$, respectively. The initially compressed pulse entering the stretcher can be represented in spectral domain as

$$\tilde{A}_i(\Omega) = \sqrt{S_0(\Omega)} \tag{2.19}$$

After propagating through the stretcher, the pulse becomes

$$\tilde{E}_s(\Omega) = \tilde{A}_i(\Omega) e^{-i\Phi_s(\Omega)} \tag{2.20}$$

The stretcher (and similarly compressor) phase can be expanded into Taylor series around the carrier frequency $\omega_0$ of the compressed pulse, yielding

$$\Phi_s(\Omega) = \sum_{m=0}^{\infty} \frac{1}{m!} \Phi_{sm}(\omega_0) \Omega^m \tag{2.21}$$

with

$$\Phi_{sm}(\omega_0) = \left. \frac{d^m \Phi_s(\omega)}{d\omega^m} \right|_{\omega_0} \tag{2.22}$$

Analogically to material dispersion, the expansion terms $\Phi_{s0}(\omega_0)$ and $\Phi_{s1}(\omega_0)$ describe the absolute phase and time delay of the pulse at the stretcher output. The second order phase term $\Phi_{s2}(\omega_0)$ of the stretcher describes the group delay dispersion (GDD). From the higher order dispersion terms (the terms that impact pulse shape), the second order dispersion term is typically dominant over the bandwidth of the pulse, and the stretcher phase can be approximated as

$$\Phi_s(\Omega) \approx \frac{1}{2} \Phi_{s2}(\omega_0) \Omega^2 \tag{2.23}$$

Within this approximation, the response of the stretcher to a Dirac delta impulse $\delta(t)$ is a chirped pulse

$$E_\delta(t) = \sqrt{\frac{\beta}{i\pi}} e^{i\left(\omega_0 t + \beta t^2\right)} \tag{2.24}$$

with linear chirp constant $\beta$ given as

$$\beta = \frac{1}{2\Phi_{s2}(\omega_0)} \tag{2.25}$$

The frequency of the oscillations of the electromagnetic field within the chirped pulse can be calculated as a first derivative of the temporal phase, yielding

$$\omega = \frac{d}{dt}\left[\omega_0 t + \beta t^2\right] = \omega_0 + 2\beta t \tag{2.26}$$

For $\beta > 0$, the pulse is positively chirped and the frequency increases linearly in time, while for $\beta < 0$ the pulse has negative chirp and the frequency decreases.

Stretching an arbitrary transform limited pulse given by (2.19) in a stretcher with phase (2.23) produces a stretched pulse with electric field intensity

$$E_s(t) = A_s(t)e^{-i\varphi_s(t)} = \sqrt{\frac{\pi}{i\beta}} e^{-i\beta t^2} \mathcal{F}^{-1}\left\{ A_i\left(-\frac{\Omega}{2\beta}\right) e^{i\frac{\Omega^2}{4\beta}} \right\}(t) \tag{2.27}$$

The temporal shape of the stretched pulse is therefore given by the inverse Fourier transform of the amplitude of the compressed pulse with a quadratic phase term. The amplitude $A_i(t)$ of the compressed pulse is typically zero for $|t| > \Delta t_0$, where $\Delta t_0$ is the FWHM pulse duration of the compressed pulse. The quadratic phase in the inverse Fourier transform in equation (2.27) is then

$$\frac{\Omega^2}{4\beta} < \beta \Delta t_0^2 \tag{2.28}$$

on the interval where the amplitude $A_i(t)$ is non-zero. In the CPA lasers, the stretching factor is typically of the order $10^3$-$10^5$. The duration of the stretched pulse is therefore much longer than the duration of the compressed pulse. Consequently, $\beta\Delta t_0^2 \ll 1$, and the temporal intensity $I_s(t)$ of the stretched pulse can be written as

$$I_s(t) \approx \frac{\pi c \varepsilon_0}{2\beta} \left| \mathcal{F}^{-1}\left\{ A_i\left(-\frac{\Omega}{2\beta}\right)\right\}(t)\right|^2 = \frac{\beta c \varepsilon_0}{2\pi} S_0(2\beta t) \tag{2.29}$$

It is clear from the last equation that for the stretched pulse with linear chirp, the spectrum $S_0(\Omega)$ and intensity $I_s(t)$ of the pulse are equivalent, and one can be calculated from the other using the correspondence between time and frequency given by the equation (2.26), and multiplying by the constant factor $\frac{\beta c \varepsilon_0}{2\pi}$. For an initially transform limited pulse matching the condition $\beta\Delta t_0 \ll 1$, the equation (2.27) simplifies to

$$E_s(t) = \sqrt{\frac{\beta c \varepsilon_0}{2\pi}} \tilde{A}_i(2\beta t) e^{-i\left(\frac{\pi}{4} - \beta t^2\right)} \tag{2.30}$$

The equations (2.26) and (2.29) hold the key assumptions for the simplification of the calculations presented in this thesis. The spectral phase introduced by the stretcher and compressor contains also higher dispersion orders and the chirp is linear only in approximation. As an example, the difference of the actual spectral phase from the quadratic approximation for the L3-HAPLS petawatt laser system can be seen in Figure 2.1. The solid lines are the actual spectral phase introduced by the stretcher and compressor, and the dashed lines represent the quadratic polynomial fits. The L3-HAPLS laser uses an Offner grating stretcher and a four grating compressor configuration, however, similar properties can be expected from other types of stretchers and compressors due to the geometry of the beam paths of individual spectral components.

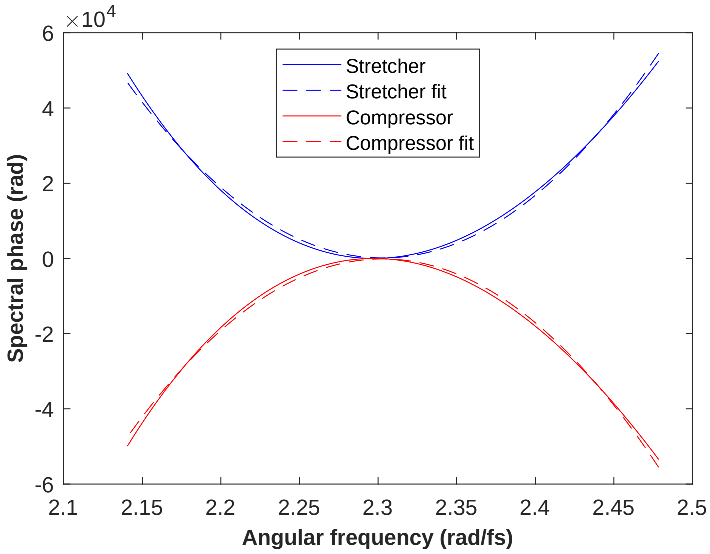

**Figure 2.1:** The higher order spectral phase introduced by the stretcher (blue) and compressor (red) of the L3-HAPLS laser system. The solid lines are the actual phase based on the dispersion management model, the dashed lines represent approximation with a quadratic polynomial.

## 2.4 Polarization of the pulse and Jones calculus in frequency domain

The coupled electric and magnetic field of an electromagnetic wave are in general vector fields. It can be shown that in an isotropic medium, the direction of the electric field intensity vector $\vec{E}(\vec{r}, t)$ and magnetic field intensity vector $\vec{H}(\vec{r}, t)$ are perpendicular to each other and to the direction of propagation given by the wave vector $\vec{k}$ [60]. Further more, the phase of the two vectors $\vec{E}(\vec{r}, t)$ and $\vec{H}(\vec{r}, t)$ is coupled. Polarization of the electromagnetic wave is a statistical property describing the evolution of the field vectors in the plane perpendicular to the propagation direction. In the most general polarization state, the end point of the electric field intensity vector $\vec{E}(t)$ is moving periodically around an elliptical path (see figure 2.2). In special cases, the ellipse reduces to circle (circular polarization, $\chi = \pm\frac{\pi}{4}$) or to a line (linear polarization, $\chi = 0$). Depending on the direction of rotation of the electric field intensity vector, the elliptical and circular polarization can be either right-hand or left-hand oriented, denoted by + and - in the figure 2.2, respectively.
The statistical nature of polarization means that the electromagnetic wave in general constitutes from all possible polarization states. Depending on the properties of the source generating the electromagnetic wave and also on the material in the path of the wave, some polarization states can be preferred, and the wave becomes polarized or partially polarized. The most general description of the polarization of light is with Stokes vector, which contains the information defining the polarization state of the part of the light which is polarized and also about the degree of polarization - the ratio of intensity $I_p$ of light that is polarized to the total intensity $I$.

$$S_0 = I \tag{2.31a}$$
$$S_1 = I_p \cos 2\psi \cos 2\chi \tag{2.31b}$$
$$S_2 = I_p \sin 2\psi \cos 2\chi \tag{2.31c}$$
$$S_3 = I_p \sin 2\chi \tag{2.31d}$$

Due to the polarization selectivity of some of the key components used in majority of the CPA laser systems, the pulses generated by such lasers are typically polarized. It is therefore easier to describe the

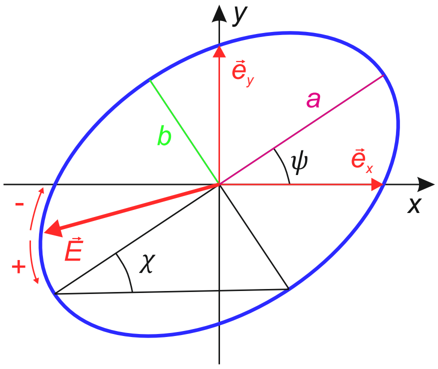

**Figure 2.2:** Illustration of a general elliptical polarization.

polarization state of the pulse in a CPA laser using Jones calculus. The polarization state is expressed as a Jones vector $\vec{e}$ consisting of two mutually perpendicular components $\vec{e}_x$, $\vec{e}_y$ of the electric field intensity vector in the plane perpendicular to the wave vector $\vec{k}$.

$$\vec{e} = \vec{e}_x + \vec{e}_y = \begin{pmatrix} E_{0x} e^{i\varphi_x} \\ E_{0y} e^{i\varphi_y} \end{pmatrix} \tag{2.32}$$

The propagation through a polarization sensitive optical component can be calculated by multiplication of the input Jones vector $\vec{e}_0$ with a Jones matrix $\mathbf{J}$ of the component

$$\vec{e}_1 = \mathbf{J}\vec{e}_0 \tag{2.33}$$

Isotropic media, such as air or glass, allow any polarization state to propagate through. Birefringent media, on the other hand, allow propagation only for specific polarization states. Such polarization states are commonly called eigenwaves of the medium, and they are the ordinary and extraordinary wave. Each eigenwave obtains different phase during the propagation, since the refractive index is different, including the dispersion. In the case of the active medium of the laser amplifier, each eigenwave might be also absorbed or amplified with different rate due to the dependence of the absorption and emission cross section on polarization state. To calculate the Jones matrix of such components, the decomposition of the input Jones vector (expressed in the reference coordinate system $x$,$y$) into the eigenwaves of the medium must be first calculated. In Jones calculus, this can be performed by multiplication of the Jones vector with rotation matrix $\mathbf{R}$ defined as

$$\mathbf{R} \equiv \mathbf{R}(\theta) = \begin{pmatrix} \cos\theta & \sin\theta \\ -\sin\theta & \cos\theta \end{pmatrix} \qquad \mathbf{R}^{-1} \equiv \mathbf{R}^{-1}(\theta) = \begin{pmatrix} \cos\theta & -\sin\theta \\ \sin\theta & \cos\theta \end{pmatrix} \tag{2.34}$$

where $\theta$ is the angle from the reference coordinate system $x$ axis to the coordinate system defining the eigenwaves. Next, the Jones matrix $\mathbf{J}_0$ describing the amplitude and phase propagation of the eigenwaves is used. Finally, the inverse rotation matrix $\mathbf{R}^{-1}$ can be used to transform the output Jones vector back to the reference coordinate system. The resulting Jones vector is then

$$\vec{e}_1 = \mathbf{R}^{-1}\mathbf{J}_0\mathbf{R}\vec{e}_0 \tag{2.35}$$

The time-dependent Jones vector of the pulse with linear polarization in the direction of the $x$ axis is

$$\vec{e}_0(t) = A(t)e^{-i\varphi(t)}\vec{x}_0 \tag{2.36}$$

where $\vec{x}_0$ is the unit vector in $x$ axis direction. Let's assume that the pulse passes through a transparent birefringent medium of thickness $L$ with optical axis at an angle $\theta$ from the $x$ axis in the plane perpendicular to the pulse wave vector. For simplicity, the pulse enters and exits the medium at normal incidence, thus there is no impact of refraction at the faces of the medium. The decomposition of the pulse into the ordinary and extraordinary wave in the medium is then

$$\vec{e}_{0i}(t) = \mathbf{R}(\theta)\vec{e}_0(t) = \sqrt{I(t)}e^{-i\phi(t)}\begin{pmatrix}\cos\theta\\ -\sin\theta\end{pmatrix} = \begin{pmatrix}E_{0e}(t)\\ E_{0o}(t)\end{pmatrix} \tag{2.37}$$

Since the pulse has finite bandwidth, the propagation of the eigenwaves in the medium cannot be easily described by a Jones matrix in time domain. However, matrix formalism can be used in spectral domain if we define frequency domain Jones matrix $\tilde{\mathbf{J}}_0$ as

$$\tilde{\mathbf{J}}_0 = \tau(\Omega+\omega_0)\begin{pmatrix}e^{-i\phi_e(\Omega)} & 0\\ 0 & e^{-i\phi_o(\Omega)}\end{pmatrix} \tag{2.38}$$

where the function $\tau(\Omega+\omega_0)$ represents the frequency-dependent transmission of the medium. The Jones vector $\vec{e}_{0i}(t)$ can be transformed to frequency domain by application of the Fourier transform (2.6a) individually to the vector components, yielding

$$\vec{\tilde{e}}_{0i}(\Omega) = \begin{pmatrix}\tilde{E}_{0e}(\Omega)\\ \tilde{E}_{0o}(\Omega)\end{pmatrix} = \sqrt{S(\Omega)}e^{-i\phi(\Omega)}\begin{pmatrix}\cos\theta\\ -\sin\theta\end{pmatrix} \tag{2.39}$$

At the output of the medium, the frequency domain Jones vector is

$$\vec{\tilde{e}}_{1i} = \tilde{\mathbf{J}}_0\vec{\tilde{e}}_{0i} \tag{2.40}$$

Due to the linearity of the dispersion and the Fourier transform, the Jones calculus can be used for optical pulses in spectral domain with the same computational advantages as in the time domain. The advantage of the application in spectral domain is that at the end of the calculation, impact of both the polarization sensitivity and dispersion of the optical system are obtained.

## 2.5 Nonlinear optical effects

The pulse in a CPA amplifier is stretched in order to minimize the nonlinear optical effects and prevent optical damage during amplification. Efficient extraction of the energy stored in the active medium requires reaching the saturation fluence in the final passes through the amplifier. At the same time, the overall nonlinear phase at the peak intensity of the stretched pulse needs to be kept well bellow 1 rad to minimize the adverse impact of the nonlinear refractive index in transmission optical components on the re-compression of the pulse. Assuming that the maximum fluence of the pulse reaches double the saturation fluence $F_{\mathrm{sat}}$, the duration of the stretched pulse $\tau_s$ shall satisfy the condition

$$\tau_s \gg \frac{4\pi n_2 F_{\mathrm{sat}} L}{\lambda B} \tag{2.41}$$

where $n_2$ and $L$ are the nonlinear refractive index and thickness of the medium, $\lambda$ is the center wavelength of the pulse, and $B$ is the maximum tolerable B-integral.

### 2.5.1 Self phase modulation and cross phase modulation

The general form of the nonlinear wave equation describing propagation of an electromagnetic wave through a dielectric medium is

$$\Delta\vec{E} - \frac{\varepsilon^{(1)}}{c^2}\frac{\partial^2\vec{E}}{\partial t^2} = \frac{1}{\varepsilon_0 c^2}\frac{\partial^2\vec{P}^{(\mathrm{NL})}}{\partial t^2} \tag{2.42}$$

where $c$ is the vacuum speed of light, $\varepsilon_0$ is the vacuum permittivity, $\varepsilon^{(1)}$ is the linear permitivity tensor, and $\vec{P}^{(\mathrm{NL})}$ is the nonlinear polarization vector of the medium [42]. The nonlinear polarization is given as a Taylor expansion in terms of electric field intensity $\vec{E}$

$$\vec{P}^{(\mathrm{NL})} = \varepsilon_0\chi^{(2)}\vec{E}^2 + \varepsilon_0\chi^{(3)}\vec{E}^3 + \varepsilon_0\chi^{(4)}\vec{E}^4 + ... \tag{2.43}$$

with $\chi^{(j)}$ being the $j$-th order susceptibility. The third order term is related to the nonlinearity of the refractive index and its dependence on the electromagnetic wave intensity. The refractive index can be written as

$$n(I) = n_0 + n_2 I \tag{2.44}$$

where $n_0$ and $n_2$ are the linear and nonlinear refractive index, respectively. The linear refractive index and the linear susceptibility are related through the equation

$$n_0 = \sqrt{1+\chi^{(1)}} \tag{2.45}$$

The nonlinear refractive index can be calculated from the third order susceptibility as

$$n_2 = \frac{3}{2n_0^2\varepsilon_0 c}\chi^{(3)} \tag{2.46}$$

Self-phase modulation (SPM) is one of the several manifestations of the nonlinearity of refractive index during propagation of intense optical pulses. Since the intensity of the pulse depends on time, the different parts of the pulse obtain different phase from propagation through the medium of the same thickness - hence the name SPM. When an intense pulse propagates through the medium together with a weak pulse, the intense pulse induces modulation of the refractive index which imprints onto the phase of the weak pulse. This phenomenon is called cross-phase modulation (XPM). In the calculations presented in this thesis, the XPM is not included since the expected impact of XPM on pre-pulse contrast is several orders of magnitude lower than SPM.

The phase obtained by the pulse due to the nonlinearity of refractive index, also called B-integral, is defined as

$$\phi_{\mathrm{NL}}(t) = \frac{\omega}{c}n_2\int_0^L I(z,t)\mathrm{d}z \tag{2.47}$$

Due to the equations (2.26) and (2.29), the phase obtained by a pulse with linear chirp due to the SPM is equivalent to spectral phase.

# Chapter 3

# B-integral post-pulse mirroring

As shown by Didenko [15], the presence of post-pulses during the amplification of a chirped pulse can lead to the generation of pre-pulses upon re-compression. The typical design of a CPA system mitigates introduction of any post-pulses by secondary reflections from optical components. In a CPA amplifier, post-pulses (and consequently pre-pulses) can be also generated due to the birefringence of the amplifier gain medium. This section describes the origin and properties of such contrast defects, utilizing the theoretical background provided in chapter 2.

## 3.1 Anisotropy of optical material properties

A material is called anisotropic, if the properties of the material depend on direction within the material. Anisotropy is typically originating from asymmetry of the internal structure of the material, which can be also induced by subjecting isotropic medium to stress. In optics, anisotropy primarily manifests through the dependence of refractive index on the direction of propagation of light through the material, and leads to a phenomenon called birefringence. A typical example of materials with natural birefringence due to its internal structure are calcite, crystallic quartz, BBO, Ti:sapphire, KTP, KD*P, etc. Induced birefringence is typically present in isotropic materials such as glass subjected to mechanical stress or to uneven thermal stress.

Other properties of the materials used in optics and laser technology may also exhibit anisotropy. For example, in anisotropic laser gain media, the absorption and emission cross section depend on the polarization of the propagating electromagnetic wave. Another examples of properties that exhibit anisotropy are the electro-optic coefficient, piezo- and elasto-optic tensor, second order susceptibility, thermal conductivity, thermal expansion, etc [61]. The most significant properties for the work presented in this thesis are discussed in the following sections.

### 3.1.1 Natural birefringence

In laser technology, the most commonly used materials to construct different laser and optical components are glasses and crystals. Birefringence relates to the properties of the dielectric permittivity tensor $\boldsymbol{\varepsilon}$. The tensor $\boldsymbol{\varepsilon}$ is a symmetric rank 2 tensor which can be written as

$$\boldsymbol{\varepsilon} = \begin{pmatrix} \varepsilon_x & 0 & 0 \\ 0 & \varepsilon_y & 0 \\ 0 & 0 & \varepsilon_z \end{pmatrix} \tag{3.1}$$

with $\varepsilon_x$, $\varepsilon_y$ and $\varepsilon_z$ being the principal values of the tensor $\boldsymbol{\varepsilon}$ along the crystallographic axes [61]. Different crystallic structures exhibit symmetry properties that reduce the number of independent elements of the permittivity tensor. Cubic crystals and isotropic materials can be described with a single principal value $\varepsilon = \varepsilon_x = \varepsilon_y = \varepsilon_z$ and a single refractive index $n = \sqrt{\varepsilon}$ [61]. The propagation of light through such materials is independent of polarization and propagation direction. A typical example of isotropic optical materials are glasses[1] and cubic crystals such as YAG, $BaF_2$, and some semiconductor materials such as GaP and Si.

The dielectric permitivity tensor of hexagonal, trigonal and tetragonal crystals can be described by two independent principal values $\varepsilon_x = \varepsilon_y$ and $\varepsilon_z$. Such crystals are called uniaxial. The unique crystallographic axis is the c-axis, also called the optical axis. An example of uniaxial crystals are BBO, KD*P, Ti:sapphire, calcite, etc.

All three principal values of the permitivity tensor $\boldsymbol{\varepsilon}$ are independent for orthorhombic, monoclinic, and triclinic crystals. Such crystals are called biaxial [61]. KTP, KTA and LBO are examples of biaxial crystals.

The directional dependence of refractive index of a material follows from the dispersion equation [60]. Assuming propagation of a harmonic wave

$$\vec{E}(\vec{r}, t) = \vec{E}_0 e^{i\vec{k}\cdot\vec{r}} e^{-i\omega t} = \vec{E}_0 e^{i\frac{2\pi}{\lambda}\vec{l}\cdot\vec{r}} e^{-i\omega t} \tag{3.2}$$

with amplitude $\vec{E}_0$, angular frequency $\omega$, and wave vector $\vec{k}$ through a material with dielectric permittivity tensor $\boldsymbol{\varepsilon}$, the dispersion equation can be written as

$$\boldsymbol{\varepsilon} \cdot \vec{E}_0 + \vec{l}\left(\vec{l} \cdot \vec{E}_0\right) - \left(\vec{l} \cdot \vec{l}\right)\vec{E}_0 = \vec{0} \tag{3.3}$$

The wavelength $\lambda$ is the vacuum wavelength corresponding to the angular frequency $\omega$. The dispersion equation has nontrivial solutions only if

$$\det\left(\boldsymbol{\varepsilon} + \overleftrightarrow{ll} - \vec{l}^2\mathbf{I}\right) = 0 \tag{3.4}$$

where $\overleftrightarrow{ll}$ is the dyadic of the vector $\vec{l}$ with itself defined as

$$\overleftrightarrow{ll} = \begin{pmatrix} l_x l_x & l_x l_y & l_x l_z \\ l_y l_x & l_y l_y & l_y l_z \\ l_z l_x & l_z l_y & l_z l_z \end{pmatrix} \tag{3.5}$$

$\vec{l}^2$ denotes the scalar product of $\vec{l}$ with itself, and $\mathbf{I}$ is the identity matrix. The points $\vec{l}$ which solve the equation (3.4) form a set called wave-vector surface. Each vector $\vec{l}$ on this surface represents a possible direction in which the harmonic wave (3.2) can propagate through the medium. The length of the vector $\vec{l}$ gives the value of the effective refractive index of the wave during the propagation.

If the medium is isotropic, the dielectric tensor $\boldsymbol{\varepsilon}$ can be written as

$$\boldsymbol{\varepsilon} = \begin{pmatrix} n^2 & 0 & 0 \\ 0 & n^2 & 0 \\ 0 & 0 & n^2 \end{pmatrix} \tag{3.6}$$

and the equation (3.4) simplifies to

$$n^2\left(n^2 - l_x^2 - l_y^2 - l_z^2\right)^2 = 0 \tag{3.7}$$

---

[1] Glass can be anisotropic if it contains residual stress from manufacturing process [61]

The solutions of this equation are all vectors $\vec{l}$ with end point lying on a sphere with radius $n$. The wave (3.2) therefore propagates in each direction with the same refractive index $n$, and the polarization of the wave can be arbitrary. Upon refraction on the boundary between the isotropic medium with other isotropic medium, such as air, the refractive index is the same for all polarization directions and angles of incidence. All rays entering the medium at a given angle of incidence are refracted at the same angle, independent of their polarization.
For birefringent uniaxial crsytals such as sapphire, BBO or KD*P, the dielectric tensor is

$$\boldsymbol{\varepsilon} = \begin{pmatrix} n_x^2 & 0 & 0 \\ 0 & n_x^2 & 0 \\ 0 & 0 & n_z^2 \end{pmatrix} \tag{3.8}$$

The wave-vector surface becomes

$$\left(n_x^2 - l_x^2 - l_y^2 - l_z^2\right)\left[n_x^2 n_z^2 - n_x^2\left(l_x^2 + l_y^2\right) - n_z^2 l_z^2\right] = 0 \tag{3.9}$$

which can be solved separately as the two following equations:

$$n_x^2 - l_{ox}^2 - l_{oy}^2 - l_{oz}^2 = \quad 0 \tag{3.10a}$$

$$n_x^2 n_z^2 - n_x^2\left(l_{ex}^2 + l_{ey}^2\right) - n_z^2 l_{ez}^2 = \quad 0 \tag{3.10b}$$

The first equation, similar to the isotropic case, is solved for any point $\vec{l_o}$ on a sphere with the radius $n_x$. Due to the analogy with the isotropic case, the wave with wave vector $k_0\vec{l_o}$ is called ordinary wave. The solution of the second equation are all points $\vec{l_e}$ on the surface of a spheroid with the two distinct axes having lengths $n_x$ and $n_z$. This second wave is different from the isotropic case, and it is called extraordinary wave. The main difference between the isotropic and the uniaxial birefringent medium is that only waves with ordinary and extraordinary polarization can propagate through the medium. Such waves are also called eigenwaves of the medium. Any other polarization is decomposed into the ordinary and extraordinary polarization components. The ordinary wave propagates with the refractive index

$$n_o(\phi, \theta) = n_x \tag{3.11}$$

and for the extraordinary wave the refractive index is

$$n_e(\phi, \theta) = \frac{n_x n_z}{\sqrt{n_x^2 \sin^2\theta + n_z^2 \cos^2\theta}} \tag{3.12}$$

Here $\phi$ is the angle in the $x$-$y$ plane, measured from the $x$ axis, and $\theta$ is the angle from the $z$ axis. From these two equations it follows that the ordinary and extraordinary waves propagate with the same refractive index $n_x$ along the c-axis ($\theta = 0$). The difference in the refractive index is largest for propagation in the direction perpendicular to the c-axis.

### 3.1.2 Refraction on birefringent crystal surface

Upon refraction at the boundary of the uniaxial birefringent medium with an isotropic medium, the polarization of the input light is decomposed into the ordinary and extraordinary waves propagating through the birefringent medium. Since the two polarizations in general propagate with different refractive indices, their angle of refraction is different. In laser amplifiers with birefringent gain medium, the refraction on the input and output face of the gain medium impacts the performance of the amplifier. The geometry of the gain medium and propagation of the amplified beams has to be optimized to achieve the desired performance.

The direction of the refracted ordinary and extraordinary waves can be calculated from the continuity of the tangential component of the electric field intensity vectors at the boundary, which implies that the tangential component of the wave vectors is equal for each of the waves. The decomposition of the input wave wave vector $\vec{l}_{\mathrm{in}}$ into the normal and tangential components $\vec{l}_n$ and $\vec{l}_t$ with respect to the medium boundary is depicted in Figure 3.1a. The normal vector to the boundary is denoted $\vec{n}$, and the spherical coordinate angles of the input wave vector are $\phi$ and $\theta$.

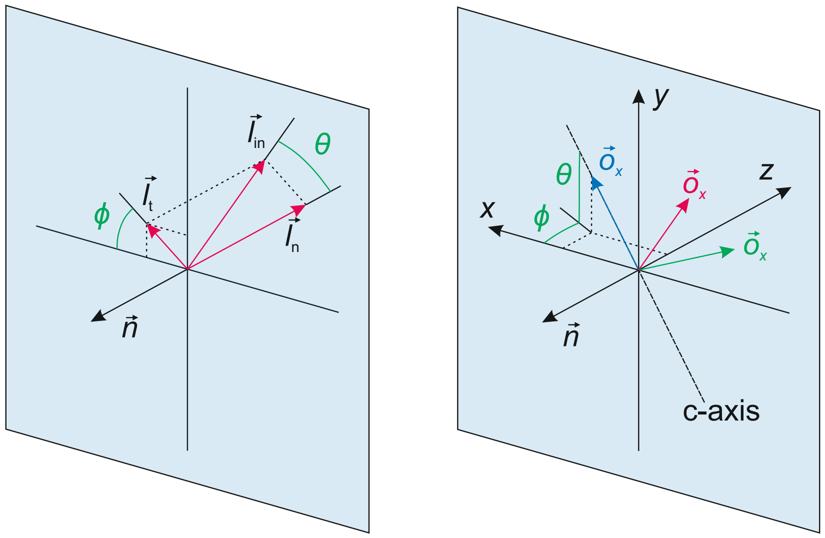

**(a)** **(b)**

**Figure 3.1:** Geometry of incidence of electromagnetic wave (a) and orientation of the c-axis (b) on a boundary between uniaxial crystal and isotropic medium.

The normal and tangential components $\vec{l}_{\mathrm{n}}$ and $\vec{l}_{\mathrm{t}}$ can be calculated using the formulas

$$\vec{l}_{\mathrm{n}} = \left(\vec{n}\cdot\vec{l}_{\mathrm{in}}\right)\vec{n} \tag{3.13a}$$

$$\vec{l}_{\mathrm{t}} = \vec{l}_{in} - \left(\vec{n}\cdot\vec{l}_{\mathrm{in}}\right)\vec{n} \tag{3.13b}$$

The refracted ordinary and extraordinary wave wave vectors $\vec{l}_{\mathrm{o}}$ and $\vec{l}_{\mathrm{e}}$ can be expressed using the normal and tangential component of the input wave vector as

$$\vec{l}_{\mathrm{o}} = \vec{l}_{\mathrm{t}} + s_{\mathrm{o}}\vec{l}_{\mathrm{n}} \tag{3.14a}$$

$$\vec{l}_{\mathrm{e}} = \vec{l}_{\mathrm{t}} + s_{\mathrm{e}}\vec{l}_{\mathrm{n}} \tag{3.14b}$$

The constants $s_{\mathrm{o}}$ and $s_{\mathrm{e}}$ can be found by solving the equation (3.10a) for $s_{\mathrm{o}}$ and the equation (3.10) for $s_{\mathrm{e}}$. The first equation for the ordinary wave can be solved right away independently of the direction of the optical axis within the birefringent medium. The solution is

$$s_{\mathrm{o}} = \frac{\sqrt{n_x^2 - ||\vec{l}_{\mathrm{t}}||^2}}{||\vec{l}_{\mathrm{n}}||} \tag{3.15}$$

The resulting ordinary wave vector can be therefore written as

$$\vec{l}_{\mathrm{o}} = \vec{l}_{\mathrm{t}} - \sqrt{n_x^2 - ||\vec{l}_{\mathrm{t}}||^2}\,\vec{n} \tag{3.16}$$

The solution for the extraordinary wave can be found for an arbitrary orientation of the optical axis in the uniaxial medium. Global reference coordinate system can be introduced, which is connected to the boundary of the two media according to Figure 3.1b. The $x$ and $y$ axes are parallel to the boundary and the $z$ axis is perpendicular to the boundary. The angle of the optical axis from the $x$-$y$ plane is $\phi_{oa}$ and from the $x$-$z$ plane $\theta_{oa}$. For $\phi_{oa} = 0$ and $\theta_{oa} = 0$, the optical axis is in the same direction as the global coordinate system $x$ axis.

To simplify the solution of the wave-vector surface for the extraordinary wave, the equation (3.10) must be solved in the coordinate system of the permittivity tensor $\boldsymbol{\varepsilon}$. First, the wave vectors and their tangential and normal components are transformed into the coordinate system of $\boldsymbol{\varepsilon}$. For this purpose, matrix transforms $\mathbf{R}$ and $\mathbf{R}^{-1}$ are introduced as

$$\vec{k} = \mathbf{R}\vec{k}^{(\varepsilon)} \tag{3.17a}$$

$$\vec{k}^{(\varepsilon)} = \mathbf{R}^{-1}\vec{k} \tag{3.17b}$$

where $\vec{k}$ and $\vec{k}^{(\varepsilon)}$ is the same vector expressed in global coordinate system and in the coordinate system of $\boldsymbol{\varepsilon}$, respectively. The transform $\mathbf{R}$ is defined as

$$\mathbf{R} = \begin{pmatrix} -\cos\phi\sin\theta & -\sin\phi & \cos\phi\cos\theta \\ \cos\theta & 0 & \sin\theta \\ -\sin\phi\sin\theta & \cos\phi & \sin\phi\cos\theta \end{pmatrix} \tag{3.18}$$

and the inverse transform $\mathbf{R}^{-1}$ is

$$\mathbf{R}^{-1} = \mathbf{R}^{T}. \tag{3.19}$$

Since the determinants of the transform matrices are equal to one, the transform preserves the length of vectors. Therefore

$$\vec{l}_{\mathrm{e}}^{(\varepsilon)} = \vec{l}_{\mathrm{t}}^{(\varepsilon)} + s_{\mathrm{e}}\vec{l}_{\mathrm{n}}^{(\varepsilon)}. \tag{3.20}$$

Substituting into (3.10), the following equation for $s_{\mathrm{e}}$ is obtained

$$n_x^2 n_z^2 - n_x^2\left[(l_{\mathrm{tx}}^{(\varepsilon)} + s_{\mathrm{e}} l_{\mathrm{nx}}^{(\varepsilon)})^2 + (l_{\mathrm{ty}}^{(\varepsilon)} + s_{\mathrm{e}} l_{\mathrm{ny}}^{(\varepsilon)})^2\right] - n_z^2(l_{\mathrm{tz}}^{(\varepsilon)} + s_{\mathrm{e}} l_{\mathrm{nz}}^{(\varepsilon)})^2 = 0 \tag{3.21}$$

which can be re-arranged into a quadratic equation for $s_e$

$$(\boldsymbol{\varepsilon}\vec{l}_{\mathrm{n}}^{(\varepsilon)}) \cdot \vec{l}_{\mathrm{n}}^{(\varepsilon)} s_{\mathrm{e}}^2 + 2(\boldsymbol{\varepsilon}\vec{l}_{\mathrm{n}}^{(\varepsilon)}) \cdot \vec{l}_{\mathrm{t}}^{(\varepsilon)} s_{\mathrm{e}} + (\boldsymbol{\varepsilon}\vec{l}_{\mathrm{t}}^{(\varepsilon)}) \cdot \vec{l}_{\mathrm{t}}^{(\varepsilon)} - n_x^2 n_z^2 = 0 \tag{3.22}$$

The solution of this quadratic equation is

$$s_{\mathrm{e}} = \frac{-(\boldsymbol{\varepsilon}\vec{l}_{\mathrm{n}}^{(\varepsilon)}) \cdot \vec{l}_{\mathrm{t}}^{(\varepsilon)} \pm \sqrt{[(\boldsymbol{\varepsilon}\vec{l}_{\mathrm{n}}^{(\varepsilon)}) \cdot \vec{l}_{\mathrm{t}}^{(\varepsilon)}]^2 + [n_x^2 n_z^2 - (\boldsymbol{\varepsilon}\vec{l}_{\mathrm{t}}^{(\varepsilon)}) \cdot \vec{l}_{\mathrm{t}}^{(\varepsilon)}](\boldsymbol{\varepsilon}\vec{l}_{\mathrm{n}}^{(\varepsilon)}) \cdot \vec{l}_{\mathrm{n}}^{(\varepsilon)}}}{(\boldsymbol{\varepsilon}\vec{l}_{\mathrm{n}}^{(\varepsilon)}) \cdot \vec{l}_{\mathrm{n}}^{(\varepsilon)}} \tag{3.23}$$

The ± in the numerator corresponds to the fact that there are two intersections of the line (3.20) with the spheroid (3.10). Here, only the solution with the + sign respects the direction of propagation of the refracted wave in the sense that the normal component of the refracted wave vector has the same direction as the normal component of the incident wave. The refractive index for the extraordinary wave can be calculated from

$$n_{\mathrm{e}} = \sqrt{||\vec{l}_{\mathrm{t}}||^2 + s_{\mathrm{e}}^2||\vec{l}_{\mathrm{n}}||^2} \tag{3.24}$$

The angles $\phi$ and $\theta$ of the refracted extraordinary wave in the coordinate system $o_x$,$o_y$,$o_z$ can be calculated as

$$\phi = \arccos\left(\frac{\vec{l}^{(\varepsilon)}_{\mathrm{e}\perp} \cdot \vec{o}_x}{||\vec{l}^{(\varepsilon)}_{\mathrm{e}\perp}||}\right) \tag{3.25a}$$

$$\theta = \arccos\left(\frac{\vec{l}^{(\varepsilon)}_{\mathrm{e}} \cdot \vec{o}_z}{||\vec{l}^{(\varepsilon)}_{\mathrm{e}}||}\right) \tag{3.25b}$$

where $\vec{o}_x$ and $\vec{o}_z$ are the unit vectors in direction of the axes $o_x$ and $o_z$, respectively, and $\vec{l}^{(\varepsilon)}_{e\perp}$ is the projection of the vector $\vec{l}^{(\varepsilon)}_e$ onto the plane $o_x$,$o_z$.

The energy of the light wave propagates in the direction of the Poynting vector $\vec{S}$

$$\vec{S} = \vec{E} \times \vec{H} \tag{3.26}$$

which is in isotropic media parallel with the wave vector. In birefringent media, the Poynting vector $\vec{P}_e$ of the extraordinary wave and the wave vector $\vec{l}_e$ are not necessarily co-linear. As a consequence, the energy of the extraordinary wave propagates in a different direction than the wave vector. The angle between the Poynting vector and the wave vector is called walk-off angle, and can be calculated using the wave-vector surface. It can be shown that the direction of the Poynting vector is parallel to the direction of the normal vector to the wave-vector surface. For a given direction $\phi$, $\theta$ of the wave vector $\vec{l}_{\mathrm{e}}$ in the coordinate system of the permittivity tensor, the direction of the Poynting vector $\vec{p}_{\mathrm{e0}}$ in the global coordinate system can be calculated using the equation

$$\vec{p}_{\mathrm{e0}} = n_e \mathbf{R} \begin{pmatrix} \frac{1}{n_z} \cos\phi \sin\theta \\ \frac{1}{n_z} \sin\phi \sin\theta \\ \frac{1}{n_x} \cos\theta \end{pmatrix} \tag{3.27}$$

The walk-off angle can be calculated from the dot product of the wave vector $\vec{l}_{\mathrm{e}}$ and the direction of the Poynting vector $\vec{p}_{\mathrm{e0}}$ as

$$\alpha_w = \arccos\left(\frac{\vec{l}_e \cdot \vec{p}_{\mathrm{e0}}}{n_e}\right) \tag{3.28}$$

As an example, the figure 3.2 shows two of the most common incidence geometries used with Ti:sapphire gain medium. The configuration on the left side utilizes incidence at Brewster angle, which improves the degree of polarization of the amplified beam. This configuration is typically used in oscillators and CPA regenerative or multi-pass pre-amplifiers, where the pump and seed beam are focused in the gain medium. To maximize the gain, the crystal is cut to ensure propagation of the seed beam in a direction perpendicular to the c-axis. The configuration shown on the right side of figure 3.2 is most commonly used in CPA power amplifiers. The impact of multiplexing of the seed beam in multi-pass amplifier is minimized when the polarization of the pulse and the c-axis are perpendicular to the plane of multiplexing. In both configurations, the spatial walk-off of the beam due to birefringence is minimal, since the propagation direction is perpendicular to the c-axis. The incidence geometry impacts the generation of post-pulses described in the following sections.

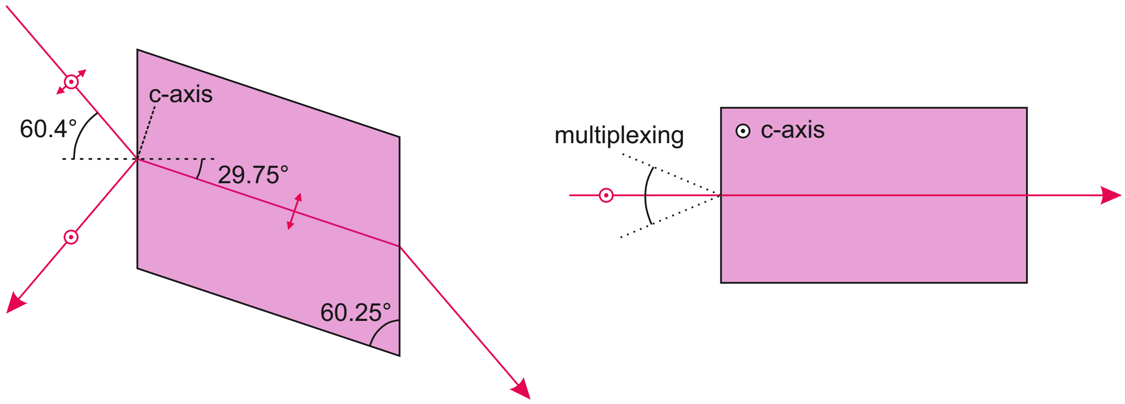

**Figure 3.2:** Example incidence geometries on birefringent laser active media commonly used in CPA laser amplifiers (here shown for Ti:sapphire). Brewster-cut crystal (left) and normal incidence (right).

### 3.1.3 Induced birefringence

Birefringence can be induced in optical materials by stress. This phenomenon is called elasto-optic effect. Mechanical stress can be induced by improper mounting of optical components. Thermal gradients in the optical components cause stress due to uneven thermal expansion [62–64]. Most commonly the thermal gradients are induced in gain media due to asymmetry between the heating and cooling processes. Thermal gradients can be also induced in optical components with low amount of absorption in lasers with high average power.

The most commonly used gain media in PW-class CPA laser amplifiers are Nd:glass, Yb:CaF$_2$, and Ti:sapphire [24]. The first two materials are isotropic, and induced birefringence introduces depolarization loss that can be significant for the performance of the amplifiers [65–67]. Ti:sapphire is naturally birefringent, and the thermally-induced birefringence is much smaller than the natural birefringence [68]. The calculations performed for 2 cm thick Ti:sapphire crystal at 120 J pumping at 1 Hz [69] indicate generation of a post-pulse by depolarization with delay of approximatelly 100 fs and relative intensity $10^{-6}$.

## 3.2 Generation of a post-pulse in birefringent medium

Let's assume propagation of a linearly polarized stretched pulse in a CPA laser system through a birefringent medium, such as e.g. Ti:sapphire. As indicated in Figure 3.3 and described in section 3.1, the main pulse entering the crystal splits into the ordinary and extraordinary polarization components. The two components propagate through the crystal with different group velocities $v_{go}$ and $v_{ge}$. In the case of Ti:sapphire, the main pulse generally has extraordinary polarization since the emission cross section (and consequently the amplifier gain) is higher. The group velocities are related as $v_{go} < v_{ge}$, and the ordinary component becomes a post-pulse with delay $T_1$ and polarization perpendicular to the main pulse. The amplitudes of the ordinary and extraordinary polarization components depend on the angle $\theta_1$ between the polarization axis of the incident pulse and the local c-axis of the crystal, and can be calculated using the rotation matrices defined in (2.34). The delay $T_1$ depends on the difference between the group velocities $v_{go}$, $v_{ge}$, and crystal thickness $L$. Since the polarizations of the two pulses are perpendicular, the post-pulse is not mirrored into a pre-pulse through SPM. However, typical TW and PW laser chains contain several amplifiers with multiple passes through each amplifier, and polarization sensitive components such as polarizers, waveplates and Pockel's cells are typically used. Further more, multiple amplifier crystals can be considered for heat management, and the direction of the c-axis within the crystal can be inhomogeneous. The two mentioned polarization components can therefore project onto the same polarization direction in the following crystal, crystal domain, pass through the amplifier (see Figure 3.3), or in a Pockel's cell, waveplate, or polarizer. Part of the previously generated post-pulse becomes polarized in the same direction as the main amplified pulse, and it can produce pre-pulses due to B-integral post-pulse mirroring as described in [15].

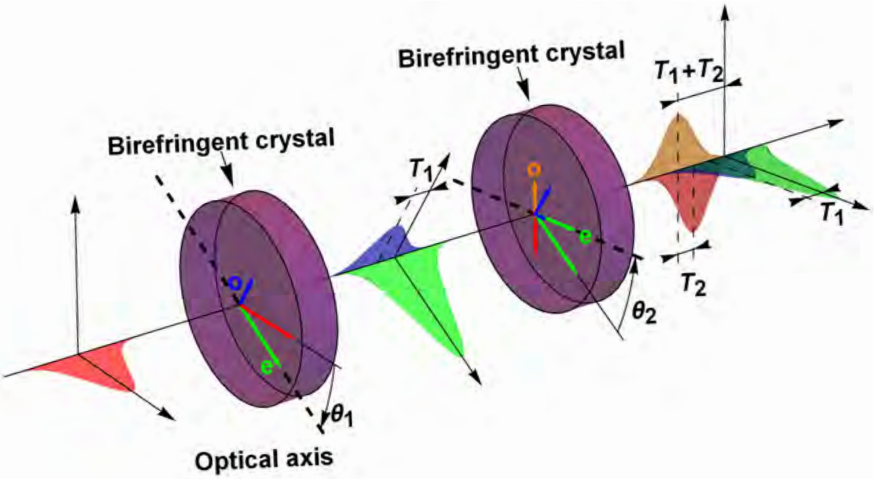

**Figure 3.3:** Generation of a post-pulse in a birefringent crystal with $n_{go} > n_{ge}$ due to imperfect alignment of the crystal to the polarization of the input pulse. The input pulse splits into ordinary and extraordinary components, and the ordinary component is delayed due to lower group velocity. The post-pulse subsequently projects onto the same polarization direction as the main pulse in a second birefringent crystal (drawn here), on a polarizer, Pockel's cell, or waveplate.

The refractive index and dispersion of a birefringent medium are different for the ordinary and extraordinary waves. For the most commonly used materials and components in petawatt-class CPA amplifiers, the first three dispersion orders are dominant within the bandwidth of the pulse, and the impact of higher order dispersion terms can be neglected for the purpose of the calculations presented in this thesis. The spectral phase $\phi_o(\Omega)$ and $\phi_e(\Omega)$ in equation (2.38) can be approximated as

$$\phi_e(\Omega) = \delta\phi_e(\Omega)L \approx D_{e0}L + D_{e1}L\Omega + \frac{1}{2}D_{e2}L\Omega^2 \tag{3.29a}$$

$$\phi_o(\Omega) = \delta\phi_o(\Omega)L \approx D_{o0}L + D_{o1}L\Omega + \frac{1}{2}D_{o2}L\Omega^2 \tag{3.29b}$$

with $D_{o0}$, $D_{o1}$, $D_{o2}$ and $D_{e0}$, $D_{e1}$, $D_{e2}$ being the first three dispersion order coefficients for the ordinary and extraordinary waves at frequency $\omega_0$, respectively. Recalling equations (2.25), (2.26) and (2.30), the two eigenwaves at the output of the birefringent medium in equation (2.39) can be written as

$$E_{1e}(t) = \sqrt{\frac{\beta_e}{\pi}S_0(2\beta_e t)}\cos(\theta)e^{i(\beta_e t^2+\varphi_e)} \tag{3.30a}$$

$$E_{1o}(t) = -\sqrt{\frac{\beta_o}{\pi}S_0\left(2\beta_o(t-T)\right)}\sin(\theta)e^{i\left[\beta_o(t-T)^2+\varphi_o\right]} \tag{3.30b}$$

where the absolute phase $\varphi_e$ and $\varphi_o$, delay $T$, and linear chirp constants $\beta_e$ and $\beta_o$ are given by the following equations

$$\varphi_e = D_{e0}L \tag{3.31a}$$

$$\varphi_o = D_{o0}L \tag{3.31b}$$

$$T_1 = (D_{o1} - D_{e1})L \tag{3.31c}$$

$$\beta_e = \frac{\beta}{1 + 2\beta D_{e2}} \tag{3.31d}$$

$$\beta_o = \frac{\beta}{1 + 2\beta D_{o2}} \tag{3.31e}$$

The pulse propagating as an ordinary wave through the medium becomes delayed by $T_1$ with respect to the extraordinary pulse. Depending on the sign of $T_1$, the ordinary pulse becomes either pre-pulse ($T_1 < 0$) or a post-pulse ($T_1 > 0$). The two pulses obtain additional chirp which is in general different for ordinary and extraordinary polarization. In systems with large stretch factor, the material dispersion and its difference for different polarization components can be neglected, since the relative change in the chirp constant is small. In the case of the L3-HAPLS laser system, the relative change of the pulse chirp due to the overall material dispersion is ≈1.5% of the total chirp from the stretcher, which implies that $\beta$ is approximately constant throughout the amplifier chain.

The first five orders of dispersion parameters for the materials commonly used in the petawatt-class lasers are summarized in appendix A.

## 3.3 Analytic expressions for B-integral post-pulse mirroring

This section contains the derivation of analytic expressions for the spectrum of the satellite pulses resulting from superposition of the stretched main pulse and post-pulses inside a medium with nonzero nonlinear refractive index. The electric field intensity $E_s(t)$ of an arbitrary stretched pulse produced by stretching a compressed pulse in a stretcher can be written as

$$E_s(t) = A_s(t)e^{-i\varphi_s(t)} \tag{3.32}$$

where $A_s(t)$ and $\varphi_s(t)$ are the temporal amplitude and temporal phase of the pulse. The corresponding frequency-domain electric field is then

$$\tilde{E}_s(\Omega) = \tilde{A}_i(\Omega)\tau_{str}(\Omega)e^{-i[\phi_i(\Omega)+\Phi_{str}(\Omega)]} \tag{3.33}$$

Here $\tilde{A}_i(\Omega)$ and $\phi_i(\Omega)$ are the spectral amplitude and spectral phase of the compressed pulse, and $\tau_{str}(\Omega)$ and $\Phi_{str}(\Omega)$ are the frequency-dependent transmittance and spectral phase introduced by the stretcher. The phase $\phi_i(\Omega) \approx 0$ for well compressed pulses.

Post-pulses generated in the amplifier by secondary reflections and due to birefringence of the amplifier gain medium can be considered delayed replicas of the main pulse. The superimposed electric field intensity $E(t)$ of the main pulse and $N$ post-pulses can be written as

$$E(t) = \sum_{n=0}^{N} \sqrt{C_n}\gamma_n E_s(t - T_n) = \sum_{n=0}^{N} \sqrt{C_n}\gamma_n A_s(t - T_n)e^{-i\varphi_s(t-T_n)} \tag{3.34}$$

with $C_n$ and $T_n$ being the relative intensity contrast and delay of the $n$-th pulse with respect to the main pulse. It is assumed that $n = 0$, $C_0 = 1$, and $T_0 = 0$ for the main pulse. The sign $\gamma_n = \pm 1$ determines whether the $n$-th pulse is added or subtracted in the superposition, and is useful for

describing situations when the superposition of pulses results from projection of pulses with mutually perpendicular polarization onto the same polarization axis.
The intensity of the superimposed main pulse and $N$ post pulses is then

$$I(t) = \frac{1}{2}\varepsilon_0 c \left| \sum_{n=0}^{N} \sqrt{C_n}\gamma_n A_s(t-T_n) e^{-i\varphi_s(t-T_n)} \right|^2 \tag{3.35}$$

where $c$ is the vacuum speed of light and $\varepsilon_0$ is the vacuum permittivity. The squared absolute value of the sum in (3.35) can be re-written as a sum of intensities of the individual pulses, and a sum of modulation terms resulting from superposition of the fields of the $k$-th and $l$-th pulses.

$$\begin{aligned} I(t) &= \frac{1}{2}\varepsilon_0 c \sum_{n=0}^{N} C_n A_s^2(t-T_n) + \qquad (3.36)\\ &+ \varepsilon_0 c \sum_{k,l=0,k<l}^{N} \sqrt{C_k C_l}\gamma_k\gamma_l A_s(t-T_k) A_s(t-T_l) \cos\left[\varphi_s(t-T_k) - \varphi_s(t-T_l)\right] \end{aligned}$$

As can be seen from the last equation, the resulting temporal intensity $I(t)$ is modulated. Since the pulse is stretched and most traditional stretchers for CPA systems produce pulses with nearly linear chirp, a coupling between temporal intensity and spectral phase exists when the pulses propagate through a medium with nonlinear refractive index. This coupling leads to the modulation of spectral phase of the pulses. The nonlinearity-induced spectral phase $\phi_{NL}^{(n)}(\omega)$ the $n$-th pulse obtains from propagating through a nonlinear medium with thickness $L$ and nonlinear refractive index $n_2$ is

$$\phi_{NL}^{(n)}(\Omega) = \frac{\Omega + \omega_0}{c} n_2 L I\left[g(\Omega) + T_n\right] = o^{(n)}(\Omega) + \sum_{k,l=0;k<l}^{N} \gamma_k\gamma_l A_{kl}^{(n)}(\Omega) \cos\left[\Delta\varphi_{kl}^{(n)}(\Omega)\right] \tag{3.37}$$

where

$$\Delta\varphi_{kl}^{(n)}(\Omega) = \varphi_s\left(g(\Omega) + T_n - T_k\right) - \varphi_s\left(g(\Omega) + T_n - T_l\right) \tag{3.38}$$

The function $g(\Omega)$ is the inverse function to the time-dependent instantaneous frequency, and gives the time within the stretched pulse at which the electric field oscillates at frequency $\Omega + \omega_0$. $g(\Omega)$ exists if the instantaneous frequency is a monotonic function of time (e.g. for pulses with nearly linear chirp, as produced in most traditional stretchers for CPA systems). For pulses with linear chirp, correspondence $t = g(\Omega)$ has the form

$$g(\Omega) = \frac{\Omega}{2\beta} \tag{3.39}$$

With this approximation and assuming that the pulse is initially perfectly compressed, the phase difference $\Delta\varphi_{kl}^{(n)}(\Omega)$ becomes

$$\Delta\varphi_{kl}^{(n)}(\Omega) = \eta_{kl}^{(n)} - (\Omega + \omega_0)T_{kl} \tag{3.40a}$$

$$\eta_{kl}^{(n)} = \beta(T_l^2 - T_k^2) - 2\beta T_n T_{kl} \tag{3.40b}$$

$$T_{kl} = T_l - T_k \tag{3.40c}$$

The term $o^{(n)}(\Omega)$ of the spectral phase is the contribution from the pulse shape given as

$$o^{(n)}(\Omega) = \frac{1}{2}(\Omega + \omega_0)\varepsilon_0 n_2 L \sum_{k=0}^{N} C_k A_s^2\left(\frac{\Omega}{2\beta} + T_n - T_k\right) \tag{3.41}$$

and $A_{kl}^{(n)}(\Omega)$ is the amplitude of spectral phase modulation from the superposition of pulses with indices $k$ and $l$

$$A_{kl}^{(n)}(\Omega) = (\Omega + \omega_0)\varepsilon_0 n_2 L\sqrt{C_k C_l} A_s\left(\frac{\Omega}{2\beta} + T_n - T_k\right) A_s\left(\frac{\Omega}{2\beta} + T_n - T_l\right) \tag{3.42}$$

Using expansion to Taylor series, binomial expansion, and Euler's formula, the nonlinearity-induced spectral phase can be expressed in the form

$$e^{-i\phi_{\mathrm{NL}}^{(n)}(\Omega)} = e^{-io^{(n)}(\Omega)} \prod_{k,l=0;k<l}^{N} \sum_{q=-\infty}^{\infty} Q_{kl,q}^{(n)}(\Omega) e^{-iq(\Omega+\omega_0)T_{kl}} e^{iq\eta_{kl}^{(n)}} \tag{3.43}$$

where

$$Q_{kl,q}^{(n)}(\Omega) = \sum_{m=|q|}^{\infty} \binom{m}{\frac{m+q}{2}} \frac{(-i\gamma_k\gamma_l)^m}{(2m)!!} \left[A_{kl}^{(n)}(\Omega)\right]^m \approx \binom{|q|}{\frac{|q|+q}{2}} \frac{(-i\gamma_k\gamma_l)^{|q|}}{(2|q|)!!} \left[A_{kl}^{(n)}(\Omega)\right]^{|q|} \tag{3.44}$$

The approximation in the last equation is valid in typical CPA systems, since the B-integral from SPM in optical components is $B < 1$ and $\sqrt{C_k} \ll 1$. Under this approximation, the most significan terms are

$$Q_{kl,0}^{(n)}(\Omega) \approx 1 \tag{3.45a}$$

$$Q_{kl,-1}^{(n)}(\Omega) \approx -i\frac{1}{2}\gamma_k\gamma_l A_{kl}^{(n)}(\Omega) \tag{3.45b}$$

$$Q_{kl,-2}^{(n)}(\Omega) \approx -\frac{1}{4}\left[A_{kl}^{(n)}(\Omega)\right]^2 \tag{3.45c}$$

After application to the superposition of pulses and compression of the pulses in a compressor, the resulting frequency-domain electric field $S(\omega)$ is

$$\begin{aligned} \tilde{E}(\Omega) &= \tilde{A}_i(\Omega)\tau_{\mathrm{tot}}(\Omega) e^{i[\phi_i(\Omega)+\Delta\Phi(\Omega)]} \sum_{n=0}^{N} \sqrt{C_n}\gamma_n e^{-i(\Omega+\omega_0)T_n} \\ &\times \; e^{-io^{(n)}(\Omega)} \prod_{k,l=0;k<l}^{N} \sum_{q=-\infty}^{\infty} Q_{kl,q}^{(n)}(\Omega) e^{-iq(\Omega+\omega_0)T_{kl}} e^{iq\eta_{kl}^{(n)}} \end{aligned} \tag{3.46}$$

where $\tau_{tot}(\Omega)$ and $\Delta\Phi(\Omega)$ are the total frequency-dependent transmittance and residual spectral phase from intensity-independent dispersion introduced by passing through the system (stretcher, compressor, transmissive and reflective optical components). As an example, figure 3.4 shows the satellite pulses calculated using the expression (3.46) for propagation of main pulse with a post pulse through a fused silica window. The relative intensity of the post-pulse was assumed $C_1$=$1{\cdot}10^{-4}$, and the delay $T_1$=1 ps. The calculation was performed for three different values of peak B-integral.

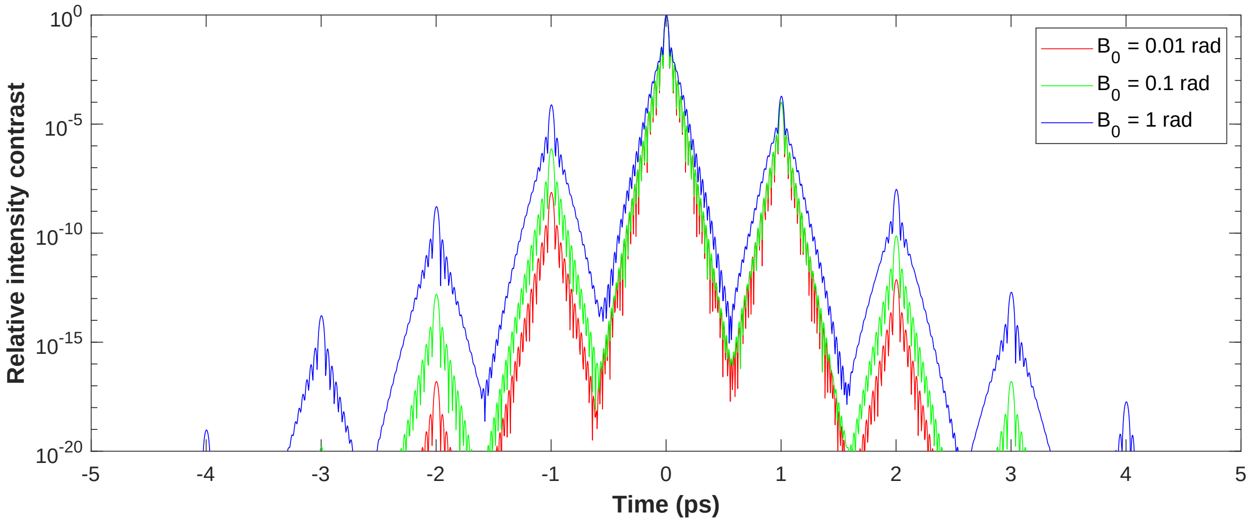

**Figure 3.4:** Satellite pulses from transparent fused silica window, calculated using the derived analytic expression (3.46).

## 3.4 Pre-pulse contrast in collimated and focused beams

In practice, the pre-pulse contrast is typically expressed as the ratio of the peak intensity of the pre-pulse to the peak intensity of the main pulse after compression. The pulses generated by CPA, especially from the petawatt-class lasers, are typically used for laser-matter interaction experiments with the beam focused to a small spot on the target. It is therefore most relevant to express the intensity contrast in the focal spot. The stretched pulse in the nonlinear medium has intensity distribution proportional to $|A_s(\bar{x}, \bar{y}, t)|^2$, where $\bar{x}$, $\bar{y}$ are spatial coordinates across the beam profile, and $t$ is time. In reality, the space and time coordinates can be dependent due to spatio-temporal effects, which brings an extra complexity to the calculations. However, on a well-behaved system, care is taken to ensure that the spatio-temporal couplings are minimal, since their presence leads to degradation of the laser-matter interaction. Under this condition, the pulse can be integrated separately over time and across the beam profile, which also ensures that the spatial and temporal Fourier transforms are independent. The equation (3.32) including the spatial dependence of the field can be re-written as

$$E_s(\bar{x}, \bar{y}, t) = \kappa S(\bar{x}, \bar{y}) A_s(t) e^{-i\varphi_s(t)} \tag{3.47}$$

with $S(\bar{x}, \bar{y})$ being the function describing the electric field amplitude across the spatial beam profile and $\kappa$ a constant scaling the pulse energy.

Let's assume for simplicity propagation of the main pulse and one post-pulse through passive nonlinear medium, such as e.g. glass, followed by an ideal pulse compression. The situation is shown in figure 3.5. The main pulse has index $n = 0$ in the above equations, and the post-pulse has $n = 1$. The delay of the pulses is $T_0 = 0$ and $T_1$, and the relative intensity of the post-pulse is $C_1$. Since the post-pulse assumed here is generated by double reflection from AR coated surfaces or due to birefringence of the gain medium, the factor $C_1$ is a constant. The intensity contrast of the post-pulse after compression is $C_1^{\mathrm{NF}}(x, y) = C_1$, and after focusing on target $C_1^{\mathrm{FF}} = C_1$. The intensity of the first-order pre-pulse generated by SPM depends on the intensity in the nonlinear medium. After compressing the pulse, the intensity contrast ratio $C_{-1}^{\mathrm{NF}}(x, y)$ is

$$C_{-1}^{\mathrm{NF}}(x, y) = \frac{I_{-1}(x, y, -T_1)}{I_0(x, y, 0)} = \left[ \frac{|\int_{-\infty}^{\infty} \tilde{E}_{-1}(x, y, \Omega) e^{-i(\Omega+\omega_0)T_1} d\Omega|}{|\int_{-\infty}^{\infty} \tilde{E}_0(x, y, \Omega) d\Omega|} \right]^2 \tag{3.48}$$

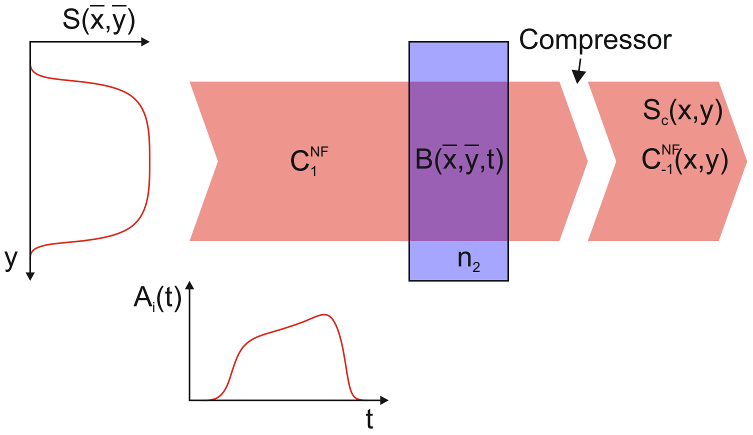

**Figure 3.5:** Impact of temporal and spatial distribution of the pulse intensity on the mirroring of post-pulses to pre-pulses.

where the coordinates $x$ and $y$ are the coordinates in the output beam of the compressor. Using the equations (3.44) and (3.46) for the case of two pulses under the assumption of low B-integral and weak post pulse, the spectral electric field intensities $\tilde{E}_0(x,y,\Omega)$ and $\tilde{E}_{-1}(x,y,\Omega)$ become

$$\tilde{E}_0(x,y,\Omega) \approx \gamma_0 \tilde{A}_i(\Omega) S_c(x,y) \tag{3.49a}$$

$$\tilde{E}_{-1}(x,y,\Omega) \approx -i\frac{\gamma_1}{2}\tilde{A}_i(\Omega) S_c(x,y) A_{01}^{(0)}(\bar{x},\bar{y},\Omega) e^{i(\Omega+\omega_0)T_1} e^{-i\eta_{01}^{(0)}} \tag{3.49b}$$

In a system with low aberrations, the coordinates $\bar{x}$, $\bar{y}$ relate to the coordinates $x$, $y$ through the beam magnification $M$ as

$$\bar{x} = \frac{x}{M} \tag{3.50a}$$

$$\bar{y} = \frac{y}{M} \tag{3.50b}$$

Another simplification can be done if the delay $T_1$ is considered much shorter than the duration of the stretched pulse, which is typically the case of post-pulses from birefringence. Inserting the complex electric field intensities into the equation (3.48) and using equation (2.29) yields the peak pre-pulse contrast in the compressed beam

$$C_{-1}^{NF}(x,y) = \frac{1}{4}\kappa^4 \varepsilon_0^2 n_2^2 L^2 C_1 S^4\left(\frac{x}{M},\frac{y}{M}\right)\left[\frac{\int_{-\infty}^{\infty}(\Omega+\omega_0)\tilde{A}_i^3(\Omega)d\Omega}{\int_{-\infty}^{\infty}\tilde{A}_i(\Omega)d\Omega}\right]^2 \tag{3.51}$$

The contrast depends on the beam intensity profile as well as on the shape of the stretched pulse (equivalent to the spectrum shape). Assuming the spectrum of the pulse is supergaussian of order $o_t$, the integrals in the last equation can be calculated to obtain

$$C_{-1}^{NF}(x,y) = \left[3^{\frac{2}{o_t}}\right]^{-1} C_1 B_0^2 S^4\left(\frac{x}{M},\frac{y}{M}\right) \tag{3.52}$$

where $B_0$ is the peak B-integral from propagation through the nonlinear medium defined as

$$B_0 = \frac{1}{2}\omega_0 \varepsilon_0 n_2 L \kappa^2 \tag{3.53}$$

The constant factor in equation (3.52) is equal to $1/3$ for $o_t = 2$, and it tends to 1 as the supergaussian order increases to infinity. The resulting first-order pre-pulse contrast is therefore three times lower

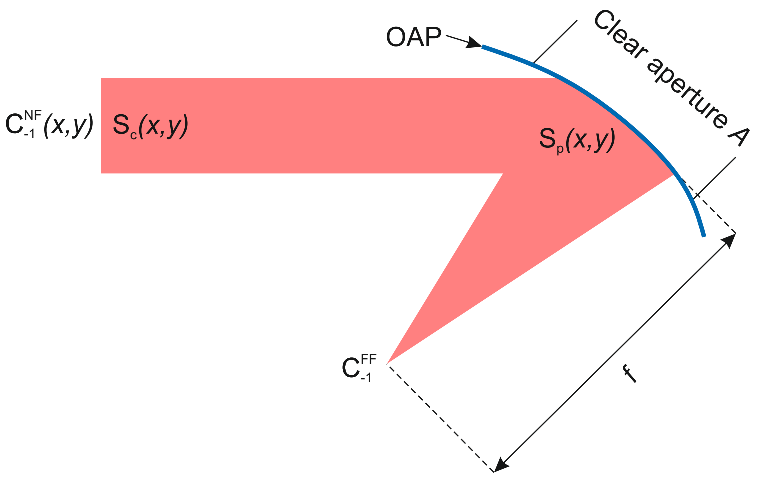

**Figure 3.6:** Illustration of beam focusing on target by an off-axis parabola, and the near field and far field pre-pulse contrast.

for a gaussian pulse spectrum compared to a pulse with rectangular spectrum. It is important to note that this mutual relationship is valid for pulses with the same peak B-integral.

The compressed pulse is typically focused onto a target by an off-axis parabola (OAP) - see figure 3.6. The focused beam intensity $I^{(f)}(t)$ at the center of the focal spot can be calculated from the electric field intensity incident on the OAP as

$$I^{(f)}(t) = \frac{1}{2}\varepsilon_0 c \left| \frac{i}{\lambda f} \iint_A E(x,y,t) dx dy \right|^2 \tag{3.54}$$

where $f$ is the focal length of the OAP and the integration is over the clear aperture $A$ of the parabola. The peak intensity contrast of the focused pulse is then

$$C^{FF}_{-1} = \frac{I^{(f)}_{-1}(-T_1)}{I^{(f)}_0(0)} = \left[ \frac{|\int_{-\infty}^{\infty} \iint_A \tilde{E}_{-1}(x,y,\Omega) e^{-i(\Omega+\omega_0)T_1} dx dy d\Omega|}{|\int_{-\infty}^{\infty} \iint_A \tilde{E}_0(x,y,\Omega) dx dy d\Omega|} \right]^2 \tag{3.55}$$

Similarly to the case of the pre-pulse intensity contrast of the unfocused beam, this equation can be simplified to

$$C^{FF}_{-1} = \frac{1}{4}\kappa^4 \varepsilon_0^2 n_2^2 L^2 C_1 \left[ \frac{\iint_A S_p(x,y) S^2\left(\frac{x}{M}, \frac{y}{M}\right) dx dy \int_{-\infty}^{\infty} (\Omega+\omega_0) \tilde{A}_i^3(\Omega) d\Omega}{\iint_A S_p(x,y) dx dy \int_{-\infty}^{\infty} \tilde{A}_i(\Omega) d\Omega} \right]^2 \tag{3.56}$$

where $S_p(x,y)$ is the beam distribution on the OAP. The calculation can be performed assuming supergaussian spectrum of order $o_t$ and supergaussian beam of order $o_s$. An additional assumption is that the entire beam fits within the clear aperture of the OAP. The resulting focused pulse intensity contrast is

$$C^{FF}_{-1} = \left[ 3^{\frac{4o_t+2o_s}{o_t o_s}} \right]^{-1} C_1 B_0^2 \tag{3.57}$$

with $B_0$ being the peak B-integral (3.53). For the same spectrum shape and peak B-integral, the focused pre-pulse contrast of gaussian beam is 1/9 of the focused contrast for flat-top beam. This is in good agreement with [15].

The nonlinear phase from propagation of a pulse and a post-pulse through $N$ independent optical components can be derived from the equation (3.43). The phase obtained from the individual components add together, and the corresponding field of the first order pre-pulse can be written as

$$e^{-i\phi^{(0)}_{\mathrm{NL}}(\Omega)} = \prod_{m=1}^{N} e^{-i\phi^{(0)}_{\mathrm{NL},m}(\Omega)} \approx -i\frac{1}{2}\gamma_0\gamma_1 e^{i(\Omega+\omega_0)T_1} e^{-i\beta T_1^2} e^{-i\sum_{m=1}^{N} o^{(0)}_m(\Omega)} \sum_{m=1}^{N} A^{(0)}_{01,m}(\bar{x},\bar{y},\Omega) \tag{3.58}$$

where only the terms with the most significant contributions and the approximations (3.45) have been assumed. The modulation amplitude term $A^{(0)}_{01,m}(\bar{x},\bar{y},\Omega)$ can be simplified to

$$A^{(0)}_{01,m}(x,y,\Omega) \approx (\Omega+\omega_0)\varepsilon_0\kappa_m^2 n_{2,m} L_m \sqrt{C_1} A_s^2\left(\frac{\Omega}{2\beta}\right) S_m^2\left(\frac{x}{M_m},\frac{y}{M_m}\right) \tag{3.59}$$

under the assumption of small delay $T_1$ compared to the stretched pulse duration, low peak B-integral, and low spatial beam aberrations. In the last equation, $n_{2,m}$ and $L_m$ are the nonlinear refractive index and the propagation length in the $m$-th medium. $M_m$ is the beam magnification between the location of the $m$-th component and the OAP. The electric field intensity of the main pulse and the first order pre-pulse can be written as

$$\tilde{E}_0(x,y,\Omega) \approx \gamma_0 \tilde{A}_i(\Omega) S_p(x,y) \tag{3.60a}$$

$$\tilde{E}_{-1}(x,y,\Omega) \approx -i\frac{\gamma_1}{2}\tilde{A}_i^3(\Omega) S_p(x,y) e^{i(\Omega+\omega_0)T_1} e^{-i\beta T_1^2}(\Omega+\omega_0)\varepsilon_0\sqrt{C_1}\sum_{m=1}^{N}\kappa_m^2 n_{2,m} L_m S_m^2\left(\frac{x}{M_m},\frac{y}{M_m}\right) \tag{3.60b}$$

The focused beam pre-pulse contrast $C_{-1}^{FF}$ can be then written as

$$C_{-1}^{\mathrm{FF}} = \frac{1}{4}\varepsilon_0^2 C_1 \left[\frac{\sum_{m=1}^{N}\kappa_m^2 n_{2,m} L_m \iint_A S_m^2\left(\frac{x}{M_m},\frac{y}{M_m}\right) S_p(x,y)\,dxdy \int_{-\infty}^{\infty}(\Omega+\omega_0)\tilde{A}_i^3(\Omega)\,d\Omega}{\iint_A S_p(x,y)\,dxdy \int_{-\infty}^{\infty}\tilde{A}_i(\Omega)\,d\Omega}\right]^2 \tag{3.61}$$

The last equation is used in the section 3.4 for evaluation of the impact of neglecting diffraction during beam propagation on the numerical calculation of the pre-pulse contrast.

### 3.4.1 Impact of beam propagation on the B-integral mirroring

The pulse propagates through the CPA amplifiers in the form of a laser beam. The beam has a spatial intensity distribution in the plane perpendicular to the beam propagation direction. This intensity distribution evolves as the beam propagates due to diffraction and phase changes induced by optical components, such as e.g. curved mirrors and lenses. An important parameter for beam propagation is the Fresnel number $F_N$ defined for rotationaly symmetric beams as

$$F_N \approx \frac{a^2}{\lambda\Delta z},\ \text{for}\ \Delta z > a \tag{3.62}$$

with $a$ being the radial size of the beam, $\lambda$ the beam wavelength, and $\Delta z$ the propagation distance [70, 71]. The beam propagation is said to be in near field when $F_N > 1$ and in far field when $F_N < 1$. In the near field, the intensity profile of the beam changes significantly with the propagation distance. In the far field, the intensity profile remains approximately constant and the beam expands due to its divergence. For large Fresnel numbers, the angular frequency approach to the calculation of beam propagation and the transfer function of the free space can be used [70, 71].

The impact of the beam propagation on the beam intensity distribution depends on the location in the laser chain. The oscillator and the first amplifiers of the CPA system typically operate with Gaussian beams focused in the gain medium. At the pulse energies of nJ to mJ typical for such amplifiers, the beam must be focused for efficient extraction of the stored energy. The beam diameter is on the order of 1 mm in such amplifiers. Due to the small size, the beam changes size significantly during propagation over distances of 1 m and longer, however, the intensity distribution is preserved for Gaussian beams. The beam propagation therefore impacts the beam intensity and B-integral in transmissive optical components mostly through the change of the beam size. On the contrary, the power amplifiers typically operate with collimated beam passing through the gain medium, since the energy of the input pulse is already sufficient for reaching the saturation fluence in the final amplification passes without focusing the beam. A flat-top beam profile allows for maximizing the energy in a beam with given beam size and with intensity/fluence limited by the nonlinear optical effects and damage threshold of the optical components.

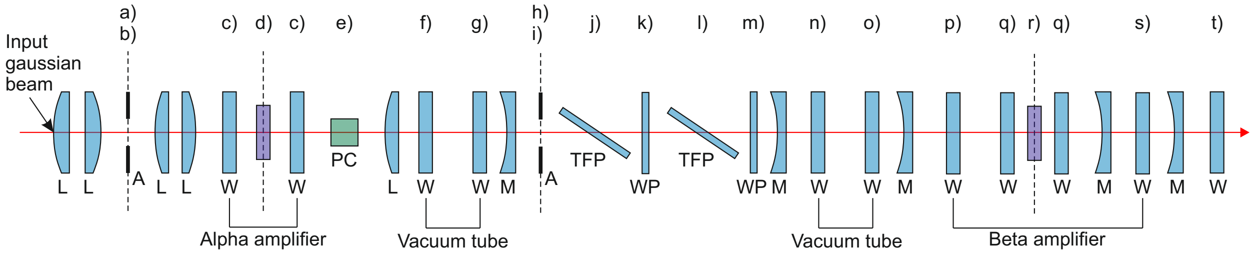

**Figure 3.7:** Schematic of the components in the beam path of the power amplifiers in the L3-HAPLS laser system: L - lens, A - aperture (round or square), W - fused silica window, PC - DKDP Pockel's cell, M - spherical mirror, TFP - thin film polarizer, WP - $\lambda/2$ waveplate.

Figure 3.8 shows the calculated beam intensity distribution on the transmissive optical components and in the gain media for the two power amplifiers and the respective beam paths of the L3-HAPLS laser system. The schematic setup of the components is shown in figure 3.7. The relay-imaging planes are marked with the letter R in the description of the beam profile plots and with dashed lines in the schematic. The descriptions of the beam profile plots also contain the Fresnel numbers $F_N$ for the propagation of the beam. A single Fresnel number is given in the plots calculated from beam propagation over a distance. Two Fresnel numbers are given when the beam passes through a lens/spherical mirror. The first number is for propagation from the input plane to the lens, and the second number is for propagation from the lens to the output plane. Similarly, three Fresnel numbers are given for propagation from the input plane to first lens of a telescope, between the telescope lenses, and from the second lens to the output plane.

The input gaussian beam from the front-end is expanded to overfill a round serrated aperture and to change the intensity distribution of the beam to flat-top profile - see plots a) and b). The first Fresnel number is infinite since the input plane is at the first lens of the telescope. The round flat-top beam is imaged onto the crystal of the Alpha amplifier - see plot d). The beam enters the vacuum chamber of the Alpha amplifier through a window - plot c). The 8 passes inside the Alpha amplifier are all relay imaged by spherical mirrors without any transmissive optic in between. The beam then exits the amplifier chamber through the same window and passes through a DKDP Pockel's cell - plot e). The beam at the Alpha amplifier crystal is imaged to a square aperture by a combination of a lens and a concave mirror. The imaged beam is reduced from circular to a square flat-top beam - plots h) and i). To prevent air break-down in the focus of the imaging telescope, the beam focus is inside a vacuum

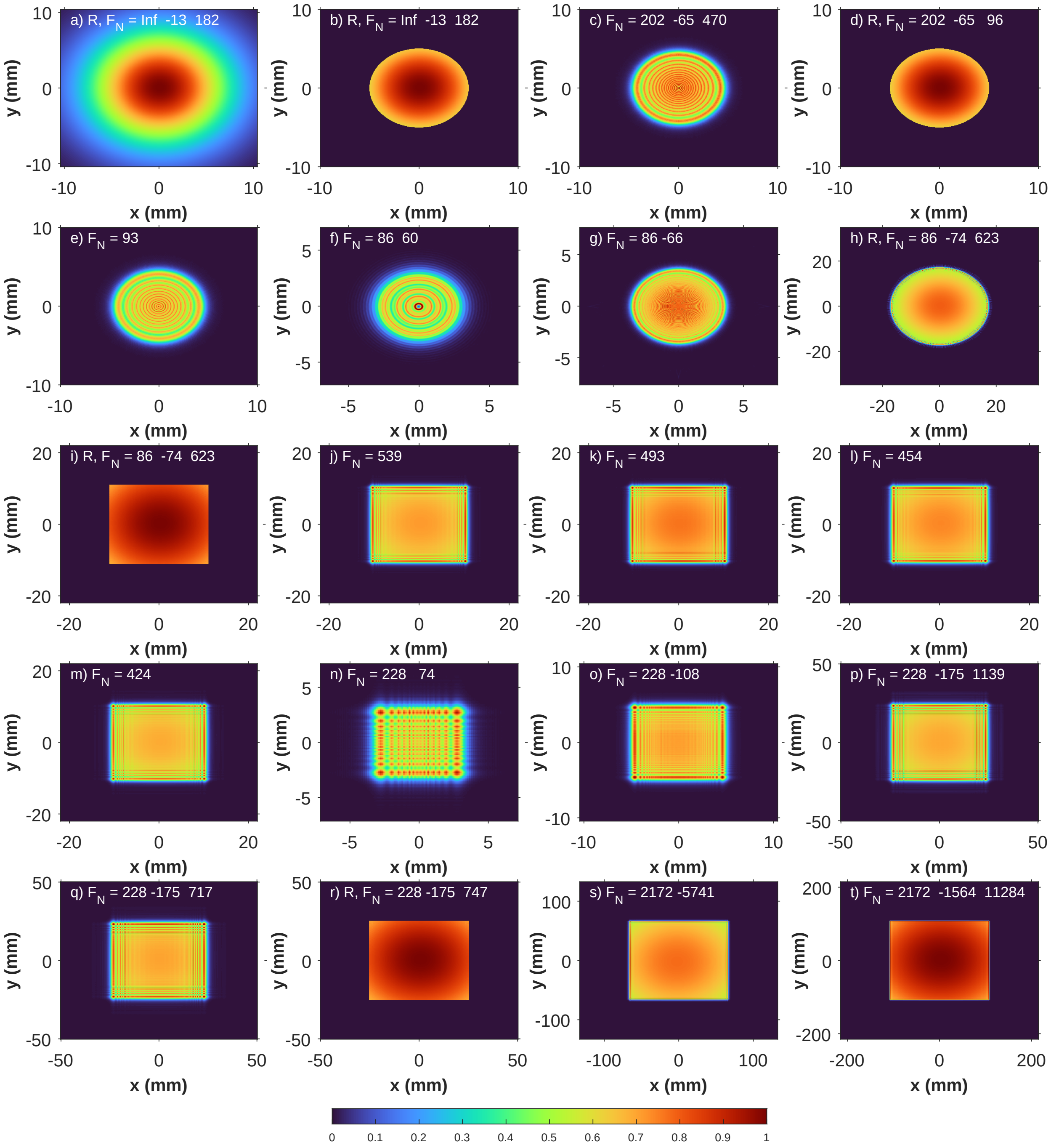

**Figure 3.8:** Numerically calculated intensity beam profiles on the transmissive optical components and at image relay planes in the power amplifier section of the L3-HAPLS laser system.

tube with input and output windows - plots f) and g). The square beam passes through a set of thin film polarizers and $\lambda/2$ waveplates - plots j)-m). The first polarizer serves as the output polarizer of a pulse picker formed by this polarizer together with the DKDP Pockel's cell. The first waveplate and the second polarizer allow for variable attenuation of the beam, and the second waveplate allows the polarization to be set for the Beta amplifier. From the square aperture, the beam is imaged by a telescope to the Beta amplifier head - plot r), passing through an input window of the Beta amplifier vacuum chamber - plot p), and a window on the Beta amplifier head - plot q). The focused beam of the imaging telescope is again passing through a vacuum tube with two windows - plots n) abd o). The Beta amplifier contains 4 passes which are relay imaged to the amplifier head. On each pass of the Beta amplifier, the beam passes through input and output window of the amplifier head. After the fourth pass, the beam is imaged to the compressor by a telescope with two concave mirrors. The beam exits the Beta amplifier diverging through the output window of the vacuum chamber - plot s). After collimation by the second mirror of the telescope, the beam enters the compressor vacuum chamber through the input window - plot t).

In order to evaluate the impact of the beam intensity modulation due to diffraction during propagation, the equation (3.56) was used to calculate the contrast of the first order pre-pulse with flat-top beam distribution and with diffraction. The cases that were compared correspond to assuming intensity distribution d) in the locations e), f) and g), scaled by the magnification introduced by the lens between the two locations. Similar comparison was performed for the case of intensity distribution i) in the locations m), n), o) and p). The ratio of the pre-pulse contrast calculated through equation (3.56) using the real diffracted beam and the flat-top distribution is 98.2% ± 5.3%. The equation (3.61) was used to calculate the overall impact of all the components, including the difference in the component thickness, nonlinear refractive index, and the local pulse energy. Assuming diffraction, the resulting contrast is 97.8% of the value obtained from simplified calculation with the flat-top beam. This result indicates that the numerical model can calculate with a single flat-top intensity value without introducing significant errors, which significantly increases calculation speed.

## 3.5 Optical components impacting the B-integral post-pulse mirroring

The impact of different optical components typically used in the CPA systems onto the generation and mirroring of post-pulses varies for the different types of components. Every transmissive optical component introduces B-integral to the propagating pulse due to the nonlinearity of refractive index and SPM. The magnitude of the B-integral depends on the intensity of the pulse, on the nonlinear refractive index of the medium, and on the thickness of the component.

Mirrors are used to change the propagation direction of the laser beam and to transport the beam between the individual components and subsystems (oscillator, amplifiers, stretcher, compressor, etc.). The most significant impact of mirrors for the mirroring of post-pulses to pre-pulses is from the rotation of linear polarization direction in complex beam paths, which is discussed in more detail in section 3.6.

In order to reproduce the intensity profile of the beam and to increase the beam size as the energy of the pulse increases, imaging optics such as lenses and spherical mirrors (often grouped to form telescopes) are used. Lenses introduce a medium with nonlinear refractive index into the beam path and add to the total B-integral of the system. Spherical or parabolic mirrors are typically used instead of lenses in order to avoid introducing radial dispersion and chromatic aberration.

Each amplifier of the CPA system contains one or more gain media for amplification of the pulse. In regenerative amplifiers, the gain medium is located inside an optical cavity together with polarizing optical components ensuring that the pulse can be locked in the cavity and after amplification extracted out. In multi-pass amplifiers, mirrors are used to direct the beam through the gain medium several times in order to efficiently extract the stored energy. The amplification increases the energy of the pulse, which in turn increases the impact of SPM. In CPA laser systems utilizing gain medium with natural birefringence (such as e.g. Ti:sapphire), incorrect alignment of the pulse polarization with respect to the optical axis of the gain medium leads to the generation of post-pulses. This process is described in section 3.2. Under thermal load, the gain medium typically exhibits stress-induced birefringence. The magnitude of the induced birefringence is much smaller than natural birefringence. In CPA amplifires utilizing isotropic gain media, the induced birefringence does not create significant difference in group velocity to produce post-pulses. In Ti:sapphire the induced birefringence is much smaller than natural birefringence, and the generation of pre-pulses is driven by the natural birefringence.

Some parts of the laser system require enclosing the beam path inside a vacuum chamber or in enclosure with controlled environment. Typically, the focused beam in a telescope with high enough focused intensity needs to be enclosed in a vacuum chamber to prevent nonlinear effects and ionization of air. Vacuum chambers and enclosures are equipped with transparent windows allowing the beam to propagate in and out. The transparent windows introduce material with nonlinear refractive index into the beam path and contribute to the B-integral.

The dispersion of the laser pulse can be controlled by static components such as chirped mirrors, prism/grating stretchers and compressors, and by inserting components with large material dispersion. Dynamic control of dispersion is possible by an acousto-optic programmable dispersive filter (AOPDF), also called dazzler [72, 73]. Prisms, high dispersion glass blocks with large material dispersion, and dazzlers all increase the B-integral.

In order to fully exploit the potential of a petawatt-class CPA laser system, the focusability of the output beam has to be ensured. The imaging optical components and systems introduce aberrations to the wavefront of the beam, which can be compensated by design, by the means of static phase correctors, and dynamically by deformable mirrors. Static phase correctors are typically transparent windows with inscribed variation of thickness, and the propagating beam obtains a corresponding B-integral.

The pulse in CPA systems is in general polarized, and typically the primary polarization state of the beam is linear polarization. A variety of polarization optical components are used in order to manipulate the polarization state of the beam. The individual impact of the optical components for manipulation of polarization is described in the following sections.

### 3.5.1 Polarizers

Polarizers are used to discriminate a certain polarization direction and to separate the orthogonal linear polarization states. There are many different types of polarizers with different properties. Some polarizers can be used in reflection, and some require the pulse to propagate through a certain thickness of material. Transmissive polarizers contribute to the total B-integral.

The impact of the polarizer on the pulse can be expressed through a Jones matrix. In most cases, properties of the polarizer can be considered frequency-independent, and the Jones matrix can be expressed in time domain as

$$\mathbf{J}_{\mathrm{pol}}(\theta) = \sqrt{\tau_{\mathrm{pol}}}\mathbf{R}^{-1}(\theta)\begin{pmatrix}1 & 0\\ 0 & \sqrt{\eta}\end{pmatrix}\mathbf{R}(\theta) \tag{3.63}$$

where $\tau_{\mathrm{pol}}$ is the transmittance of the polarizer independent of polarization, and $\eta$ is the intensity extinction ratio. The angle $\theta$ is between the reference $x$-axis and the transmission direction. In case the polarizer exhibits frequency dependence, the frequency domain Jones matrix

$$\tilde{\mathbf{J}}_{\mathrm{pol}}(\theta, \Omega, \omega_0) = \sqrt{\tau_{\mathrm{pol}}(\Omega + \omega_0)}\mathbf{R}^{-1}(\theta)\begin{pmatrix}1 & 0\\ 0 & \sqrt{\eta(\Omega + \omega_0)}\end{pmatrix}\mathbf{R}(\theta) \tag{3.64}$$

can be used instead.

Polarizers may impact the generation of pre-pulses from post-pulses introduced due to birefringence of the gain medium. If a post-pulse is generated in the birefringent gain medium in the polarization component orthogonal to the main pulse, the electromagnetic fields of the two pulses do not create modulated intensity, since the fields are in directions perpendicular with respect to each other. If the pulses pass through a polarizer, and the transmission axis of the polarizer is not precisely aligned with respect to the polarization of the main pulse, both the pulses partially project onto the direction of the polarizer transmission. The misalignment of the polarizer therefore leads to the superposition of the electromagnetic fields of the pulses and consequently to mirroring of the post-pulse to a pre-pulse. Any medium that allows only propagation of certain polarization states has a similar impact - this includes waveplates, Pockel's cells, birefringent media, and others.

### 3.5.2 Waveplates

Waveplates are used in laser systems to change the polarization state of the laser beam. Birefringent materials with well defined thickness are typically used to form the waveplate. The input electromagnetic field is decomposed into the two orthogonal polarization states propagating through the birefringent material. The directions of these polarization states are also called the fast and slow axis of the waveplate. The phase velocity of the wave corresponding to the fast axis is higher than the phase velocity corresponding to the slow axis. The difference in the phase obtained by the two waves after the propagation through the waveplate is called phase retardation. The most commonly used waveplates provide phase retardation of $2m\pi + \pi$ and $2m\pi + \frac{\pi}{2}$. The number $m$ is also called the order of the waveplate. Waveplates with $m = 0$ are called zero-order waveplates. The main advantage of zero-order waveplates is their better thermal stability of the phase retardation. For broad-bandwidth pulses used in CPA lasers, the dependence of the phase retardation on wavelength becomes important. Achromatic waveplates offer well defined phase retardation over large bandwidths.

The impact of the waveplate on the propagating beam can be described by a Jones matrix

$$\mathbf{J}_{\mathrm{wp}}(\theta) = \sqrt{\tau_{\mathrm{wp}}}\mathbf{R}(\theta)\begin{pmatrix} e^{-i\varphi_{\mathrm{r}}} & 0 \\ 0 & 1 \end{pmatrix}\mathbf{R}^{-1}(\theta) \tag{3.65}$$

with $\tau_{\mathrm{wp}}$ and $\varphi_{\mathrm{r}}$ being the transmittance and phase retardation of the waveplate. The angle $\theta$ is the angle between the local $x$-axis direction and the fast axis of the waveplate. For broad-bandwidth pulses, it is more convenient to express the Jones matrix in frequency domain as

$$\tilde{\mathbf{J}}_{\mathrm{wp}}(\theta, \Omega, \omega_0) = \sqrt{\tau_{\mathrm{wp}}(\Omega + \omega_0)}\mathbf{R}(\theta)\begin{pmatrix} e^{-i\varphi_{\mathrm{r}}(\Omega+\omega_0)} & 0 \\ 0 & 1 \end{pmatrix}\mathbf{R}^{-1}(\theta) \tag{3.66}$$

where $\Omega = \omega - \omega_0$.

Similarly to polarizers, the waveplate introduces mixing of the input orthogonal linear polarization components. In contrast with polarizers, this mixing is present independently of small misalignment of the waveplate from design position. The waveplate also contributes to the total B-integral in the system, even though this contribution is typically small compared to other components due to the small thickness of the waveplate.

Most common waveplates consist of a combination of quartz and magnesium fluoride. The B-integral from propagation through a component composed of two different materials with different thicknesses can be calculated as

$$\phi_{\mathrm{NL}}(\Omega) = \frac{\Omega + \omega_0}{c} n_{2,\mathrm{eff}}(L_1 + L_2) I\left(\frac{\Omega}{2\beta}\right) \tag{3.67a}$$

$$n_{2,\mathrm{eff}} = \frac{n_{21}L_1 + n_{22}L_2}{L_1 + L_2} \tag{3.67b}$$

where $n_{21}$, $n_{22}$ and $L_1$, $L_2$ are the nonlinear refractive indices and thicknesses of the two materials, respectively.

A less common achromatic waveplate with large precision of the phase retardation over large bandwidth utilizes birefringent polymer plate stacks on a fused silica glass substrate (manufactured by e.g. Astropribor). In such case the pulse propagates through the birefringent material and through the glass substrate. The contribution to the B-integral from the birefringent plate stack can be neglected due to small thickness compared to the glass substrate. For the contrast calculations presented in the later chapters, this type of waveplate can be considered as a combination of isotropic transparent window with an ideally thin waveplate.

### 3.5.3 Pockel's cells

Pockel's cells are devices that use linear electro-optic effect to manipulate the polarization of the propagating beam by an applied high voltage. In laser technology, Pockel's cells are used for intensity modulation in pulse pickers, for polarization switching inside regenerative amplifiers, and also for cleaning of the pre-pulse contrast on nanosecond time scale.

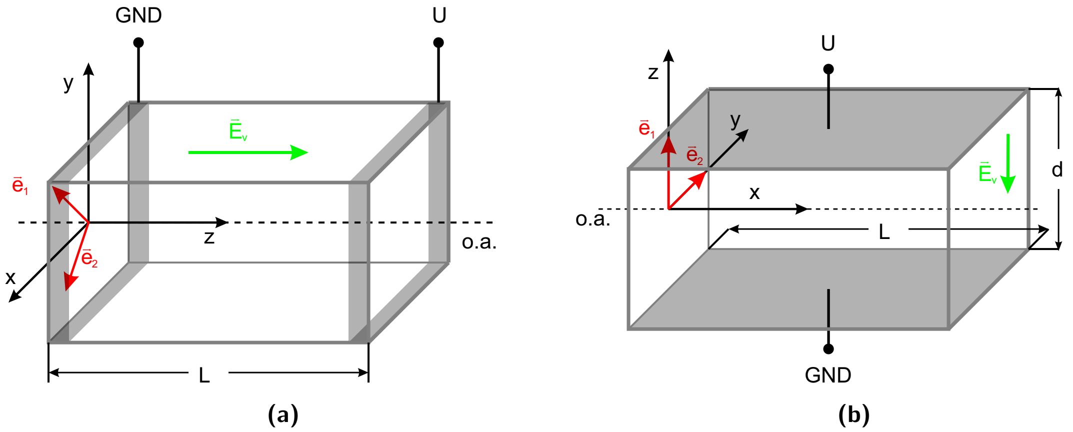

**Figure 3.9:** An example of a longitudinal and transverse Pockel's cell configuration: (a) longitudinal Pockel's cell, e.g. KDP and DKDP, (b) transverse Pockel's cell, e.g. $LiNbO_3$ and RTP.

Figure 3.9 shows an example of Pockel's cells in longitudinal and transverse configuration. In the longitudinal configuration used typically with KDP and DKDP Pockel's cells, the light propagates through the Pockel's cell crystal along the optical axis (o.a.). Without voltage applied, the polarization of the light is not affected by the cell except for small depolarization originating from crystal imperfections. Application of high voltage $U$ to the crystal creates an electric field $\vec{E}_v = \frac{U}{L}\vec{z}_0$ inside the crystal oriented in the direction of the optical axis. The eigenwaves $\vec{e}_1$ and $\vec{e}_2$ of the crystal with the voltage applied are linearly polarized at an angle of ±45° with respect to the crystallographic axis $x$

$$\vec{e}_{1,2} = \frac{1}{\sqrt{2}}\left(\vec{x}_0 \pm \vec{y}_0\right) \tag{3.68}$$

The electric field of the input pulse $\vec{E}_{in}$ coupled into the eigenwaves of the Pockel's cell can be calculated as

$$\vec{E}_1 = \frac{1}{\sqrt{2}}\begin{pmatrix} 1 & 1 \\ 1 & -1 \end{pmatrix}\vec{E}_{in} \tag{3.69}$$

The eigenwaves propagate through the Pockel's cell at different phase velocities, yielding a phase difference $\Delta\varphi = \varphi_2 - \varphi_1$. At the output of the DKDP crystal, the phase difference is

$$\Delta\varphi = \frac{2\pi n_o^3 r_{63} U}{\lambda} \tag{3.70}$$

where $n_o$ is the ordinary refractive index of the Pockel's cell crystal at wavelength $\lambda$ and $r_{63}$ is the nonzero coefficient of the electrooptic tensor for the given geometry of the electric field and beam propagation through the crystal. The internal electric field at the output of the Pockel's cell crystal is

$$\vec{E}_2 = \begin{pmatrix} 1 & 0 \\ 0 & e^{i\Delta\varphi} \end{pmatrix} \vec{E}_1 = \frac{1}{\sqrt{2}} \begin{pmatrix} 1 & 1 \\ e^{i\Delta\varphi} & -e^{i\Delta\varphi} \end{pmatrix} \vec{E}_{in} \tag{3.71}$$

The electric field of the pulse after passing through the Pockel's cell is then

$$\vec{E}_{out} = \frac{1}{\sqrt{2}} \begin{pmatrix} 1 & 1 \\ 1 & -1 \end{pmatrix} \vec{E}_2 = \frac{1}{2} \begin{pmatrix} 1 + e^{i\Delta\varphi} & 1 - e^{i\Delta\varphi} \\ 1 - e^{i\Delta\varphi} & 1 + e^{i\Delta\varphi} \end{pmatrix} \vec{E}_{in} \tag{3.72}$$

From the last equation it is clear that if the phase difference $\Delta\varphi = \pi$ for half-wave voltage $U_\pi$, the output electric field becomes

$$\vec{E}_{out} = \begin{pmatrix} 0 & 1 \\ 1 & 0 \end{pmatrix} \vec{E}_{in} \tag{3.73}$$

If the input pulse is linearly polarized and the direction of the pulse polarization is aligned with one of the crystallographic axes $x$ or $y$, the output pulse is linearly polarized with the polarization direction rotated by 90° from the polarization direction of the input pulse.
The Jones matrix of the DKDP Pockel's cell can be written as

$$\mathbf{J}_{\text{pc}}(\theta) = \frac{1}{2}\sqrt{\tau_{\text{pc}}}\mathbf{R}^{-1}(\theta) \begin{pmatrix} 1 + e^{i\Delta\varphi} & 1 - e^{i\Delta\varphi} \\ 1 - e^{i\Delta\varphi} & 1 + e^{i\Delta\varphi} \end{pmatrix} \mathbf{R}(\theta) \tag{3.74}$$

The angle $\theta$ is the angle between local $x$-axis and the crystallographic $x$-axis of the Pockel's cell crystal. For broad bandwidth pulses, the frequency domain Jones matrix is

$$\tilde{\mathbf{J}}_{\text{pc}}(\theta, \Omega, \omega_0) = \frac{1}{2}\sqrt{\tau_{\text{pc}}(\Omega + \omega_0)}\mathbf{R}^{-1}(\theta) \begin{pmatrix} 1 + e^{i\Delta\varphi(\Omega,\omega_0)} & 1 - e^{i\Delta\varphi(\Omega,\omega_0)} \\ 1 - e^{i\Delta\varphi(\Omega,\omega_0)} & 1 + e^{i\Delta\varphi(\Omega,\omega_0)} \end{pmatrix} \mathbf{R}(\theta) \tag{3.75}$$

with the phase retardation

$$\Delta\varphi(\Omega, \omega_0) = \frac{(\Omega + \omega_0) n_o^3 r_{63} U}{c} \tag{3.76}$$

The Pockel's cell contributes to the mirroring of post-pulses by mixing of orthogonal linear polarization components and by the B-integral. Additionally, KDP and DKDP Pockel's cells are typically enclosed in a housing with input and output window, since the KDP and DKDP crystals are hygroscopic [74].

### 3.5.4 Pulse picking with a Pockel's cell

Pulse picking and pre-pulse contrast cleaning are two applications of intensity modulation with a Pockel's cell. In the following text we refer to both as pulse picking, since the principle is identical. The most common setups for pulse picking are shown in figure 3.10a. The Pockel's cell is located between two crossed polarizers - $P_1$ and $P_2$. The input polarizer might be omitted if the polarization of the input pulses is well defined. A half-wave plate is used to properly orient the input pulse polarization with respect to the polarizers and the Pockel's cell. The typical time-dependent transmission through the setup is shown in figure 3.10b. With the Pockel's cell off, the input pulses are rejected by the polarizer $P_2$, and the transmission is minimal. Once half-wave voltage is applied to the cell, the polarization of the pulse is rotated, and the pulse is transmitted with transmittance $T_{\max}$. The minimum transmittance $T_{\min}$ is given by the reflection loss from the polarizer and cell faces, internal absorption, and extinction ratio of the polarizers. The maximum transmittance $T_{\max}$ is influenced by the reflection and absorption loss, and the applied voltage.

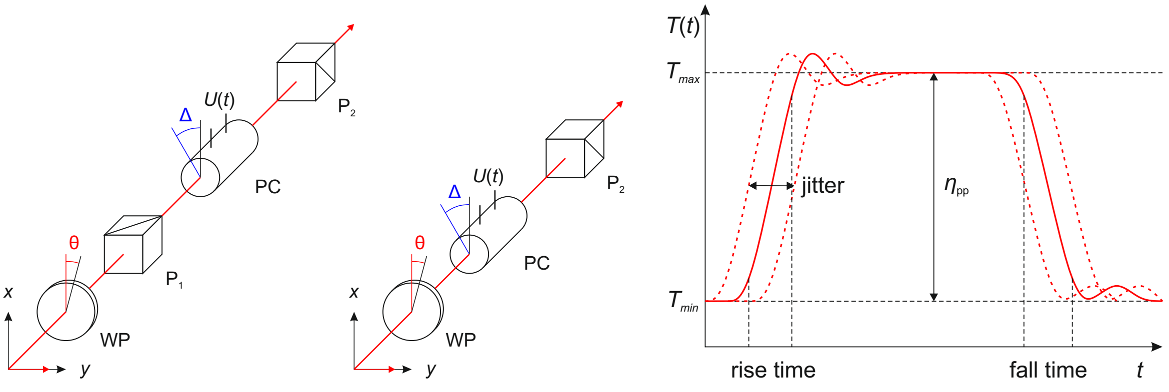

**(a)** **(b)**

**Figure 3.10:** Use of a Pockel's cell for pulse picking: (a) typical setups and (b) typical transmittance defined as $I_{\text{out}}(t)/I_{\text{in}}(t)$.

One of the most important characteristics of the pulse picker is the extinction ratio - ratio of the transmittance without voltage to the transmittance with voltage applied. The theoretical value can be derived utilizing the Jones calculus and using the equation for intensity corresponding to the Jones vector $\vec{E}$ in the form

$$I = |E_x|^2 + |E_y|^2 \tag{3.77}$$

where $E_x$ and $E_y$ are the two components of the Jones vector. Assuming ideal alignment of the input polarization, the extinction ratio of the pulse picker is in both configurations given by

$$\eta_{\text{pp}} = \frac{2\eta}{(\eta - 1)\cos(\Delta\varphi) + \eta + 1} \tag{3.78}$$

The best extinction is achieved when the applied voltage is equal to $U_\pi$ and the phase retardation is $\Delta\varphi = \pi$. In that case $\eta_{\text{pp}} = \eta$. The rejected pulses are in the best case attenuated by the factor given by the extinction ratio of the polarizers used. In reality, the extinction ratio limit given by the polarizers may not be reached due to the quality of the Pockel's cell. Also, the alignment of the pulse picker components must be performed carefully to avoid introduction of unnecessary loss to the selected pulse and to maintain the extinction ratio. For the setup with two polarizers, the transmittance with the Pockel's cell off is

$$T_{\text{off}}^{(2)} = \eta T_{\text{PC}} T_{\text{pol}}^2 T_{\text{wp}} \tag{3.79}$$

and the transmittance with the Pockel's cell under half-wave voltage can be calculated from

$$T_{\mathrm{on}}^{(2)} = T_{\mathrm{PC}} T_{\mathrm{pol}}^{2} T_{\mathrm{wp}} \Big[ |\cos(2\Delta)\cos(2\theta) + \sin(2\Delta)\sin(2\theta)\sqrt{\eta}|^2 + + |\sqrt{\eta}\cos(2\theta)\sin(2\Delta) - \eta\cos(2\Delta)\sin(2\theta)|^2 \Big] \tag{3.80}$$

where $T_{\mathrm{PC}}$, $T_{\mathrm{pol}}$ and $T_{\mathrm{wp}}$ are the polarization-independent transmittance of the Pockel's cell, polarizers and the waveplate, respectively. The polarizers are assumed to be identical, both having extinction ratio $\eta$. The angle $\theta$ is the angle between the input pulse polarization direction and the fast axis of the input half-wave plate. The angle $\Delta$ is the angle between the crystallographic $x$-axis of the Pockel's cell crystal and the rejection direction of the polarizer $P_2$. For the setup with a single polarizer, the transmittance with the Pockel's cell off is

$$T_{\mathrm{off}}^{(1)} = T_{\mathrm{PC}} T_{\mathrm{pol}} T_{\mathrm{wp}} \left[ \eta\cos^2(2\theta) + \sin^2(2\theta) \right] \tag{3.81}$$

and the transmittance with the Pockel's cell under half-wave voltage becomes

$$T_{\mathrm{on}}^{(1)} = T_{\mathrm{PC}} T_{\mathrm{pol}} T_{\mathrm{wp}} \left[ \cos^2(2\Delta - 2\theta) + \eta\sin^2(2\Delta - 2\theta) \right] \tag{3.82}$$

The index in the round bracket identifies the setup and corresponds to the number of polarizers. With the high voltage set to $U_\pi$, the extinction ratio becomes

$$\eta_{\mathrm{pp}}^{(2)} = \frac{\eta}{\left[\cos(2\Delta)\cos(2\theta) + \sin(2\Delta)\sin(2\theta)\sqrt{\eta}\right]^2 + \left[\sqrt{\eta}\cos(2\theta)\sin(2\Delta) - \eta\cos(2\Delta)\sin(2\theta)\right]^2} \tag{3.83}$$

for the setup with two polarizers. For the setup with single polarizer, the extinction ratio at $U_\pi$ depends on the angles $\theta$ and $\Delta$ as

$$\eta_{\mathrm{pp}}^{(1)} = \frac{\eta\cos^2(2\theta) + \sin^2(2\theta)}{\eta\sin^2(2\Delta - 2\theta) + \cos^2(2\Delta - 2\theta)} \tag{3.84}$$

Figure 3.11a shows the impact of the component alignment on the extinction ratio in the two pulse picker configurations. In both cases, the maximum achievable extinction ratio is identical, however, the extinction ratio is less sensitive to alignment in the setup with two polarizers. In figure 3.11b, the relative transmittance of the selected pulse is plotted as a function of the component alignment. If the Pockel's cell is well aligned and $\Delta \approx 0$, the transmittance for the selected pulse is identical in both setups - the solid red and blue curves are overlapping in the graph. Rotation of the Pockel's cell around the propagation direction decreases the maximum transmittance in the two polarizer setup, and introduces loss to the selected pulse. In the setup with single polarizer, the loss can be minimized by adjustment of the half-wave plate at the cost of the extinction ratio.

The transition between the open and closed state of the pulse picker is finite, and the switching speed depends on the electrical characteristics of the Pockel's cell and of the high voltage driver. Typically, the switching to half-wave voltage can be achieved within several nanoseconds to few tens of nanoseconds. With special drivers, the switching time can be reduced down to several hundreds of picoseconds. For contrast cleaning and for pulse picking from pulse trains with high repetition rates, the switching speed becomes important, since the transmission state must change between adjacent pulses separated by a very short time. During the transition to open state, the high voltage applied to the cell typically exhibits ringing, which leads to modulation of the transmitted intensity. The ringing can be minimized by proper design of the high voltage driver and by impedance matching of the high voltage switch and the Pockel's cell terminals.

Another important characteristic, especially for contrast cleaning, is the jitter of the transitions between the closed and open state with respect to the selected pulse. For suppression of the pre-pulses and

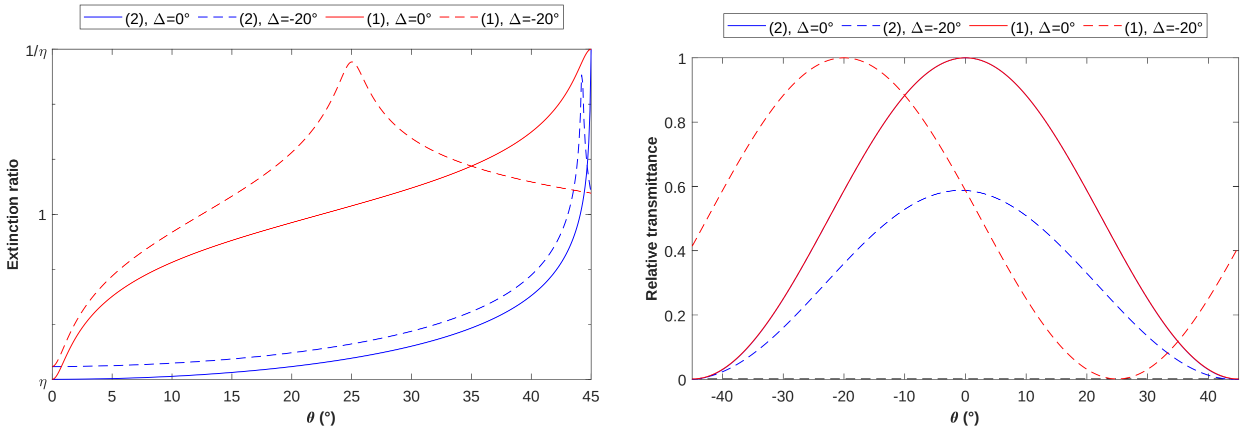

**(a)** **(b)**

**Figure 3.11:** Theoretical dependence of the characteristics of two common configurations of pulse picker: (a) extinction ratio as a function of angle $\theta$, (b) transmittance relative to the individual components as a function of angle $\theta$. Note that the solid red and blue curve in the graph (b) are overlapping.

pedestals appearing very close to the pulse, the opening of the pulse picker must be very fast and as close to the main pulse as possible. The jitter limits how close the high voltage rising edge can be pushed without introducing instability at the rising edge of the pulse. The jitter of the falling edge is typically not a problem for contrast cleaning, however, it may have impact for pulse picking from high repetition rate pulse trains.

For petawatt-class CPA laser systems where the pulse has considerable bandwidth and the pulse spectrum is mapped to time. The impact of the pulse picker on the transmitted pulse has to be considered. The transition to the open state must be completed and the high voltage stabilized before the arrival of the pulse, otherwise spectrum modulation may be introduced to the pulse. The timing can be typically optimized by adjusting the delay of the pulse picker through a delay generator. The components of the pulse picker setup introduce material dispersion to the optical path of the CPA pulse, which can be accounted for in the dispersion model of the system during design of the system. Dispersion from adding a pulse picker to an existing system can be usually compensated by the compressor and through the use of dazzler. The half-wave voltage $U_\pi$ required for achieving the maximum extinction ratio is a function of wavelength, and for a longitudinal KDP or DKDP Pockel's cell, it takes the form

$$U_\pi(\lambda) = \frac{\lambda}{2n_o^3(\lambda)r_{63}} \tag{3.85}$$

The wavelength dependence of the phase retardation $\Delta\varphi$ introduced by the Pockel's cell impacts the spectral transmittance of pulse picker when the voltage is applied. The phase retardation relative to $\pi$ as a function of wavelength for longitudinal DKDP Pockel's cell with the half-wave voltage set for three different wavelengths is shown in figure 3.12a. Figure 3.12b shows the resulting relative transmittance of the pulse picker for different wavelengths. As can be seen, the DKDP pulse picker provides over 100 nm of bandwidth.

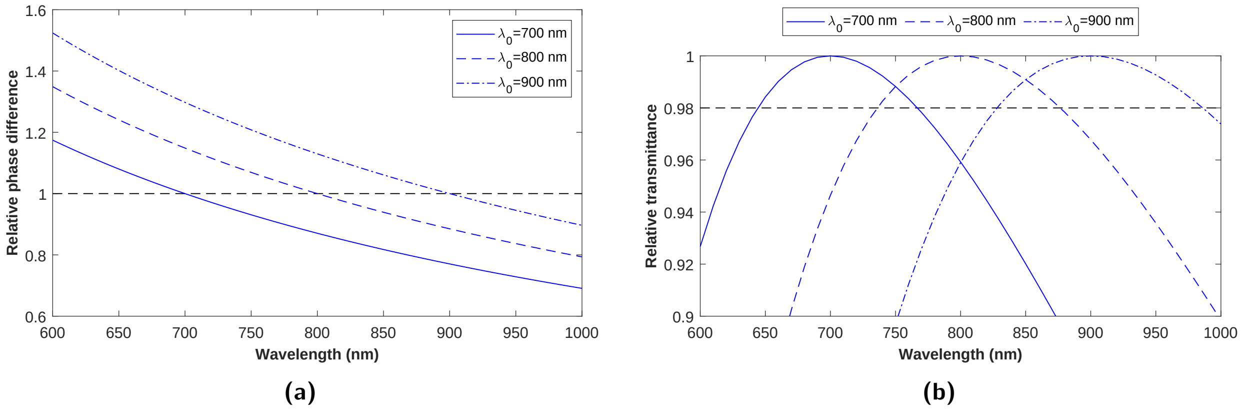

**Figure 3.12:** Wavelength dependence of the relative phase $\Delta\varphi(\lambda)$ of a DKDP Pockels cell (a), and relative transmittance for DKDP Pockel's cell between two crossed polarizers (b).

## 3.6 Polarization rotation in optical systems

The polarization state of light propagating through an optical path consisting of mirrors may change due to geometry of the optical path. This change is in some cases desired, since it may provide a crucial function for the optical system such as e.g. wavelength-independent 90° rotation of the polarization state. In other cases, it may degrade the performance of the optical system. A simple example of such change is a periscope increasing the beam height. When the periscope only changes beam height and the propagation direction remains, the polarization is unchanged. Rotating the top mirror around the vertical axis introduces rotation of the input polarization direction by the same angle as the angle between the input and output beam direction, measured in horizontal plane. Typically, the rotation of polarization can be expected in out-of-plane beam paths. The polarization rotation in complex beam paths can be evaluated using commercial ray tracing software, such as e.g. Zemax.

In this thesis, the contrast degradation is evaluated for the two power amplifiers of the L3-HAPLS laser system. The two amplifiers have very similar design and differ mainly in the number of passes, beam size, and cooling of the gain media. The multiplexing and relay imaging between individual amplification passes is realized by telescopes with 3f-$\frac{3}{2}$f imaging. These telescopes contain beam propagation in all three dimensions with relatively small angles of incidence on the mirrors, and introduce rotation of the linear polarization direction between the subsequent amplification passes. Each telescope was modelled in Zemax and the polarization rotation with respect to the direction of the optical axis in the gain medium was analyzed. The results are shown in figures 3.13 and 3.14.

The impact of the polarization rotation is best explained using figure 3.3, where it effectively creates the difference between the angles $\theta_2$ and $\theta_1$. Assuming that on the initial pass through the amplifier gain medium the polarization direction is aligned with the optical axis of the amplifier crystal, the rotation of polarization between first and second pass introduces a post pulse with polarization orthogonal to the polarization of the main pulse. The relative intensity of this post pulse is

$$C_{\perp}(\bar{x},\bar{y}) = \sin^2\theta_{12}(\bar{x},\bar{y}) \tag{3.86}$$

where $\theta_{12}(\bar{x},\bar{y})$ is the angle of polarization rotation between the first and second pass. After the second pass through the amplifier gain medium, the polarization of the main pulse and the post-pulse is rotated by the angle $\theta_{23}(\bar{x},\bar{y})$. Upon incidence of the pulses for the third pass through the gain medium, the post-pulse projects onto the same polarization direction as the main pulse with the relative intensity given by

$$C_1(\bar{x},\bar{y}) = \frac{G^\sigma}{G^\pi}\sin^2\left[\theta_{12}(\bar{x},\bar{y})\right]\tan^2\left[\theta_{23}(\bar{x},\bar{y})\right] \tag{3.87}$$

The ratio of the gain in $\sigma$ and $\pi$ polarization accounts for the difference in the gain of the post-pulse and the main pulse during the second amplification pass. The contrast of the electric field intensity and the factor $\gamma_1$ are

$$\sqrt{C_1(\bar{x},\bar{y})} = \left|\sqrt{\frac{G^\sigma}{G^\pi}}\sin\left[\theta_{12}(\bar{x},\bar{y})\right]\tan\left[\theta_{23}(\bar{x},\bar{y})\right]\right| \tag{3.88a}$$

$$\gamma_1(\bar{x},\bar{y}) = \operatorname{sign}\left\{\sin\left[\theta_{12}(\bar{x},\bar{y})\right]\tan\left[\theta_{23}(\bar{x},\bar{y})\right]\right\} \tag{3.88b}$$

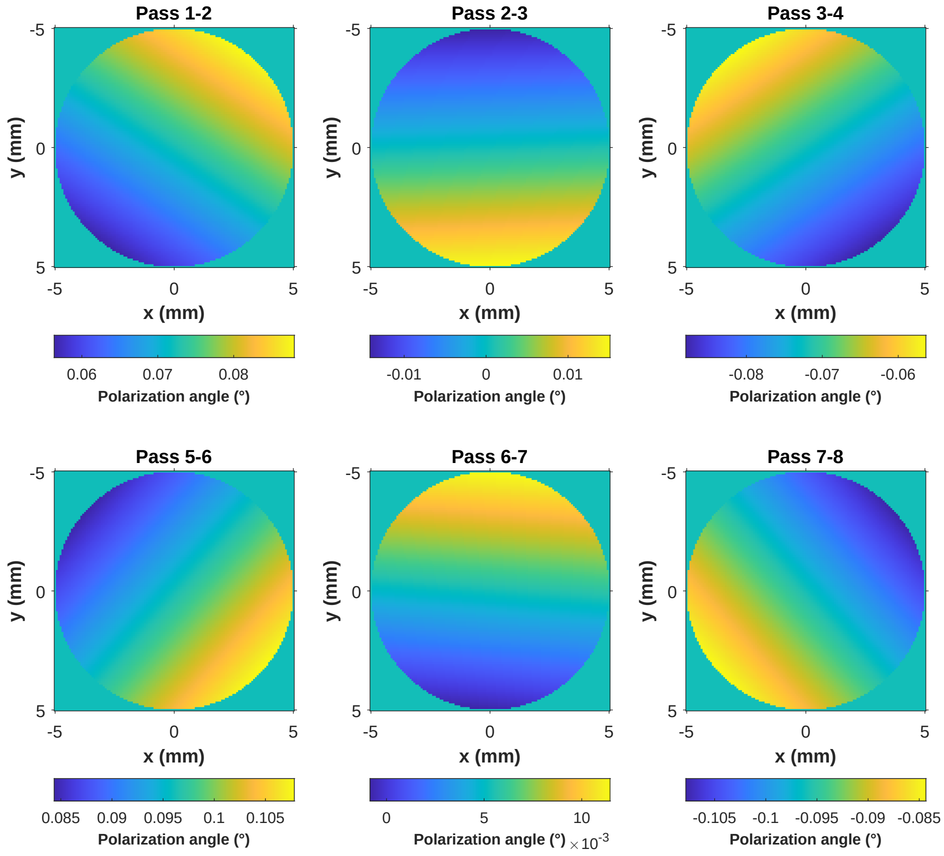

**Figure 3.13:** Rotation of the linear polarization direction by the telescopes between amplifier passes in Alpha amplifier of the L3-HAPLS laser system.

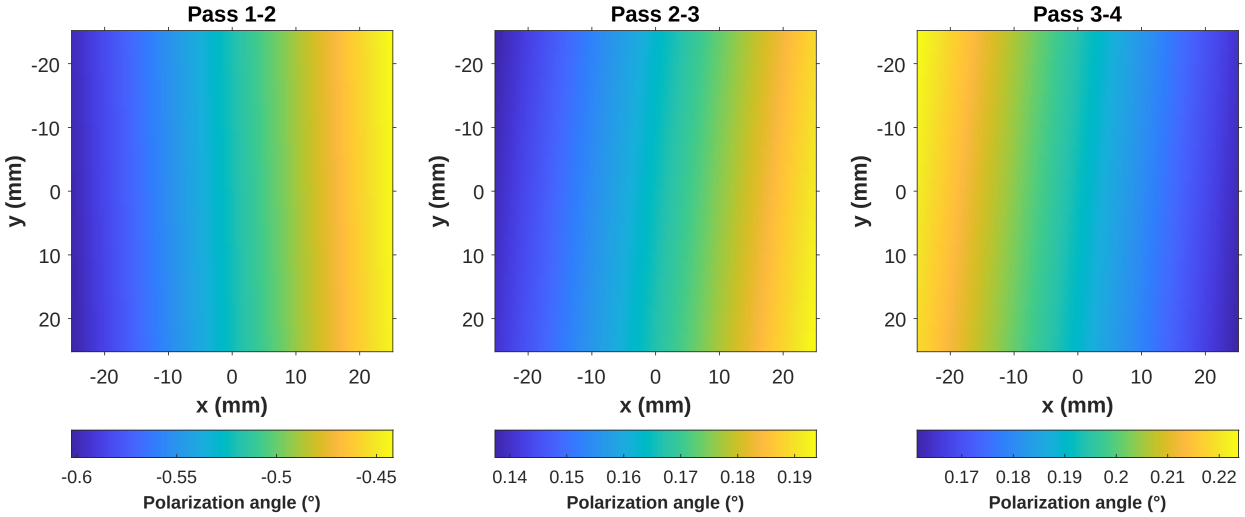

**Figure 3.14:** Rotation of the linear polarization direction by the telescopes between amplifier passes in Beta amplifier of the L3-HAPLS laser system.

# Chapter 4

# Characterization of local c-axis direction in large aperture Ti:sapphire crystals

The intensity of the post-pulses introduced due to birefringence as described in section 3.2 depends on the angle between the polarization of the pulse and the direction of the crystallographic c-axis of the amplifier crystal. For Ti:sapphire amplifiers with small beam area on the amplifier crystal, the angle changes mainly with the alignment of the crystal with respect to the input pulse. Scaling up the amplifiers to PW and multi-PW peak powers requires crystals with large aperture in the final amplification stages. Such crystals are difficult to grow with high homogeneity, and they can comprise multiple crystal grains with different orientation of the c-axis, separated by grain boundaries [75]. A method was developed to characterize the homogeneity of large aperture Ti:sapphire crystals. This method and the results from measurements of spare Ti:sapphire crystals for the Beta amplifier of the L3-HAPLS laser are described in this chapter.

## 4.1 Application of Jones calculus to the measurement of local c-axis orientation

Jones matrix formalism, described in more detail in section 2.4, was applied to develop a method for spatially resolved measurement of the orientation of optical axis in uniaxial birefringent crystals. The method is based on measurement of the light intensity transmitted through the measured sample placed in between two crossed, high-extinction-ratio polarizers (see figure 4.1). The transmitted intensity $I(x, y, \theta)$ is measured with a CCD camera as a function of rotation angle of the sample $\theta$. To ensure the spatial resolution of the measurement, imaging is employed from the sample to the second polarizer and from the second polarizer onto the camera. A polarized laser is used as a light source for the measurement. The method is suitable for measuring the projection of the optical axis onto the plane perpendicular to the axis of rotation of the measured sample.

Due to the imaging, the Jones matrix formalism can be used to calculate the theoretical dependence of the transmitted light intensity through a single point of the measured sample. The Jones matrices of the two crossed polarizers are given as

$$\mathbf{J}_{\mathrm{P1}} = \sqrt{\tau_P}\begin{pmatrix} 1 & 0 \\ 0 & \sqrt{\eta} \end{pmatrix} \quad \mathbf{J}_{\mathrm{P2}} = \sqrt{\tau_P}\begin{pmatrix} \sqrt{\eta} & 0 \\ 0 & 1 \end{pmatrix} \tag{4.1}$$

where $\eta$ is the intensity extinction ratio of the polarizers, and $\tau_P$ is the polarization independent transmittance. It is assumed that the measured sample is a crystal cut into the shape of a disk or a

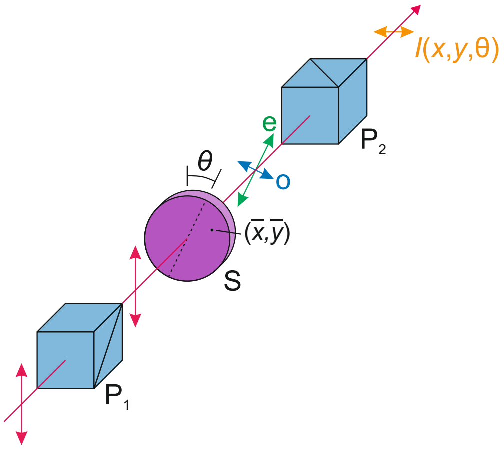

**Figure 4.1:** Schematic diagram showing the principle of the c-axis direction measurement. $P_1$, $P_2$ - polarizers with high extinction ratio, S - birefringent crystal sample, $\theta$ - angle of rotation of the sample.

slab of thickness $L(\bar{x}, \bar{y})$. A coordinate system $\bar{x}$, $\bar{y}$ is assigned to the sample in the plane of the slab surface. The thickness of the sample is not assumed constant, since the sample might have a wedge angle for mitigation of post-pulses from multiple reflections. The optical axis of the crystal lies in the plane of the sample and makes an angle $\theta_c$ with the $\bar{x}$-axis. The impact of the sample on polarization of light propagating under normal incidence can be then characterized by Jones matrix

$$\mathbf{J}_\mathrm{S}(\bar{x}, \bar{y}, \lambda) = \sqrt{\tau_S} \begin{pmatrix} \cos^2\theta_c(\bar{x}, \bar{y}) - e^{i\phi(\bar{x}, \bar{y}, \lambda)} \sin^2\theta_c(\bar{x}, \bar{y}) & \left(1 - e^{i\phi(\bar{x}, \bar{y}\lambda),}\right) \cos\theta_c(\bar{x}, \bar{y}) \sin\theta_c(\bar{x}, \bar{y}) \\ \left(1 - e^{i\phi(\bar{x}, \bar{y}, \lambda)}\right) \cos\theta_c(\bar{x}, \bar{y}) \sin\theta_c(\bar{x}, \bar{y}) & \sin^2\theta_c(\bar{x}, \bar{y}) + e^{i\phi(\bar{x}, \bar{y}, \lambda)} \cos^2\theta_c(\bar{x}, \bar{y}) \end{pmatrix} \tag{4.2}$$

which is a matrix of a general waveplate with transmission $\tau_S$, phase retardation $\phi(\bar{x}, \bar{y}, \lambda)$, and with angle $\theta_c(\bar{x}, \bar{y})$ between the fast/slow axis and the $\bar{x}$-axis. The phase retardation $\phi(\bar{x}, \bar{y}, \lambda)$ between the transmitted light polarized along the optical axis and perpendicular to the optical axis depends on the ordinary and extraordinary refractive indices of the sample material $n_o$, $n_e$, on wavelength $\lambda$, and on the thickness $L(\bar{x}, \bar{y})$ of the sample as

$$\phi(\bar{x}, \bar{y}, \lambda) = \frac{2\pi}{\lambda}(n_o - n_e)L(\bar{x}, \bar{y}) \tag{4.3}$$

Using the Jones matrices (4.1) and (4.2), the Jones matrix of the entire measurement setup can be written as

$$\mathbf{J}(\bar{x}, \bar{y}, \theta, \lambda) = \mathbf{J}_\mathrm{P2} \cdot \mathbf{R}(-\theta) \cdot \mathbf{J}_\mathrm{S}(\bar{x}, \bar{y}, \lambda) \cdot \mathbf{R}(\theta) \cdot \mathbf{J}_\mathrm{P1} \tag{4.4}$$

where the rotation matrices are utilized for rotation of the measured sample. The input polarization state of the laser source used for the measurement is assumed to be linear with direction aligned with the transmission axis of the input polarizer. The non-normalized Jones vector of the input polarization state can be therefore written as

$$\mathbf{E}_\mathrm{in} = \sqrt{I_0} \begin{pmatrix} 1 \\ 0 \end{pmatrix} \tag{4.5}$$

where $I_0$ is the intensity of the light from the laser source incident onto the input polarizer. The polarization state after passing through the system can be then written as

$$\mathbf{E}_\mathrm{out}(\theta) = \mathbf{J}(\bar{x}, \bar{y}, \theta, \lambda) \cdot \mathbf{E}_\mathrm{in} \tag{4.6}$$

The intensity of light after the second polarizer is the sum of the intensities of the two orthogonal polarization components, which can be written as

$$I = |E_x|^2 + |E_y|^2 = E_x E_x^* + E_y E_y^* \tag{4.7}$$

Using this equation, the formula for the transmitted intensity can be obtained in the form

$$I_{\text{out}}(\bar{x},\bar{y},\theta,\lambda) = \underbrace{I_0 \tau_S \tau_P^2 \eta}_{I_{\text{bg}}(\bar{x},\bar{y},\lambda)} + \underbrace{2(1-\eta) I_0 \tau_S \tau_P^2 (1-\cos\phi(\bar{x},\bar{y}))}_{I_{\text{mod}}(\bar{x},\bar{y},\lambda)} \cos^2\left[\theta+\theta_c(\bar{x},\bar{y})\right] \sin^2\left[\theta+\theta_c(\bar{x},\bar{y})\right] \tag{4.8}$$

As can be seen, the transmitted intensity consists of two terms. The first term is independent of the angle $\theta$, if the beam has homogeneous intensity distribution on the sample. This term is the background of the measurement, and is therefore denoted $I_{\text{bg}}$. The second term depends on the angle of rotation of the sample, and also on the phase retardation $\phi$. The amplitude of the intensity modulation from rotation of the sample depends on the spatial coordinates $\bar{x}$, $\bar{y}$, and wavelength $\lambda$. The second term tends to zero for sample thicknesses which yield the phase retardation to be close to any integer multiple of $2\pi$. In such case, the sample behaves as an isotropic medium and therefore it is not possible to recognize the direction of the optical axis $\theta_c$. If, on the other hand, the phase retardation is close to $(2p+1)\pi$, where $p \in \mathcal{N}_0$, the effect of birefringence is strongest and it is possible to extract the local optical axis direction.

## 4.2 Extracting the spatially resolved map of c-axis orientation

The method for extracting the spatially resolved orientation of the optical axis $\theta_c(\bar{x},\bar{y})$ can be derived from further analysis of the theoretical dependence (4.8) of the intensity transmitted to the CCD detector. The dependence of (4.8) on the angle of rotation of the sample $\theta$ is given by the product of the squares of sine and cosine of the angle $\theta + \theta_c(\bar{x},\bar{y})$. This means that the function (4.8) is symmetrical with respect to the point $-\theta_c(\bar{x},\bar{y})$, and the spatially resolved map of the optical axis orientation can be extracted from the intensity measured by the CCD as the angle of the sample which yields the minimum transmission.

The function $\cos^2[\theta+\theta_c(\bar{x},\bar{y})]\sin^2[\theta+\theta_c(\bar{x},\bar{y})]$ from (4.8) can be expanded into a Taylor series around point $-\theta_c(\bar{x},\bar{y})$. The resulting Taylor series contains only even terms, and for angles $|\theta+\theta_c| < 5°$, it can be well approximated only by the zero and second order terms. The transmitted intensity (4.8) using this approximation becomes

$$I_{\text{out}}(\bar{x},\bar{y},\theta) \approx I_{\text{bg}}(\bar{x},\bar{y},\lambda) + I_{\text{mod}}(\bar{x},\bar{y},\lambda)\left[\theta+\theta_c(\bar{x},\bar{y})\right]^2 , \tag{4.9}$$

The approximation of the transmitted intensity simplifies the processing of the intensity data from the CCD. The spatially resolved map of optical axis orientation can be extracted from several CCD images captured at different angle of rotation $\theta$. The images have to be transformed first to remove the rotation of the sample with respect to the camera. Next, a data set is created for each poiont $(\bar{x}_i,\bar{y}_i)$ in the measured area, containing the measured intensities $I_{ij}$ and corresponding sample rotation angles $\theta_j$. This data set is then fitted with a second order polynomial

$$f_i(\theta) = a_i + b_i\theta + c_i\theta^2 \tag{4.10}$$

Comparing the equations (4.9) and (4.10), the following set of equations relating the fit parameters $a_i$, $b_i$ and $c_i$ to the parameters of the measured sample and measurement setup are obtained

$$I_{\mathrm{bg},i} = a_i - \frac{b_i^2}{4c_i} \tag{4.11a}$$

$$\theta_{c,i} = -\frac{b_i}{2c_i} \tag{4.11b}$$

$$I_{\mathrm{mod},i} = c_i \tag{4.11c}$$

The second equation directly relates the parameters of the fit to the direction of the c-axis at point $(\bar{x}_i, \bar{y}_i)$ within the plane of the measured sample. Performing the polynomial fit and calculating (4.11b) for each point within the measured area therefore yields the spatially resolved map of the c-axis projection onto the plane perpendicular to the rotation of the sample.

## 4.3 Measurement of c-axis in large aperture Ti:Sapphire crystals

The method described in the previous sections was used to characterize several a-cut large aperture Ti:sapphire crystals with ≈10 cm diameter. The thickness of the samples ranged from 10 mm to 15 mm. The crystals are spare slabs for the Beta amplifier in the L3-HAPLS laser system.
The setup used for the measurement is shown schematically in the Figure 4.2. A beam from a commercial fiber-coupled CW laser (CrystaLaser IRCL-300-1053-S) is collimated using a fiber coupled collimator and expanded 3 times by a refractive telescope to overfill an adjustable aperture. The beam then passes through a λ/2 waveplate and polarizer with extinction ratio $>10^7$ (Thorlabs LPVIS100-MP2). The waveplate is used to adjust the direction of the linear polarization of the beam incident on the first polarizer. The beam is then expanded by another refractive telescope with 6.6 times magnification. After passing through the sample, the beam is demagnified and imaged onto a second high extinction ratio polarizer. Finally, the beam is imaged from the second polarizer onto a CCD camera (Basler acA 1600-20gm). The measured crystal sample is held in a mount that allows for rotation around the axis perpendicular to the face of the crystal.

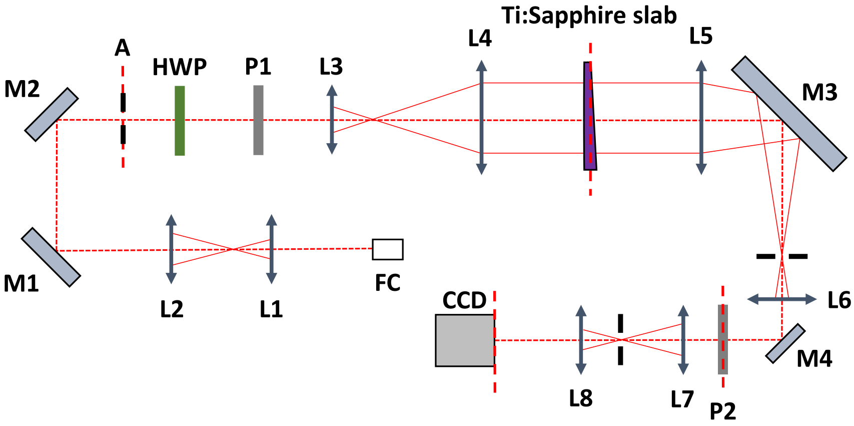

**Figure 4.2:** Setup used for spatially-resolved c-axis orientation measurement of large aperture Ti:sapphire crystals. FC - fiber collimator, L1 to L8- plano-convex lenses, M1 to M4 - high reflective mirrors, A - adjustable aperture, HWP - half-waveplate, P1 and P2 - high extinction ratio polarizers, CCD - CCD camera.

The map of projection of the c-axis onto the face of the crystal was extracted from the acquired images of the beam intensity passing through the crossed polarizers at different angles of rotation of the sample, as described in section 4.2. Positioning of the mirror M3 between telescope lenses L5 and L6 was not optimal with respect to polarization sensitivity of the measurement, but spatial restrictions did not allow to insert the mirror before the lens L5.

The sample sub-set of the CCD images acquired during measurement of the c-axis orientation of one of the crystal samples is shown in Figure 4.3. The relative angle of rotation of the sample is in the top left corner of each image. From the CCD images it is obvious that there is an area at the bottom left of the measured sample, where the c-axis is misoriented with respect to the rest of the crystal.

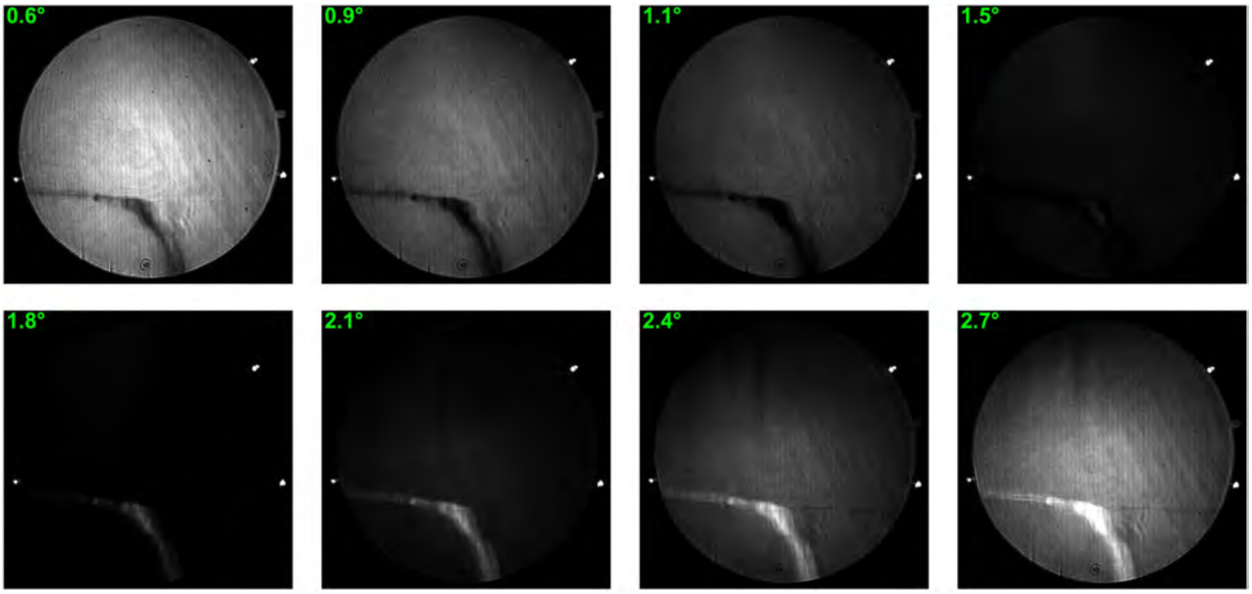

**Figure 4.3:** Transmitted intensity images acquired by the CCD camera during the measurement of the c-axis orientation within the Ti:sapphire crystal sample.

Figure 4.4 shows the results of the measurement for two different crystals obtained from the same parent boule. There is a clearly visible L-shaped area at the bottom left part of the measurement aperture, where the c-axis projection is misoriented with respect to the rest of the crystal. The vertical stripes in both images are introduced by the second polarizer. The mean deviation of the c-axis projection direction in Figure 4.4 a) is 0.4°, and the maximum deviation reaches up to 0.7°. The RMS direction of the c-axis projection is 0.12° within the L-shaped domain, and 0.09° outside the domain. The missing data in the c-axis map at the top of the measured area of Figure 4.4 b) are due to the phase term $1 - \cos\phi$ being close to zero in this area due to a wedge in thickness of the crystal. The wedge is <5 arcmin and was oriented in vertical direction.

The results of the presented measurements show that due to the complexity of the crystal growth process, large aperture Ti:sapphire crystals used in high-peak-power CPA laser systems can exhibit imperfections in the homogeneity of the direction of the crystallographic c-axis. It is one of the primary goals of this thesis to explore the influence of this c-axis direction inhomogeneity on the contrast performance of the pulse produced by amplifier systems containing crystals with such imperfections.

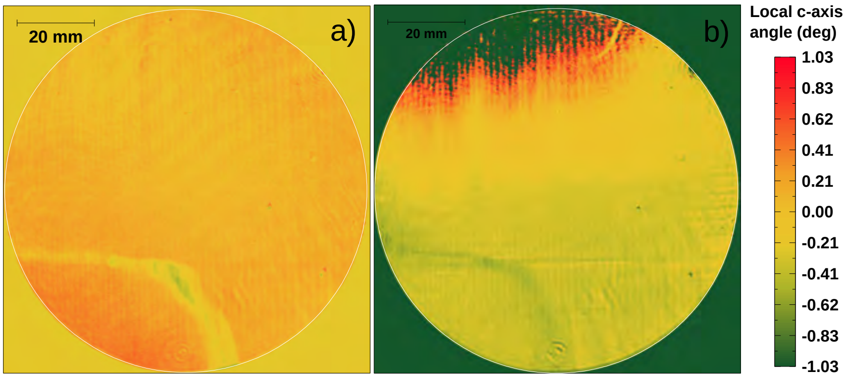

**Figure 4.4:** Measured c-axis projection direction map of two different Ti:sapphire crystals with 10 cm aperture extracted from the same parent boule.

## 4.4 Measurement with broad-bandwidth laser source

The dependence of the transmitted intensity (4.8) on the phase retardation $\phi(\bar{x},\bar{y},\lambda)$ between the ordinary and extraordinary waves propagating through the measured sample makes the above mentioned method unusable for birefringent crystal samples with phase retardation $\phi \approx 2p\pi$, where $p \in \mathcal{N}_0$. This limitation can be overcome if instead of a narrow-bandwidth laser source, a broadband laser or a swept-wavelength laser are used for the measurement. Typically, it can be assumed that the background intensity $I_{\text{bg}}$ and the modulation amplitude $I_{\text{mod}}$ in the equation (4.8) depend on the spatial coordinates $\bar{x}$, $\bar{y}$ and the wavelength $\lambda$ of the laser as

$$I_{\text{bg}}(\bar{x},\bar{y},\lambda) = I_0(\bar{x},\bar{y},\lambda)\tau_s\tau_p^2(\lambda)\eta(\lambda) \tag{4.12a}$$

$$I_{\text{mod}}(\bar{x},\bar{y},\lambda) = 2[1-\eta(\lambda)]I_0(\bar{x},\bar{y},\lambda)\tau_s\tau_p^2(\lambda)[1-\cos\phi(\bar{x},\bar{y},\lambda)] \tag{4.12b}$$

The CCD detector used to capture the transmitted intensity as a function of rotation of the sample effectively integrates the intensity over the spectrum of the laser source, and the resulting measured intensity is therefore

$$I_{\text{CCD}}(x,y,\theta) \approx \int_0^\infty I_{\text{bg}}(x,y,\lambda)d\lambda + [\theta+\theta_c(x,y)]^2\int_0^\infty I_{\text{mod}}(x,y,\lambda)d\lambda \tag{4.13}$$

The equations (4.11) then become

$$\int_0^\infty I_{\text{bg},i}(\lambda)d\lambda = a_i - \frac{b_i^2}{4c_i} \tag{4.14}$$

$$\theta_{c,i} = -\frac{b_i}{2c_i} \tag{4.15}$$

$$\int_0^\infty I_{\text{mod},i}(\lambda)d\lambda = c_i. \tag{4.16}$$

The second equation again gives the map of the orientation of the optical axis $\theta_{c,i}$ at points $(\bar{x}_i,\bar{y}_i)$. The advantage of this approach is illustrated by the figure 4.5. The graph on the left side shows the intensity incident on the CCD as a function of the wavelength $\lambda$ and sample rotation angle $\theta$.
As can be seen, for some wavelengths, the intensity is zero for all rotation angles. For such wavelengths $\lambda_p$, the term $1-\cos\phi(\bar{x},\bar{y})$ in equation (4.12b) is equal to zero and the following equation holds

$$\frac{2\pi}{\lambda_p}[n_o-n_e]L(\bar{x},\bar{y}) = 2p\pi, \tag{4.17}$$

where $p \in \mathcal{N}_0$.

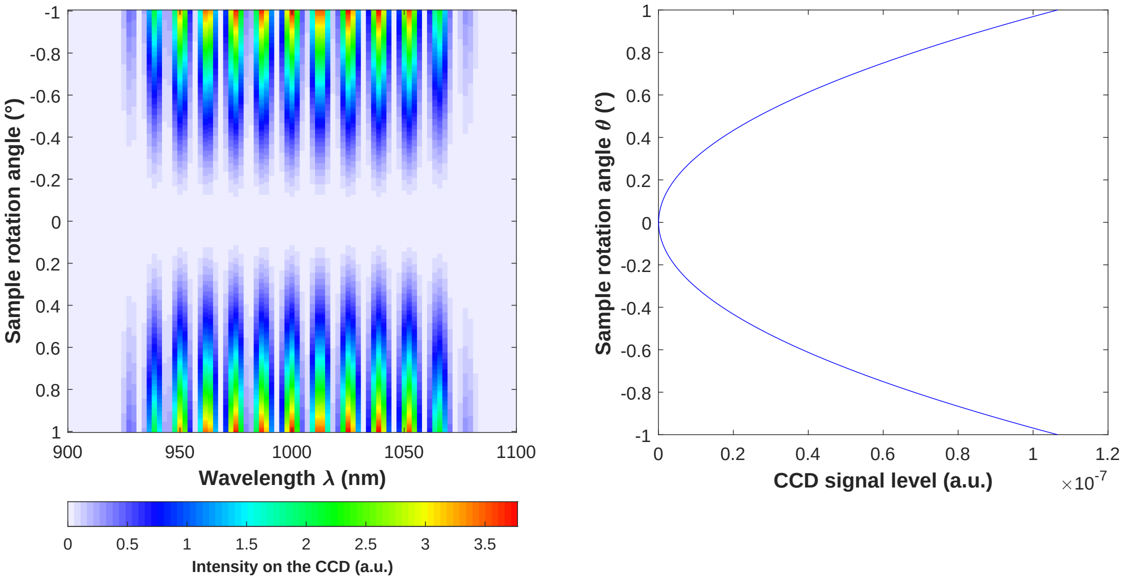

**Figure 4.5:** Transmitted intensity through the sample birefringent crystal and crossed polarizers with respect to the wavelength of the laser source and angle of rotation of the sample (left); resulting signal measured by the CCD detector as a function of the angle of rotation of the sample (right).

Since the laser is broad-bandwidth and the CCD integrates the intensity over the entire spectrum of the laser, the second integral in equation (4.13) is non-zero. Consequently, the coefficient $c_i$ of the fitting polynomial is also non-zero, and the equation for $\theta_{c,i}$ can be evaluated. The graph on the right side in figure 4.5 shows the integrated intensity measured by the CCD detector. The integrated intensity exhibits nearly quadratic dependence on sample rotation angle. The minimum bandwidth $\Delta\lambda$ required in order to overcome the limitation caused by phase retardation can be calculated from the equation

$$\Delta\lambda = 2L(n_e - n_o) + 2\sqrt{\lambda^2 + L^2(n_e - n_o)^2} \tag{4.18}$$

where $n_o$, $n_e$ are the ordinary and extraordinary refractive indices of the sample at wavelength $\lambda$, and $L$ is the sample thickness. $\Delta\lambda$ is derived from the condition that the difference in phase $\phi(\bar{x}, \bar{y})$ for wavelengths $\lambda - \Delta\lambda/2$ and $\lambda + \Delta\lambda/2$ is $2\pi$. The samples measured here have thickness between 10 and 20 mm, and require bandwidth of at least 14 nm at the center wavelength of 1053 nm, or 8 nm at the center wavelength of 800 nm.

A measurement of c-axis projection was performed using the broad-bandwidth laser pulses at the output of the L3-HAPLS laser front-end. The FWHM spectrum bandwidth of the pulses is 60 nm. The result of the measurement within the area of the L-shaped domain shown in figure 4.4 a) is presented in the figure 4.6. The result of the measurement is consistent with the measurement performed with the narrow-bandwidth source.

It is assumed in the equation (4.8) that the c-axis orientation is homogeneous along the thickness of the sample. In case of multiple spatially overlapping domains along the sample thickness, the interpretation of the c-axis projection measured using the above method becomes more complex. The measured projection is then influenced by the direction of c-axis in the individual domains as well as the mutual relationship of the phase retardation in individual domains (equivalent to the thickness of the domains). With a narrowband laser source, a grain boundary will appear as a quasi-periodic modulation

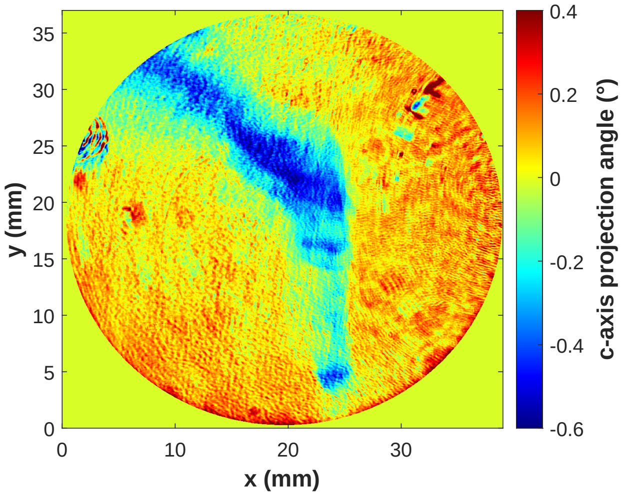

**Figure 4.6:** C-axis projection direction map of Ti:sapphire crystal with 10 cm aperture, measured with broad-bandwidth laser source with 60 nm bandwidth at the center wavelength of 807 nm.

in the c-axis projection measurement. The spatial frequency of the modulation is proportional to the gradient of change in domain thickness. The presence of multiple overlapping domains can be identified from the measured c-axis projection using the narrowband source, if the gradient $G$ of the domain thickness satisfies the condition

$$G >> \frac{\lambda}{a|n_e - n_o|} \tag{4.19}$$

where $a$ is the size of the measured sample aperture. With a broadband source having bandwidth given by equation (4.18), the influence of the mutual phase retardation is averaged out and the modulation is not present. The narrowband measurement is therefore useful for evaluation of the homogeneity along sample thickness. An ideal source for the measurement would be a narrow-band laser tunable over bandwidth greater than $\Delta\lambda$, allowing for recognition of multiple domains along sample thickness, and elimination of the insensitivity due to the phase term $1 - \cos\phi$.

## Chapter 5

# Numerical model of contrast degradation due to birefringence of amplifier gain medium

A numerical model was developed in order to study the impact of birefringence of the gain medium in high-focused-intensity CPA laser systems on the pre-pulse contrast of the resulting compressed pulse. The model calculates propagation of a stretched pulse with defined polarization state through individual optical components of a CPA laser amplifier system. The optical system assumed by the model can be a single optical component or a more complex system of optical components, such as e.g. CPA amplifier. The main code of the model is designed to read the required model parameters and the specification of the optical system from a text file, which increases its robustness. The evaluation of the optical system is performed in three main steps.

First step contains the initialization of the input pulse using the defined spectrum shape and dispersion of the stretcher. Two orthogonal polarization components are calculated, allowing for initialization of the input polarization state of the pulse. Alternatively, existing pre- and post-pulses can be added to the pulse. The output of the initialization phase are the two components of complex electric field intensity vector of the pulse.

In the second step of the evaluation, the main code reads the properties of the individual optical components along the propagation of the pulse and calculates the propagation of the electric field intensity. The schematic diagrams of the implementation of each type of optical component are shown in figure 5.7. For polarizers, waveplates, Pockel's cells, and birefringent media, the decomposition into the polarization states propagating through the component is calculated. The two polarization states are then transformed to frequency domain and the nonlinear spectral phase accumulated during the propagation is applied to the spectrum. For waveplates and Pockel's cells, the phase retardation is applied. For birefringent media, one of the polarization components is delayed by the amount corresponding to the thickness and type of the medium. In amplifiers, the propagation through the gain medium includes creating population inversion by absorption of the pump pulses. The population inversion after each pass of the pulse is considered as the initial population inversion for the next pass. The calculation of the accumulated B-integral in the gain medium includes the increase in the pulse intensity within the gain medium.

Finally, the compression of the pulse and the relative intensity pre-pulse background of the pulse are calculated. The dispersion of the compressor is added to the spectral phase of the pulse, and the polarization-dependent transmission of the compressor is applied.

The individual aspects of the implementation of the numerical model are described in the first sections of this chapter, followed by the description of implementation of individual types of optical components. The second part of this chapter is dedicated to validation of the model and description of the results of the numerical calculations for the power amplifiers of the L3-HAPLS laser system.

## 5.1 Definition and sampling of the pulse

For most CPA systems, it is convenient to define the pulse by it's spectrum at the input to the stretcher through the equation (2.19). The main advantage is that the pulse is assumed to be compressed, and the spectral phase can be assumed zero over the pulse bandwidth. The spectrum can be easily measured with a spectrometer. In principle, the spectrum shape can be arbitrary and the only limitation may be considered from the sampling of the pulse. In the calculations presented here the spectrum at the input to the stretcher is assumed to have the form

$$S_0(\lambda) = \left[1 + a_1\left(\frac{\lambda - \lambda_0}{\Delta\lambda_{\mathrm{FWHM}}}\right) + a_2\left(\frac{\lambda - \lambda_0}{\Delta\lambda_{\mathrm{FWHM}}}\right)^2\right] e^{-\ln 2\left(2\frac{\lambda-\lambda_0}{\Delta\lambda_{\mathrm{FWHM}}}\right)^m} \tag{5.1}$$

which is a modified $m$-th order supergaussian spectrum with linear and quadratic amplitude modulation, expressed in terms of wavelength $\lambda$. This spectral shape is convenient for the purpose of compensation of the pulse shape distortion during amplification. The bandwidth $\Delta\lambda_{\mathrm{FWHM}}$ can be defined to support the desired pulse duration after re-compression. We define the spectrum as a function of wavelength for convenience, since it can be easily compared with measurements. The wavelength and frequency are related through the equation

$$\lambda(\Omega) = \frac{2\pi c}{\Omega + \omega_0} \tag{5.2}$$

For amplifier systems with pulses without spatio-temporal couplings, the pulse is defined as

$$E(x, y, t) = \kappa S(x, y) A(t) e^{-i\varphi_t(t)} \tag{5.3}$$

and the spatial coordinates are independent of time and frequency. The energy of the pulse can be calculated by integrating the temporal intensity across time and beam profile

$$E_p = \iiint_{-\infty}^{\infty} I(x, y, t)\mathrm{d}x\mathrm{d}y\mathrm{d}t \tag{5.4}$$

A relationship between the temporal intensity and spectrum can be obtained using the Plancherel's theorem

$$\int_{-\infty}^{\infty} |E(x, y, t)|^2 \,\mathrm{d}t = \frac{1}{2\pi}\int_{-\infty}^{\infty} \left|\tilde{E}(x, y, \Omega)\right|^2 \mathrm{d}\Omega \tag{5.5}$$

Due to the equations (2.19) and (5.3)-(5.5), the pulse energy can be written as

$$E_p = \frac{1}{4\pi}\varepsilon_0 c\kappa^2 \iint_{-\infty}^{\infty} S^2(x, y)\mathrm{d}x\mathrm{d}y \int_{\infty}^{\infty} S_0(\Omega)\mathrm{d}\omega \tag{5.6}$$

and the scaling factor $\kappa$ is therefore

$$\kappa = \sqrt{\frac{4\pi E_p}{\varepsilon_0 c \iint_{-\infty}^{\infty} S^2(x, y)\mathrm{d}x\mathrm{d}y \int_{\infty}^{\infty} S_0(\Omega)\mathrm{d}\Omega}} \tag{5.7}$$

As was discussed in the section 3.4, for the calculation of pre-pulse contrast from post-pulse mirroring, the diffraction of the flat-top spatial beam profile can be neglected and the beam can be represented by a uniform distribution. For this reason, the numerical model represents the beam intensity distribution with a single uniform intensity value, and the initial spatial distribution function simplifies to

$$S(x,y) = \begin{cases} 1 & \text{for } (x,y) \in A_b \\ 0 & \text{otherwise} \end{cases} \tag{5.8}$$

where $A_b$ denotes the area of the beam. Introducing this simplification, the equation (5.7) can be written as

$$\kappa = \sqrt{\frac{4\pi E_p}{\varepsilon_0 c A_b \int_{\infty}^{\infty} A^2(t)\mathrm{d}t}} \tag{5.9}$$

The beam intensity and area are scaled throughout the calculation by the beam magnification $M$ between the different locations in the modelled laser system. With the increase of beam size by the magnification $M$, the intensity is reduced by $M^2$ to preserve the energy of the pulse.
The sampling of the pulse in time and frequency used by the numerical model is best explained on the case of propagation of the pulse through a transparent optical window of thickness $L$ - see figure 5.1. In time domain, the pulse amplitude $A(t)$ and phase $\varphi(t)$ are sampled on the interval $< -\frac{T}{2}, \frac{T}{2} >$ with uniform spacing $dt$. The time range $T$ is selected large enough to cover the entire stretched pulse. The spacing of the samples $dt$ can be calculated from the equation

$$dt = \frac{T}{r-1} \tag{5.10}$$

where $r$ is the number of samples. The spacing is selected small enough to provide sufficient resolution for the pulse and for the contrast features after compression. Since the pulse is most commonly stretched from ≈10 fs to ≈1 ns, the number of samples needs to be of the order of $2^{20}$.

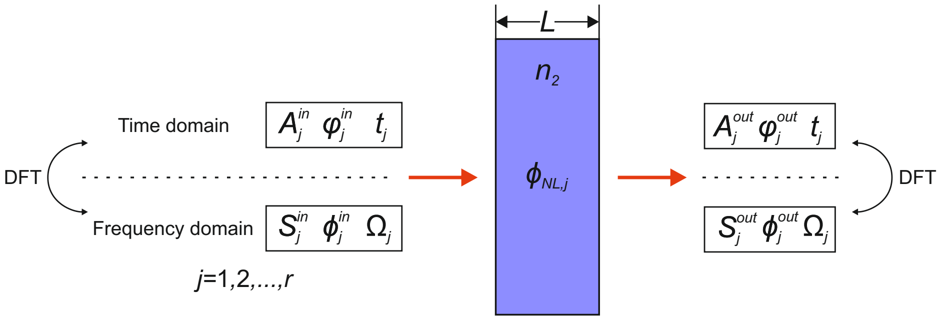

**Figure 5.1:** Sampling of the pulse for the case of propagation through transparent dielectric window.

The samples of time, amplitude, phase, complex electric field intensity, intensity, and nonlinear phase are calculated as

$$\left.\begin{aligned} t_j &= -\frac{T}{2} + (j-1)dt \\ A_j &= A(t_j) \\ \varphi_j &= \varphi(t_j) \\ E_j &= A_j e^{-i\varphi_j} \\ I_j &= \frac{1}{2} c\varepsilon_0 \left|E_j\right|^2 \\ \phi_{\mathrm{NL},j} &= \frac{1}{2}(\Omega_j + \omega_0) n_2 \varepsilon_0 L \left|E_j\right|^2 \end{aligned}\right\} \quad \text{for } j = 1, 2, \ldots, r \tag{5.11}$$

In frequency domain, the spectrum $S(\Omega)$ and spectral phase $\phi(\Omega)$ are sampled on the interval from $-\frac{\Delta\Omega}{2}$ to $\frac{\Delta\Omega}{2}$ with uniform spacing $d\Omega$. The samples of the frequency, spectrum, spectral phase, complex frequency domain electric field intensity, and instantaneous frequency are

$$\left.\begin{aligned} \Omega_j &= -\frac{\Delta\Omega}{2} + (j-1)d\Omega \\ S_j &= S(\Omega_j) \\ \phi_j &= \phi(\Omega_j) \\ \tilde{E}_j &= \sqrt{S_j}e^{-i\phi_j} \\ \omega_j &= \Omega_j + \omega_0 \end{aligned}\right\} \quad \text{for } j = 1, 2, ..., r \tag{5.12}$$

The model mainly operates with the complex electric field intensity $E_j$ and its frequency domain equivalent $\tilde{E}_j$, other quantities are calculated when needed. Similarly to equations (2.6) for the continuous functions, discrete Fourier transform (DFT) is used to transform the pulse between the time and frequency domain. The direct and inverse DFT are defined as

$$\tilde{E}_{k+1} = \sum_{n=0}^{r-1} E_{n+1} e^{-i\frac{2\pi}{r}kn} \tag{5.13a}$$

$$E_{n+1} = \frac{1}{r}\sum_{k=0}^{r-1} \tilde{E}_{k+1} e^{i\frac{2\pi}{r}kn} \tag{5.13b}$$

Due to the DFT, the frequency range $\Delta\Omega$ is connected with the sampling interval $dt$ through the relationship

$$\Delta\Omega = \frac{2\pi}{dt} \tag{5.14}$$

Under the assumption of the linear chirp, the time and frequency domain are connected through time-frequency correspondence (2.26). We require that the frequency corresponding to the time $\frac{T}{2}$ is equal to $\frac{\Delta\Omega}{2}$ for positive chirp, and $-\frac{\Delta\Omega}{2}$ for negatively chirped pulse. If we assume that the number of samples $r = 2^u + 1$ where $u \in \mathbb{N}$, we obtain the following equation for the frequency range

$$\Delta\Omega = \mathrm{sign}(\beta)\sqrt{|\beta|\pi 2^u} \tag{5.15}$$

This choice of the sampling of the pulse in time and frequency domain ensures that the instantaneous frequency $\omega_j = \omega_0 + 2\beta t_j$ matches the frequency $\Omega_j + \omega_0$ for $j = 1, 2, ..., 2^u + 1$. The spectral phase $\phi_{j,\mathrm{NL}}$ from SPM and XPM in the optical components in the CPA system can be therefore calculated from the temporal intensity $I_j$ and directly applied to the spectrum as

$$\tilde{E}_j^{\mathrm{out}} = \tilde{E}_j^{\mathrm{in}} e^{-i\phi_{j,\mathrm{NL}}} \tag{5.16}$$

The process of initialization of the pulse is shown in figure 5.2. First, the spectrum $S_j$ is defined for the compressed pulse at the stretcher input. The magnitude of the spectrum is scaled to match the pulse energy. The spectral phase $\phi_j$ is assumed to be zero for all $j = 1, 2, ..., r$. The quadratic approximation of the spectral phase of the stretcher is added to the pulse, yielding the stretched pulse complex spectral electric field intensity $\tilde{E}_j$. The frequency representation of the pulse is then transformed to time domain using the inverse DFT.

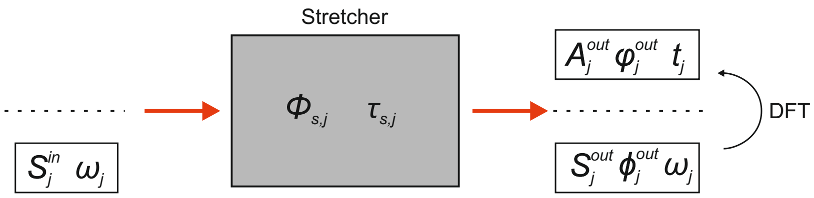

**Figure 5.2:** Process of initialization of the pulse in the numerical model.

## 5.2 Implementation of DFTs in Matlab

The Matlab functions `fft` and `ifft`, representing the discrete Fourier transforms 5.13 do not preserve the absolute value of the field when the electric field intensity is transformed to frequency domain and back to time domain. The transforms need to be scaled by the factors

$$C_{\text{fft}} = dt \tag{5.17a}$$

$$C_{\text{ifft}} = \frac{r d\omega}{2\pi} \tag{5.17b}$$

to preserve the amplitudes of the electric field. The functions `fftshift` and `ifftshift` are used to manipulate the electric field vectors to ensure the position of the center frequency of the pulse and of the zero time are matching with the frequency and time vectors. The following code listing summarizes the implementation of the DFTs in Matlab used in the numerical model

```
S = fftshift(Cfft*fft(E,r,2));
E = Cifft*ifft(ifftshift(S),r,2);
```

## 5.3 Modeling of pulse amplification

The amplification in conventional laser amplifiers is based on the process of stimulated emission. Figure 5.3 shows the energy level diagram for a 3-level and 4-level gain medium with indicated transitions during the operation of a laser amplifier. The dynamic of the amplification process can be derived from rate equations describing the rate of change in photon density and in population density of the individual energy levels in the gain medium. The equations were solved analytically for the amplification of narrow-band pulses by Franz and Nodovik [76]. In a conventional laser amplifier, the energy is first stored into the gain medium through the pumping mechanism, creating population inversion between the initial and terminal laser level. The analytic solution of Franz and Nodovik does not include the mechanism of pumping, but it can be easily extended for the case of optical pumping, due to the similarity between the absorption process and stimulated emission process. During the propagation through the gain medium with population inversion, the seed pulse with optical frequency matching the photon frequency corresponding to the energy difference between the initial and terminal laser level is amplified. The amplification process reduces the population inversion in the gain medium, leading to saturation of the amplifier gain when the pulse reaches the saturation intensity. The numerical model of the amplification process, including the optical pumping through absorption, is described in the following sections.

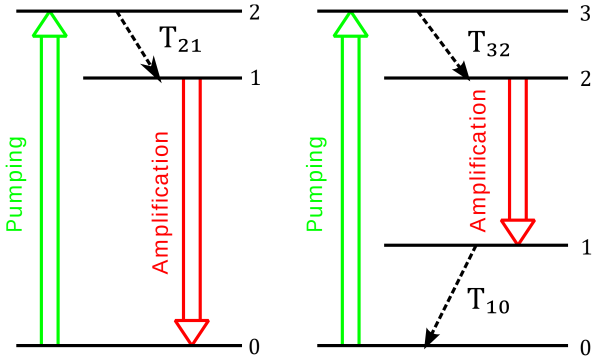

**Figure 5.3:** Diagram of energy levels and transitions in a 3-level (left) and 4-level (right) laser gain medium.

### 5.3.1 Analytic expressions for narrow-bandwidth pulse amplification

The numerical model of the pulse amplification in a laser gain medium presented in this thesis is based on the 1D analytic equations for population inversion density $\Delta(z,t)$ and photon density $p(z,t)$ during narrow-band pulse amplification derived by Frantz and Nodovik. The population inversion density of the gain medium and photon density of the pulse can be written as

$$\Delta(z,t) = \frac{\Delta_0(z)\exp\left[-\sigma\int_0^z \Delta_0(z')dz'\right]}{\exp\left[\gamma\sigma c\int_{-\infty}^{t-z/c} p_0(t')dt'\right] + \exp\left[-\sigma\int_0^z \Delta_0(z')dz'\right] - 1} \tag{5.18a}$$

$$p(z,t) = \frac{p_0(t-z/c)}{1-\left\{1-\exp\left[-\sigma\int_0^z \Delta_0(z')dz'\right]\right\}\exp\left[-\gamma\sigma c\int_{-\infty}^{t-z/c} p_0(t')dt'\right]} \tag{5.18b}$$

where $\sigma$ is the emission cross section of the gain medium at the wavelength of the amplified pulse, $\gamma$ is the population inversion reduction factor ($\gamma = 2$ for a 3-level gain medium and $\gamma = 1$ for a 4-level medium), $c$ is speed of light in vacuum, $\Delta_0(x)$ is the initial population inversion density and $p_0(t)$ is the photon density of the input pulse. This analytic solution of the rate equations assumes no spontaneous emission or pumping during the amplification process. The equations (5.18a) and (5.18b) describe amplification if the population inversion density $\Delta > 0$, and absorption if $\Delta < 0$.

### 5.3.2 Numerical model of broad-bandwidth pulse amplification in anisotropic medium

As was described in chapter 2, the spectrum of a chirped pulse in a CPA amplifier is mapped to time due to nearly-linear chirp. The emission cross section $\sigma$ of the gain medium depends on the angular frequency of the electromagnetic field: $\sigma \equiv \sigma(\omega)$. The equation 2.26 shows the dependence of the instantaneous frequency on time within the chirped pulse. For anisotropic media, the absorption and emission cross sections depend on the polarization of the electromagnetic wave in the medium. Typically, the geometry of the gain medium and the amplifier multiplexing are selected in such a way, that the beam propagates along the optical axis or in the direction perpendicular to the optical axis. The emission cross section for eigenwaves with polarization parallel and perpendicular to the optical axis are usually denoted with the Greek letters $\pi$ and $\sigma$, respectively.

Due to the dependence of emission cross section on frequency, the equations (5.18a) and (5.18b) cannot be used for the description of amplification of a pulse with broad bandwidth and time-dependent instantaneous frequency, since the important assumption during their derivation was that the emission cross section is time-independent. However, the equations can be solved numerically under the following assumptions:

1. The pulse is coupled into the $\pi$ and $\sigma$ polarization components in the medium with photon densities $p_0^\pi(t)$ and $p_0^\sigma(t)$.
2. The pulse is finite in time, and the photon densities $p_0^\pi(t)$ and $p_0^\sigma(t)$ are nonzero for $-\frac{T}{2} \leq t \leq \frac{T}{2}$ and zero otherwise.
3. The photon densities of the pulse can be sampled at times $t_i$, $i = 0, 1, ..., N_t$ on the interval $\left\langle -\frac{T}{2}, \frac{T}{2} \right\rangle$. The samples at time $t_i = i\Delta t - \frac{T}{2}$ are $p_{0i}^\pi = p_0^\pi(t_i)$ and $p_{0i}^\sigma = p_0^\sigma(t_i)$. The spacing $\Delta t$ between the samples is uniform and $\Delta t = \frac{T}{N_t}$ with $N_t$ being the total number of samples. The sampling is illustrated in figure 5.4a.
4. The photon density on each interval $\langle t_{i-1}, t_i \rangle$ can be considered as a sub-pulse that propagates through the gain medium independently of the photon density at times $> t_i$.
5. The saturation of the gain medium by each sub-pulse is small - the number of samples $N_t$ is large enough to satisfy this assumption.
6. The instantaneous frequency $\omega_i$ at time $t_i$ can be considered constant over the interval $\langle t_{i-1}, t_i \rangle$. The sampling is shown in figure 5.4b.
7. The population inversion is sampled on the interval $\langle 0, L \rangle$ with $L$ being the length of the active medium. The $j$-th sample at position $z_j = j\Delta z$ is $\Delta_0 j = \Delta_0(z_j)$, where $j = 0, 1, ..., N_z$ and $\Delta z = \frac{L}{N_z}$.
8. The population inversion density calculated from propagation of the $i$-th sub-pulse is used as an initial population inversion density for the following sub-pulse. The propagation of the first pulse assumes the population inversion density $\Delta_{0j}$.
9. The $i$-th sub-pulse traverses the gain medium of length $L$ in $\frac{L}{c}$ and emerges at the output of the gain medium at time interval $\left\langle t_{i-1} + \frac{L}{c}, t_i + \frac{L}{c} \right\rangle$. The material dispersion is not assumed.

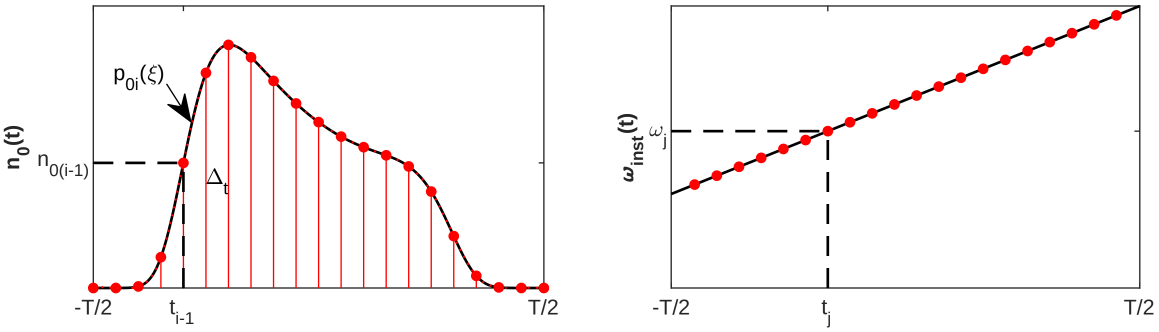

**(a)** Photon density **(b)** Instantaneous frequency

**Figure 5.4:** Sampling of the pulse for calculation of broad-bandwidth amplification using Frantz-Nodvik analytic equations for narrow-band amplification.

The photon density of the $i$-th sub-pulse can be approximated with cubic spline interpolation as $s_{0i}^{\pi}(\xi)$ and $s_{0i}^{\sigma}(\xi)$. On each interpolation interval $\langle t_{i-1}, t_i \rangle$ , $i = 1, 2, ..., N_t$, the cubic function $s_{0i}^{(k)}(\xi)$ has the form

$$s_{0i}^{(k)}(\xi_i) = \begin{cases} a_i^{(k)} + b_i^{(k)}\xi_i + c_i^{(k)}\xi_i^2 + d_i^{(k)}\xi_i^3 & \text{for } \xi_i \in < 0, 1 > \\ 0 & \text{otherwise} \end{cases} \tag{5.19}$$

where $(k) = \pi, \sigma$. The parameter $\xi_i$ relates to time $t$ as

$$\xi_i = \frac{t - t_{i-1}}{\Delta t_i} \tag{5.20}$$

Considering the length of the gain medium and the time needed for the sub-pulse to traverse the medium, the time integral of the photon density in equations (5.18a) and (5.18b) for the $i$-th sub-pulse at the times $t_{i-1}$ and $t_i$ can be simplified to

$$\int_{-\infty}^{t_{i-1}} p_0^{(k)}(t')dt' \approx \int_{t_{i-1}}^{t_{i-1}} s_{0i}^{(k)}\left(\frac{t - t_{i-1}}{\Delta t_i}\right) dt = 0 \tag{5.21a}$$

$$\int_{-\infty}^{t_i} p_0^{(k)}(t')dt' \approx \int_{t_{i-1}}^{t_i} s_{0i}^{(k)}\left(\frac{t - t_{i-1}}{\Delta t_i}\right) dt = \Delta t_i \left(a_i^{(k)} + \frac{b_i^{(k)}}{2} + \frac{c_i^{(k)}}{3} + \frac{d_i^{(k)}}{4}\right) = \mathcal{S}_{0i}^{(k)}\Delta t_i \tag{5.21b}$$

An equation for population inversion can be derived from the equation (5.18a) under the assumption of small gain saturation in the gain medium by the individual sub-pulses. In this approximation, the amplification of the $\sigma$ and $\pi$ polarization components can be evaluated independently. For simplification of the equations, small signal gain $G_0^{(k)}(z)$ and saturation factor $f^{(k)}(t)$ are defined as

$$G_0^{(k)}(z) = \exp\left[\sigma^{(k)} \int_0^z \Delta_0(z')dz'\right] \tag{5.22a}$$

$$f^{(k)}(t) = \exp\left[\gamma\sigma^{(k)} c \int_{-\infty}^{t} p_0^{(k)}(t')dt'\right] \tag{5.22b}$$

Introducing small signal gains and saturation factors into the equation (5.18a) simplifies the equation to the form

$$\Delta^{(k)}(z, t) = \frac{\Delta_0(z)}{\left[f^{(k)}(t) - 1\right] G_0^{(k)}(z) + 1} \tag{5.23}$$

Reduction of the population inversion $\delta^{(k)}(z, t)$ by the polarization component $(k) = \pi, \sigma$ can be then written as

$$\delta^{(k)}(z, t) = \Delta^{(k)}(z, t) - \Delta_0(z) = -\frac{\Delta_0(z)\left[f^{(k)}(t) - 1\right] G_0^{(k)}(z)}{\left[f^{(k)}(t) - 1\right] G_0^{(k)}(z) + 1} \tag{5.24}$$

The population inversion after propagation of the corresponding sub-pulses in both polarization components can be written as

$$\Delta(z, t) = \Delta_0(z) + \left[\delta^{(\pi)}(z, t) + \delta^{(\sigma)}(z, t)\right] \tag{5.25}$$

The last two equations yield

$$\Delta(z, t) = \frac{\Delta_0(z)\left[1 - \left(f^{\pi}(t) - 1\right)\left(f^{\sigma}(t) - 1\right) G_0^{\pi}(z)G_0^{\sigma}(z)\right]}{\left[\left(f^{\pi}(t) - 1\right) G_0^{\pi}(z) + 1\right]\left[\left(f^{\sigma}(t) - 1\right) G_0^{\sigma}(z) + 1\right]} \tag{5.26}$$

Introducing the sampling and approximation of the photon density between the sub-pulses into the equations (5.18a) and (5.18b), the following numerical solution is obtained

$$\Delta_{ij} = \frac{\Delta_{(i-1)j}\left[1-(f_i^{\pi}-1)(f_i^{\sigma}-1)G^{\pi}_{(i-1)j}G^{\sigma}_{(i-1)j}\right]}{\left[(f_i^{\pi}-1)G^{\pi}_{(i-1)j}+1\right]\left[(f_i^{\sigma}-1)G^{\sigma}_{(i-1)j}+1\right]} \tag{5.27a}$$

$$G_{ij}^{(k)} = \exp\left[\sigma^{(k)}_{(i+1)}D_{ij}\right] \tag{5.27b}$$

$$f_i^{(k)} = \exp\left[\gamma c\sigma_i^{(k)}\mathcal{S}^{(k)}_{0i}\Delta t_i\right] \tag{5.27c}$$

$$p_i^{(k)} = \frac{s^{(k)}_{(i+1)N_z}(0)+s^{(k)}_{iN_z}(1)}{2} \tag{5.27d}$$

$$s^{(k)}_{(i+1)N_z}(0) = \frac{p^{(k)}_{0i}}{1-\left\{1-1/G^{(k)}_{iN_z}\right\}} \tag{5.27e}$$

$$s^{(k)}_{iN_z}(1) = \frac{p^{(k)}_{0i}}{1-\left\{1-1/G^{(k)}_{(i-1)N_z}\right\}\left[f_i^{\pi}f_i^{\sigma}\right]^{-1}} \tag{5.27f}$$

$$D_{ij} = \mathrm{NI}_{m=1}^{j}\left[\Delta_{im}, z_m\right] \tag{5.27g}$$

$$p_0^{(k)} = \frac{s^{(k)}_{1N_z}(0)}{2} \tag{5.27h}$$

$$p_{N_t}^{(k)} = \frac{s^{(k)}_{N_tN_z}(1)}{2} \tag{5.27i}$$

where $i = 1, 2, ..., N_t$ and $(k) = \pi, \sigma$. The photon density $p_0^{(k)}$ and $p_{N_t}^{(k)}$ at times $-\frac{T}{2}$ and $\frac{T}{2}$ is calculated assuming that the photon density of the pulse is zero outside the interval $\left\langle -\frac{T}{2}, \frac{T}{2}\right\rangle$. The operator $\mathrm{NI}_{m=1}^{M}\left[y_m, x_m\right]$ denotes numerical integration of function $y(x)$ sampled at points $x_m$, $m = 1, 2, ..., M$, with values $y_m$.

Due to the simplifying assumption that the emission cross section $\sigma_i$ can be assumed constant over the interval $\langle t_{i-1}, t_i\rangle$, the values of the cubic approximations $s_i(1)$ and $s_{i+1}(0)$ after propagation through the gain medium at time $t_i$ are in general not equal to each other. The equations above account for the difference by taking the average value. This difference decreases with increasing sampling of the photon densities, and it is proportional to the first derivative of the emission cross section with respect to frequency.

### 5.3.3 Numerical model of narrow-bandwidth pump pulse absorption

To capture both pumping of the gain medium and amplification of the seed pulse, both processes have to be assumed. In most laser CPA amplifiers, energy is first stored in the gain medium by pumping with a pulsed pump laser, laser diodes, or flash lamps. The pumping creates population inversion in the gain medium and the seed pulse then extracts a portion of the energy in one or more amplification passes.

Assuming that the total density of active ions in the gain medium is $N_{tot}$ and that the non-radiating transitions described by the relaxation times $T_{21}$, $T_{32}$ and $T_{10}$ are fast ($T_{21} \rightarrow 0$, $T_{32} \rightarrow 0$ and $T_{10} \rightarrow 0$), the population inversion densities for absorption $\Delta^{(a)}$ and emission $\Delta^{(g)}$ are related by the equation

$$\Delta^{(g)} - \gamma\Delta^{(a)} = N_{tot} \tag{5.28}$$

If the population inversion density is $\Delta_0^{(g)}(z)$ before the arrival of the pump pulse, the initial absorption inversion density $\Delta_0^{(a)}(z)$ can be calculated as

$$\Delta_0^{(a)}(z) = \frac{1}{\gamma}\left(\Delta_0^{(g)}(z) - N_{tot}\right) \tag{5.29}$$

Under the similar assumptions as for the broad-bandwidth pulse amplification, the following numerical model describes the absorption of the pump pulse

$$\Delta_{ij}^{(a)} = \frac{\Delta_{(i-1)j}^{(a)}\left[1-(f_i^{\pi}-1)(f_i^{\sigma}-1)A_{(i-1)j}^{\pi}A_{(i-1)j}^{\sigma}\right]}{\left[(f_i^{\pi}-1)A_{(i-1)j}^{\pi}+1\right]\left[(f_i^{\sigma}-1)A_{(i-1)j}^{\sigma}+1\right]} \tag{5.30a}$$

$$\Delta_{ij}^{(g)} = N_{tot} + \gamma\Delta_{ij}^{(a)} \tag{5.30b}$$

$$p_i^{(k)} = \frac{s_{(i+1)N_z}^{(k)}(0) + s_{iN_z}^{(k)}(1)}{2} \tag{5.30c}$$

$$s_{(i+1)N_z}^{(k)}(0) = \frac{p_{0i}^{(k)}}{1-\left[1-1/A_{iN_z}^{(k)}\right]} \tag{5.30d}$$

$$s_{iN_z}^{(k)}(1) = \frac{p_{0i}^{(k)}}{1-\left[1-1/A_{(i-1)N_z}^{(k)}\right]\left[f_i^{\pi}f_i^{\sigma}\right]^{-1}} \tag{5.30e}$$

$$A_{ij}^{(k)} = \exp\left[\sigma_A^{(k)}D_{ij}\right] \tag{5.30f}$$

$$f_i^{(k)} = \exp\left[c\sigma_A^{(k)}\mathcal{S}_{0i}^{(k)}\Delta t_i\right] \tag{5.30g}$$

$$D_{ij} = \mathrm{NI}_{m=1}^{j}\left[\Delta_{im}^{(a)}, z_m\right] \tag{5.30h}$$

$$p_0^{(k)} = \frac{s_{1N_z}^{(k)}(0)}{2} \tag{5.30i}$$

$$p_{N_t}^{(k)} = \frac{s_{N_tN_z}^{(k)}(1)}{2} \tag{5.30j}$$

Note that the absorption cross section $\sigma_A^{(k)}$ is assumed independent of wavelength since the pump pulse is assumed to have narrow bandwidth.

## 5.4 Numerical calculation of B-integral

The origin of the self-phase modulation was described in the section 2.5.1. For the calculation of the contrast degradation due to birefringence of the gain medium, it can be assumed that the electric field intensity of the main pulse is mostly coupled to one eigenwave of the gain medium, and the impact of cross-phase modulation is therefore negligible.

For passive optical components, the intensity can be assumed constant along the propagation distance $z$ through the medium, and the equation (2.47) for nonlinearity-induced spectral phase due to SPM (also called B-integral and denoted $B$) simplifies to

$$\phi_{\mathrm{NL}}(t) = \frac{\omega}{c}n_2 I(t)L \tag{5.31}$$

Since the intensity of the stretched pulse in approximation of linear chirp is given by equation (2.29), the last equation can be written as

$$\phi_{\mathrm{NL}}(\Omega) = \frac{\beta \varepsilon_0 n_2 L(\omega_0 + \Omega)}{2\pi} S_0(\Omega) \tag{5.32}$$

The last two equations are equivalent due to the time-frequency correspondence (2.26). In the numerical implementation of the model, the nonlinear phase is calculated from the temporal intensity, since the sampling ensures it can be directly applied to the spectrum. The nonlinear spectral phase at time $t_i$ and frequency $\omega_i = \Omega_i + \omega_0$ is

$$\phi_{\mathrm{NL},i} = \frac{1}{2}\omega_i n_2 \varepsilon_0 L \left|E_i\right|^2 \tag{5.33}$$

In case of the gain medium, the intensity evolves during the propagation due to amplification. The intensity $I(z,t)$ can be written in terms of photon density as

$$I(z,t) = c\hbar\omega p(z,t) \tag{5.34}$$

Utilizing equations 5.27, the B-integral from amplification in a gain medium can be written as

$$B_i^{(k)} = \phi_{\mathrm{NL},i}^{(k)} = \frac{1}{2}\hbar\omega_i^2 n_2 \mathrm{NI}_{j=1}^{N_z}\left[s_{(i+1)j}^{(k)}(0) + s_{ij}^{(k)}(1), z_j\right] \tag{5.35}$$

The index $(k) = \pi, \sigma$ denotes the polarization component in anisotropic gain medium. Due to the large number of samples ($r \approx 2^{20}$), the calculation of the amplification using the numerical model (5.27) is time consuming. The calculation speed can be increased by sampling the photon density $p(t)$ of the pulse with a significantly lower number of samples (typically, $N = 2^{10}$ is sufficient). The approach to decreasing the sampling of the photon density is shown in figure 5.5. The red curve illustrates the densely-sampled photon density calculated from the electric field intensity. The sampling is reduced and the average of the surrounding values is taken, since the photon density can become modulated due to presence of satellite pulses with significant delay and relative intensity with respect to the main pulse. The averaging interval is shown in green color in figure 5.5, and it can be adjusted for modeling of specific systems.

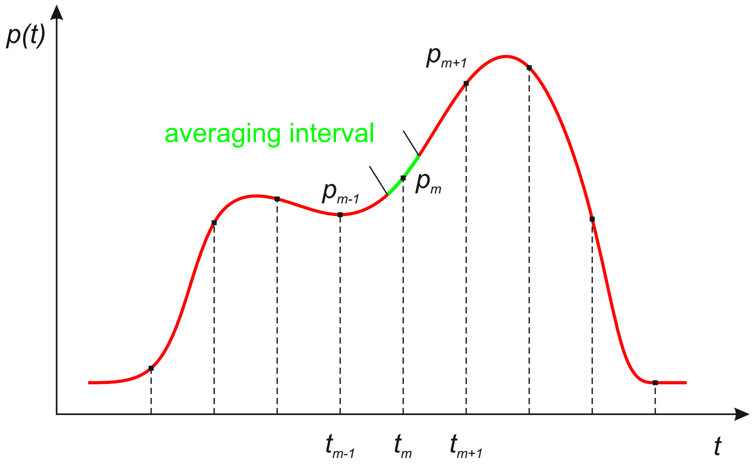

**Figure 5.5:** Down-sampling of the photon density for calculation of pulse amplification and nonlinearity-induced spectral phase.

The calculation of the pulse amplification is then performed on the low-resolution photon density. In order to calculate the amplified pulse and the B-integral with the original resolution, the time-dependent gain is first calculated from the low-resolution input and output photon density $p_{0m}^{(k)}$ and $p_m^{(k)}$ as

$$G_m^{(k)} = \frac{p_m^{(k)}}{p_{0m}^{(k)}}, \text{ for } m = 1, 2, ..., N \tag{5.36}$$

The original resolution of the gain is then restored by spline interpolation, which approximates the values between the low resolution samples. This approximation can be performed since the amplifier gain depends on the population inversion and emission cross section, which both exhibit slow variations with time. The number of low resolution samples $N$ is selected to ensure that the saturation of the gain medium between the samples is small. The evolution of the sub-pulse intensity within the thickness of the gain medium is approximated with small signal gain equation

$$I(z) = I(0)G_{\text{eff}} = I(0)e^{g_{\text{eff}}L} \tag{5.37}$$

where the effective gain is the gain defined by the ratio of the output and input photon density. The high-resolution gain is used to calculate the amplified pulse electric field intensity and the B-integral

$$E_i^{(k)} = \sqrt{G_i^{(k)}}E_{0i}^{(k)} \tag{5.38a}$$

$$\phi_{\text{NL},i}^{(k)} = \frac{1}{2}\omega_i n_2 \varepsilon_0 \left|E_i^{(k)}\right|^2 \frac{\left(G_i^{(k)} - 1\right)L}{G_i^{(k)} \ln G_i^{(k)}} \tag{5.38b}$$

where $E_{0i}^{(k)}$ and $E_i^{(k)}$ are the sampled electric field intensity in polarization component $(k) = \pi, \sigma$ at the input and output of the gain medium, respectively.

The comparison of the B-integral calculated directly in the low resolution pulse amplification (equation (5.35)) and from the high resolution effective gain with the small signal intensity dependence approximation (equation (5.38b)) is shown in figure 5.6. The two calculations yield almost identical results.

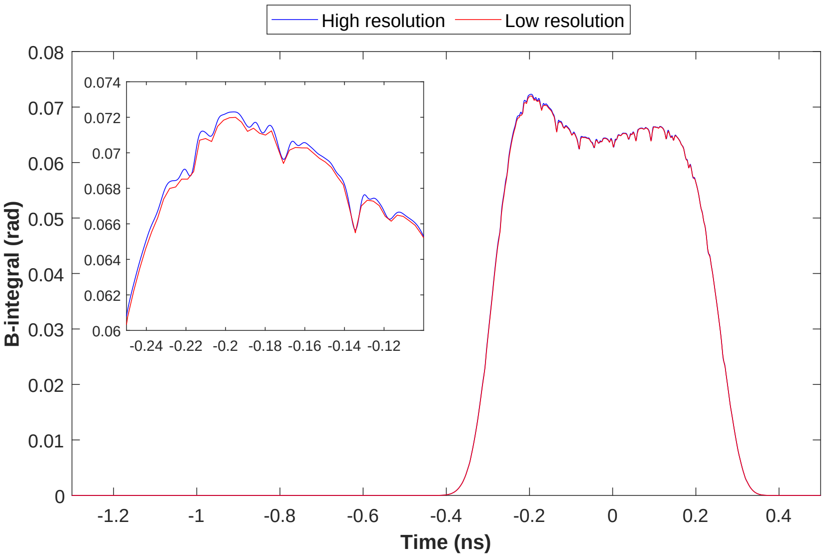

**Figure 5.6:** Comparison between the low and high resolution calculation of B-integral in gain medium.

## 5.5 Implementation of individual optical components

The components evaluated by the numerical model are implemented according to the schematic shown in figure 5.7. The common element for all the components is the application of beam magnification from the location of the last component to the currently evaluated component. The beam magnification factor accounts for the change in beam intensity, which impacts the accumulated B-integral.

The most simple component for implementation is a transparent window. Once the electric field intensity vectors are scaled by the beam magnification, the nonlinear phase is calculated using the equation (5.33), and applied to the polarization components in spectral domain. The impact of cross-phase modulation is not assumed since it is expected to produce pre-pulses with relative intensity contrast significantly lower than self-phase modulation.

Birefringent media, Pockel's cells, waveplates, polarizers, and the compressor all have in common that the decomposition into eigenwaves (or to s and p polarization on the compressor gratings) is calculated after the application of magnification. The calculation of the decomposition is equivalent to the application of rotation matrix to the electric field intensity vector components. The angle $\theta$ is the angle between the direction of the polarization of the main pulse in the previous component with eigenwaves and the current component. The nonlinear phase is then calculated and applied similarly to the case of the transparent window. Delay from propagation and phase retardation are applied in accordance with the type of the medium. For the compressor, the spectral phase is calculated from the dispersion orders and applied to the s and p polarization components.

The highest complexity of the calculation is with the birefringent gain medium. After applying magnification and decomposition to eigenwaves propagating through the gain medium, the amplification of the pulse and resulting nonlinear phase are calculated in accordance with sections 5.3.2 and 5.4. Similarly to the passive birefringent medium, the calculated nonlinear phase and group delay are applied to the electric field intensity components.

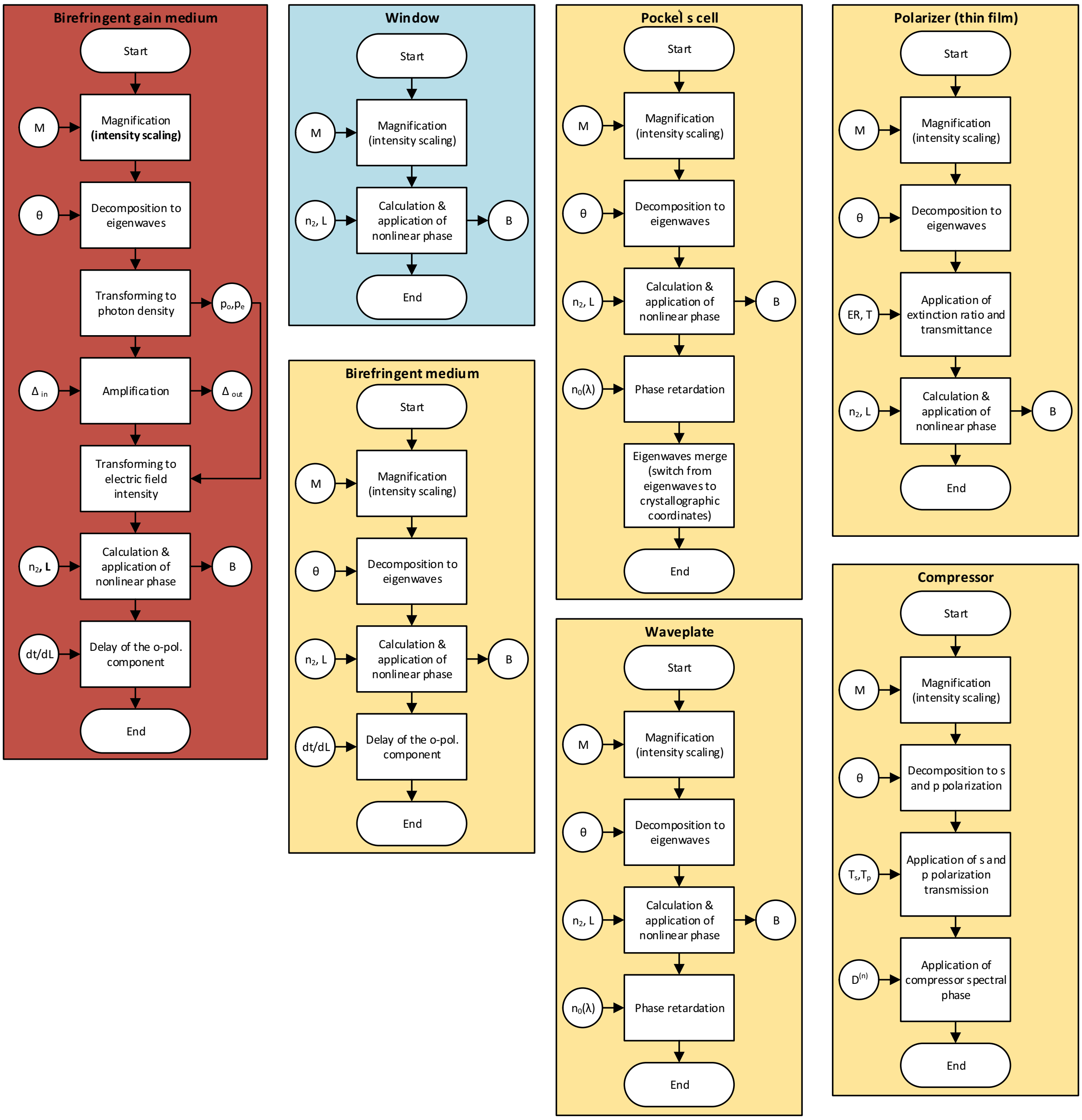

**Figure 5.7:** Diagram of pulse propagation through various types of optical components implemented in the numerical model of pre-pulse contrast degradation.

## 5.6 Validation of the numerical model

The implementation of the numerical model described in this chapter was compared against the performance of the power amplifiers of the L3-HAPLS laser system. The first part of the validation ensures that the model of pulse amplification provides reasonable results, since the B-integral that consequently impacts generation of pre-pulses depends on pulse energy. The model of pulse amplification in the Alpha and Beta amplifier is shown schematically in figure 5.8.

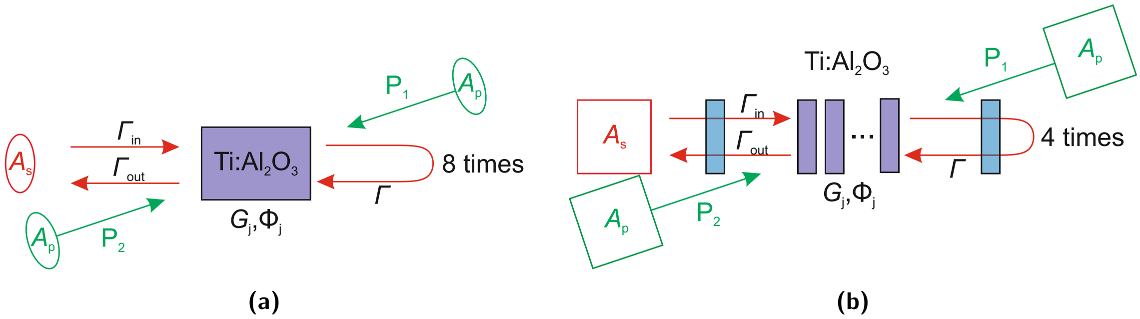

**Figure 5.8:** Schematic diagram of the numerical model of power amplifiers in the L3-HAPLS laser system: (a) Alpha amplifier, (b) Beta amplifier.

The population inversion in the medium is calculated using the model of pump pulse absorption described in section 5.3.3. Pumping by two pulses $P_1$ and $P_2$, one from each side of the gain medium, is assumed. The amplification of the seed pulse is then calcuated for each pass through the amplifier. The loss $\Gamma_{in}$, $\Gamma_{out}$ at the input and output of the amplifier, and the loss $\Gamma$ between amplification passes are applied. The loss factors account for the reflectivity of the HR coatings on mirrors and AR coatings on transmissive optics in the beam path. The input and output loss factor accounts for the loss between the gain medium and the locations of measurement of the input and output energy in the laser system. For both amplifiers, a flat-top beam intensity distribution is assumed in the gain medium.

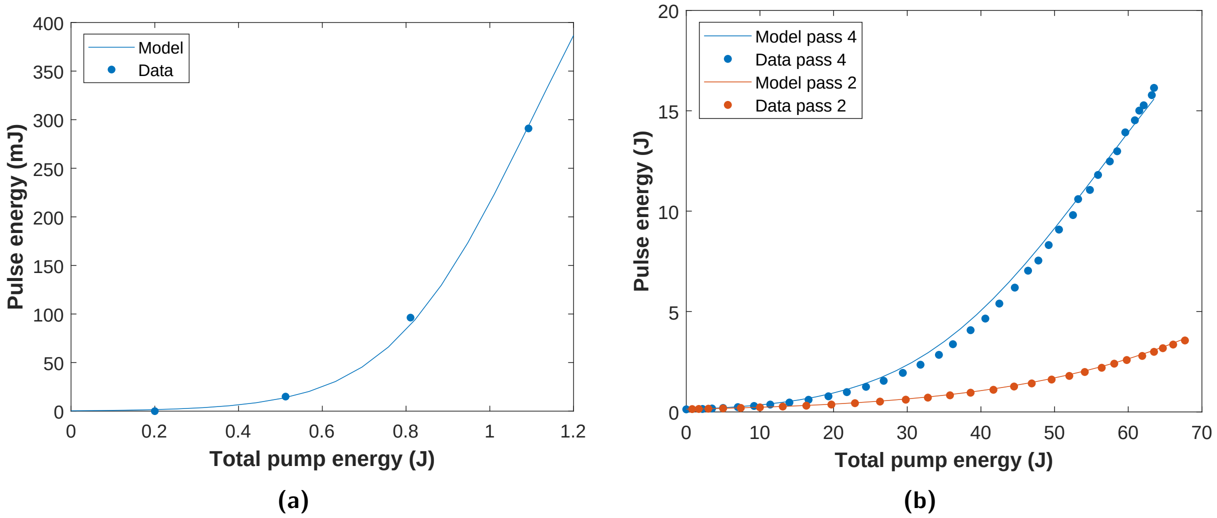

**Figure 5.9:** Comparison of measured and calculated energy characteristics of the L3-HAPLS power amplifiers: (a) Alpha amplifier, (b) Beta amplifier.

The model of the amplifiers uses measured data such as the seed spectrum shape which compensates for square pulse distortion in the amplifiers, splitting ratio of the pump laser energy into the two pump beams, loss factor in the Beta amplifier, etc. These parameters are fixed. The parameter which is adjusted to benchmark the amplification model to the measured data is the density of the active ions in the gain medium of each amplifier. The comparison of the measured and calculated energy dependence of the Alpha and Beta amplifier is shown in figure 5.9. The benchmarking of the model to measured data shows good agreement between the calculated an measured energy characteristics. For the Beta amplifier, the energy after two and four passes through the amplifier were compared with the model, showing that the model represents correctly the pulse energy throughout the amplification process.

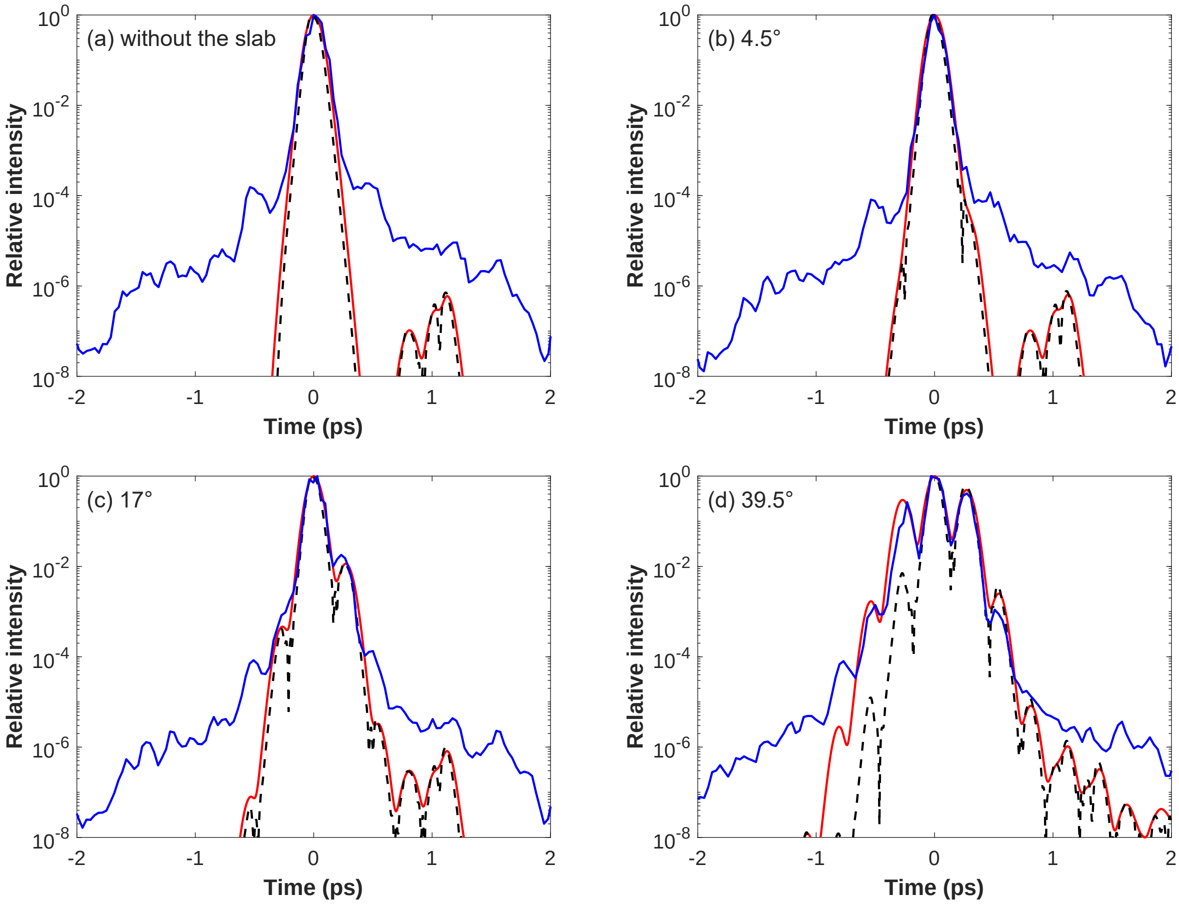

**Figure 5.10:** Comparison of the measured (blue) and calculated (red) cross-correlation trace and calculated intensity contrast (dashed) of the L3-HAPLS laser without the additional slab (a), and with the 10.3 mm Ti:sapphire slab inserted in the system and rotated by 4.5° (b), 17° (c), and 39.5° (d).

In the second part of the validation, an experiment was performed with inserting an a-cut Ti:sapphire slab into the beam path before the Alpha amplifier. The beam was propagating through the slab at normal incidence. The slab was held in a mount allowing for rotation around the axis of the propagating beam. A post pulse was introduced into the amplifier system with relative intensity corresponding to the angle between the input pulse polarization and c-axis of the slab. The thickness of the slab was 10.3 mm, and the expected post-pulse delay calculated from equation (3.31c) was

288.4 fs. The pre-pulse contrast was measured by third order cross correlator (Sequoia, Amplitude technologies) for different angles of the slab rotation. The amplifier system including the additional slab was modelled using the numerical model, and the resulting intensity contrast and third order cross correlator trace were calculated for the slab rotation angles corresponding to the measurements. The resulting comparison of the measured and calculated contrast is shown in figure 5.10.

The spectrum of the amplified stretched pulse at the output of the Beta amplifier was measured for the different rotation angles of the slab. The measured spectra are shown in figure 5.11. The peak at the wavelength of 808 nm is from a CW laser diode illuminating the Beta amplifier head for on-shot damage detection. The red curve shows the spectrum without the additional slab before the Alpha amplifier. The green and blue curves were measured with the slab inserted at an angle of 17° and 39.5°. The measured spectrum was analyzed using Fourier frequency analysis to obtain amplitude and delay of the post-pulse. The result is shown in figure 5.11b. The measured delay is 284.14 fs, and the relative intensity of the post-pulse is $2.3{\cdot}10^{-2}$ and $5.3{\cdot}10^{-1}$ for the slab angles 17° and 39.5°, respectively. Both the delay and the relative intensity of the post-pulse agree with the expected delay calculated from the slab thickness and with the post-pulse intensities measured by the Sequoia.

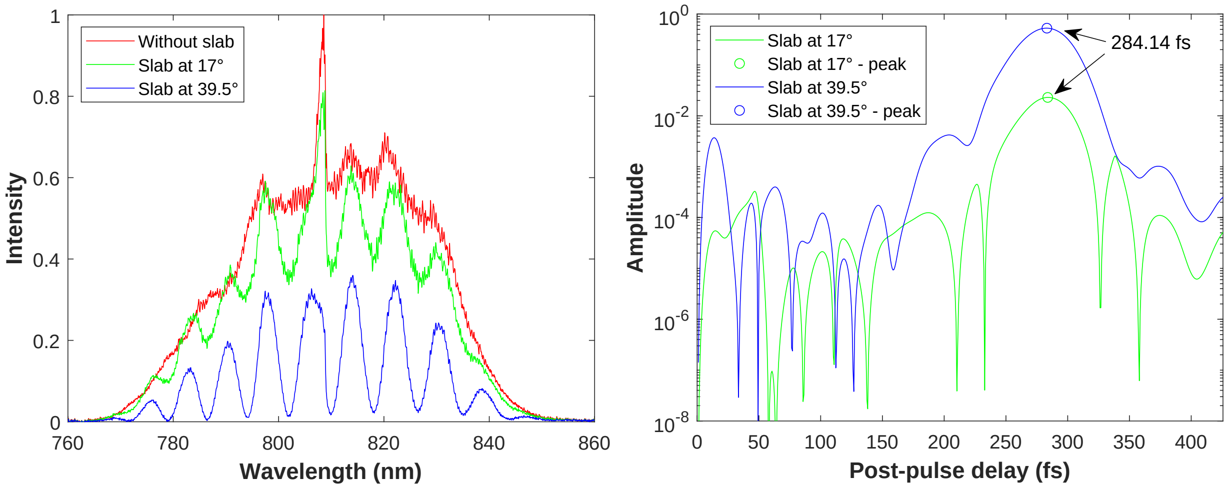

(a) (b)

**Figure 5.11:** Analysis of measured modulated spectra of chirped pulse with post-pulse introduced by Ti:sapphire slab located before Alpha amplifier: (a) measured spectra for different slab angles and without the slab, (b) Fourier analysis of the corresponding post-pulse delay.

## 5.7 Results of the numerical calculations

This section presents the discussion of the impact of the CPA amplifier gain medium birefringence and imperfections of alignment of polarization sensitive components on the final contrast of a petawatt-class CPA amplifier system. The amplifiers discussed here are based on the design of the L3-HAPLS laser Alpha and Beta power amplifiers. The top level description of the L3-HAPLS laser system is presented in section 1.3. The optical components included in the numerical model of the amplifiers and the beam transport between the amplifiers and the compressor are shown in figure 5.12.

The Alpha amplifier provides amplification of the seed pulse from the commercial front-end from 0.5 mJ to 0.5 J. The amplifier contains a single Ti:sapphire crystal and relay imaging telescopes for multiplexing and imaging of the beam at each of the 8 amplification passes. The amplifier is enclosed

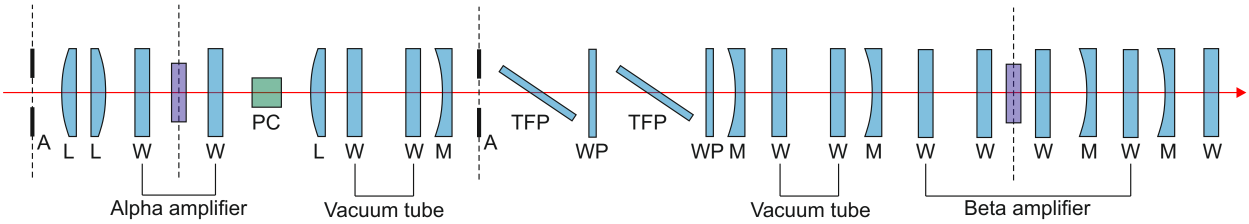

**Figure 5.12:** Optical components included in the numerical model of the power amplifiers of the L3-HAPLS laser system.

in a vacuum chamber to prevent ionization of air and nonlinear optical effects in the focal planes of the imaging telescopes. Energy is stored in the Ti:sapphire crystal by two pump beams, one from each end of the crystal along the propagation direction of the seed pulse. The injection seeded master oscillator power amplifier (MOPA) laser used for the pumping (Northrop Grumman, CPL-020-QSG-0010) is pulsed and generates 10 ns pulses with energy up to 2 J at the wavelength of 532 nm and repetition rate of 10 Hz. The output beam from the pump laser is split into two beams providing the pumping from each side of the amplifier crystal. The pump pulses arrive to the Ti:sapphire crystal just before the seed pulse in order to minimize gain relaxation and ASE. The seed pulse enters the vacuum chamber of the amplifier through a fused silica window and propagates through the gain medium 8 times. After the amplification, the pulse exits the chamber through the same window. The polarization of the pulse on the first pass through the amplifier crystal is set by a $\lambda/2$ waveplate. Between the amplification passes, the polarization is rotated by the amounts shown in figure 3.13. The average values of the polarization rotation between the individual passes were assumed. The amplified pulse passes through a Pockel's cell allowing to select the repetition rate of the pulses seeding the Beta amplifier. Figure 5.8a shows schematically the propagation of the seed pulse through the amplifier. On each pass through the amplifier, gain $G$ and nonlinear phase $\phi$ are calculated and applied to the pulse.

The Beta amplifier is designed to increase the energy of the output pulses from the Alpha amplifier to 40 J. The geometry of the amplifier is similar to the Alpha amplifier. Due to higher thermal load in the gain medium, the amplifier contains several Ti:sapphire slabs rather than a single crystal. The slabs are mounted in a cooling structure allowing circulation of room temperature helium through the amplifier head. The helium flows between the slabs and extracts the stored heat. The amplifier head is separated from the vacuum of the amplifier vacuum chamber by two fused silica windows. Similarly to the Alpha amplifier, the slabs are pumped by two pump beams - one from either side of the amplifier head. The pump laser currently delivers up to 70 J split into two pump pulses with 20 ns pulse duration. The pump pulses arrive to the amplifier head just before the seed pulse. Future upgrade to 1 PW will increase the total pump energy to approximately 140 J, and the amplifier crystals will be pumped by two pulses before the arrival of the seed pulse and by another two pulses during extraction. Figure 5.8b shows the propagation of the seed pulse through the amplifier, as assumed by the numerical model.

### 5.7.1 Ideally aligned system

The contrast was calculated first under the assumption of ideal alignment of the components in the laser system, and without polarization rotation between amplification passes in both Alpha and Beta amplifier. It is expected that only the main pulse should be visible in the resulting intensity contrast background. The result of the calculation is shown in figure 5.13. The post pulse at 4 ps originates in the Pockel's cell and waveplates between the Alpha and Beta amplifier. The voltage of the Pockel's cell is ideally set to half-wave voltage for the center wavelength of the pulse. As was shown in the figure 3.12a, the phase retardation introduced by the DKDP Pockel's cell is equal to $\pi$ only for the center wavelength of the pulse. Due to the spectral dependence of the phase retardation in the Pockel's cell and waveplates, the resulting polarization of the pulse is slightly elliptical for wavelengths other than the center wavelength. The resulting polarization component orthogonal to the polarization of the main pulse is then delayed during the propagation through the Ti:sapphire slabs in the Beta amplifier. Since no component misalignments were assumed, the post pulse does not interact with the main pulse to create pre-pulses. The post-pulse appears in the calculated pre-pulse contrast, since the gratings in the compressor partially reflect the polarization component parallel to the grating grooves.

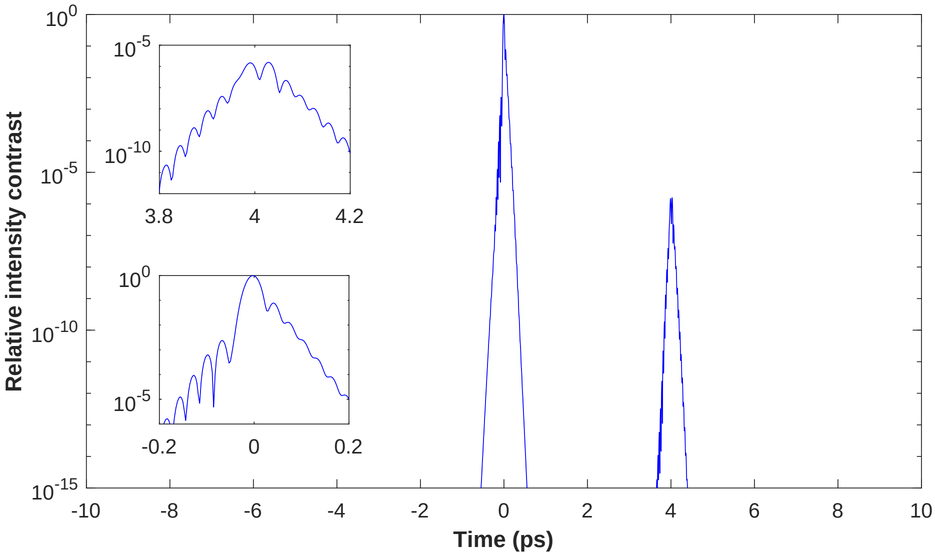

**Figure 5.13:** Calculated ideal relative intensity contrast of the L3-HAPLS laser power amplifiers.

The peak B-integral in the individual components of the amplifiers and in the respective beam paths is shown in figure 5.14. The blue dots show the contribution of the individual components, and the red line shows the cumulative B-integral through the laser system. The individual data points are labeled with the type of the component: W - transparent window, PC - DKDP Pockel's cell, WP - half-wave plate, and Ti:$Al_2O_3$ - titanium sapphire crystal. The most significant nonlinear phase is from the final passes through the amplifier gain media and from the Pockel's cell between the Alpha and Beta amplifier. The relative intensity contrast of the first order pre-pulse depends on the square of the accumulated B-integral, and therefore will be higher the earlier the corresponding post-pulse is introduced into the beam path.

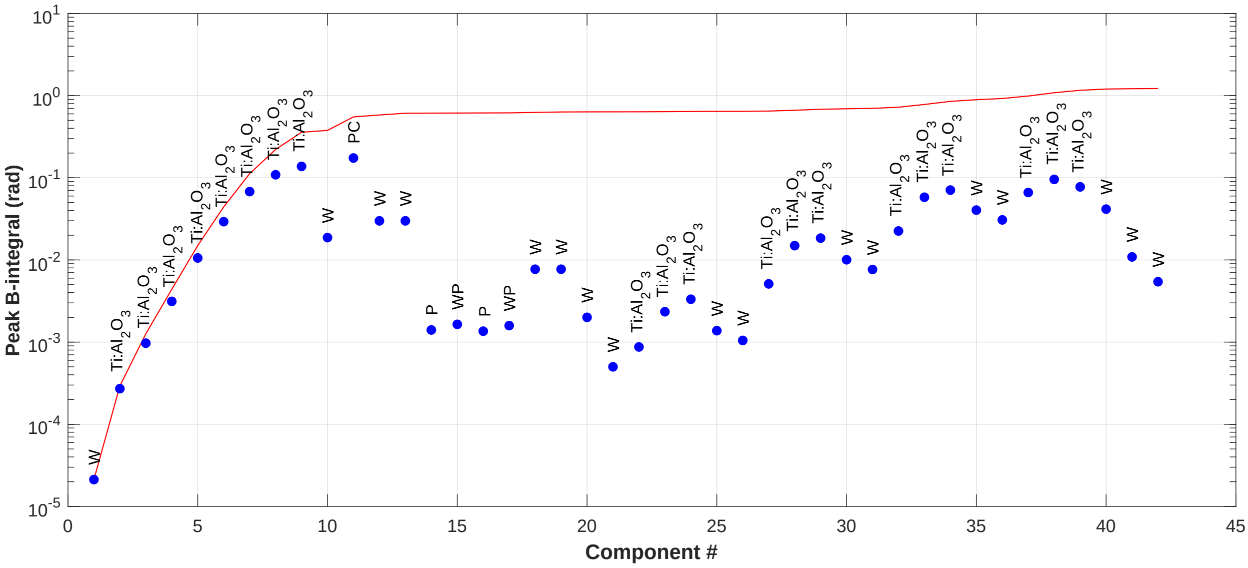

**Figure 5.14:** Calculated peak B-integral in the components of the L3-HAPLS laser power amplifiers. The red line shows the accumulated B-integral.

### 5.7.2 Impact of polarization rotation

The influence of the polarization rotation between amplification passes in the Alpha and Beta amplifier is shown in figures 5.15a and 5.15b. In both cases, the number of pre- and post-pulses present corresponds to the number of amplification passes. The intensity of the pre-pulses is stronger for the plarization rotation in Beta amplifier, since the angle of rotation is larger, and the generation of pre-pulses is impacted by the depolarization in the DKDP Pockel's cell and waveplates. On the other hand, the relative intensity of the pre-pulses is closer to the relative intensity of the corresponding post-pulses for the Alpha amplifier, since the accumulated B-integral is higher.

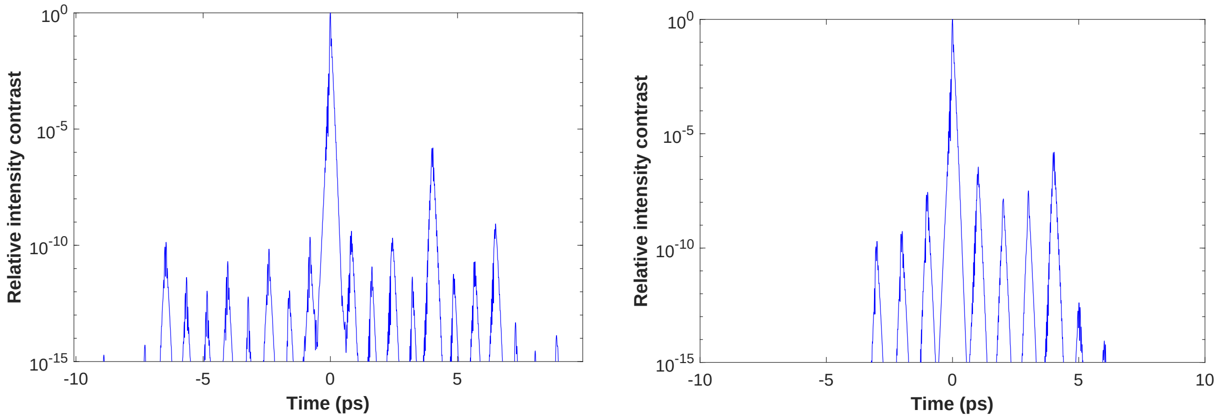

**(a)** **(b)**

**Figure 5.15:** Impact of polarization rotation on the pre-pulse contrast of the L3-HAPLS laser power amplifiers: (a) polarization rotation in Alpha amplifier, (b) polarization rotation in Beta amplifier.

### 5.7.3 Impact of multiple slab misalignment

The amplifier head of the Beta amplifier contains several Ti:sapphire slabs for efficient extraction of the stored heat. The mutual alignment of the slabs is set by their mechanical mounting and by bonding with cladding for absorption of transverse amplified spontaneous emission (TASE). The alignment angle $\theta_i$ associated with each of the slabs is defined as the angle between the c-axis of the crystal and the reference direction for seed pulse polarization with the ideal alignment of the slabs. The mechanical mounting of the slabs is designed to ensure the alignment of each slab is within $\pm 0.3°$ of the designed position. The polarization of the main pulse after passing through $i$-th slab makes an angle $\theta_{i,i+1} = \theta_{i+1} - \theta_i$ with the direction of the c-axis of the following slab. The polarization direction can be therefore misaligned by up to $\pm 0.6°$.
The impact of multiple slab misalignment was evaluated using Monte Carlo simulation. The angles of the amplifier slabs were randomly generated in the range $\pm 1°$, and the contrast of the Beta amplifier was calculated. Figure 5.16a shows the relative intensity of the strongest pre-pulse for each set of slab alignments. The same data set is plotted as a histogram in figure 5.16b. The contrast was calculated with and without the polarization rotation between amplification passes. The polarization rotation was assumed -0.52°, 0.16° and 0.19°, which is the average value across the beam profile. The overall misalignment of the main pulse polarization with respect to the slabs can be characterized by magnitude of misalignment $\psi$ defined as

$$\psi = \frac{1}{\lceil M/2 \rceil} \sum_{m=1}^{\lceil M/2 \rceil} \sqrt{\delta_{2m-1}^2 + \sum_{i=2}^{N} (\theta_i - \theta_{i-1})^2} + \frac{2}{\lfloor M/2 \rfloor} \sum_{m=1}^{\lfloor M/2 \rfloor} \sqrt{\delta_{2m}^2 + \sum_{i=1}^{N-1} (\theta_i - \theta_{i+1})^2} \tag{5.39}$$

where $M$ is the number of amplification passes, and $N$ is the number of slabs. For the first pass, $\delta_m$ gives the sum of the misalignment angles of seed pulse polarization and the first slab. For all other passes, $\delta_m$ is the polarization rotation in the optical beam path between the subsequent amplification passes. In another words, the magnitude of misalignment $\psi$ is the standard norm of the vector consisting of the angles between the polarization of the main pulse and the c-axis of each slab, averaged over all the passes through the amplifier. With this definition, the resulting contrast of the strongest pre-pulse can be approximately calculated as

$$C_{\max}(\psi) = \frac{1}{3} B_0^2 \sin^2 \psi \tan^2 \psi \tag{5.40}$$

where $B_0$ is the sum peak B-integral of the amplifier. Assuming small misalignments, the approximations $\sin x \approx x$ and $\tan x \approx x$ can be used to obtain

$$C_{\max}(\psi) \approx \frac{1}{3} B_0^2 \psi^4 \tag{5.41}$$

As can be seen from the resulting graphs, the pre-pulses due to polarization rotation define the minimum contrast intensity when the slab misalignments are close to zero. In this range, the impact of polarization rotation is dominant over multiple-slab misalignment. The minimum contrast of the amplifier is $2{\cdot}10^{-11}$. This value is lower in comparison with the peak pre-pulse shown in figure 5.15b. The reason is that the degradation calculated by the Monte Carlo simulation assumed only the Beta amplifier without the impact of the preceding optical path. Figure 5.16a shows that the approximate contrast intensity calculated using the equation (5.40) provides a precise estimation of the maximum contrast degradation from the misalignment of multiple amplifier slabs. Figure 5.16c contains the plot of the distribution of the randomly generated misalignments. The dashed black line shows the theoretical distribution corresponding to uniform distribution of individual slab angles on logarithmic scale.

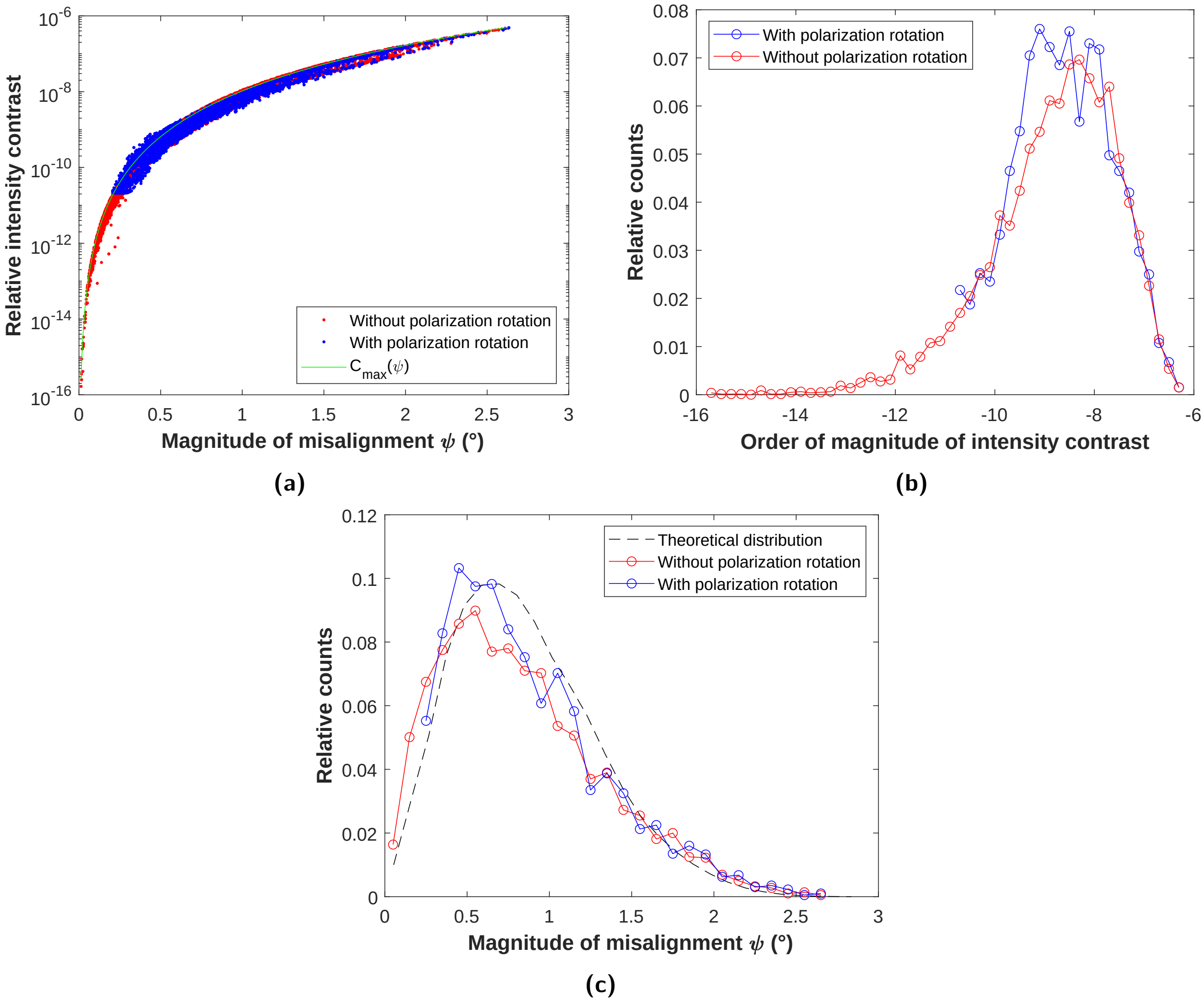

**Figure 5.16:** Impact of multiple-slab misalignment on the pre-pulse contrast of the Beta amplifier with and without polarization rotation betwen amplification passes: (a) dependence of strongest pre-pulse relative contrast on misalignment $\psi$, (b) strongest pre-pulse intensity contrast histogram, (c) distribution of $\psi$ from randomly generated misalignments.

### 5.7.4 Impact of crystal domains

As was shown in chapter 4, the Ti:sapphire crystals can contain domains with different local orientation of the c-axis. This imperfection of crystal growth manifests especially in large aperture crystals. Monte Carlo simulation was performed to evaluate the impact of crystal domain in one of the amplifier slabs. The parameters of the domain were selected based on the results of the measurements presented in section 4.3 - area of the domain covering 5 % of the beam, and c-axis misalignment of 0.7 ° with respect to the rest of the slab. The results of the Monte Carlo simulation are shown in figure 5.17. The presence of the domain impacts the contrast mainly for small misalignments $\psi$. In this range, the relative intensity of the pre-pulses increases by 1-2 orders of magnitude. Figure 5.17a shows that the impact of the c-axis inhomogeneity is lower when the inhomogeneity is located in one of the outer slabs of the amplifier head. The contribution of the inner slabs to the overall misalignment $\psi$ is a factor of two higher than the contribution of the outer slabs. This follows from the equation (5.39) and from the consideration that inner slabs have impact on propagation through two neighbouring slabs, while the outer slabs impact only one. The histogram of the order of magnitude of the strongest pre-pulse contrast shown in figure 5.17b indicates that with the presence of the domain, the intensity contrast with ideal alignment is limited by the pre-pulse intensity from the area of the domain.

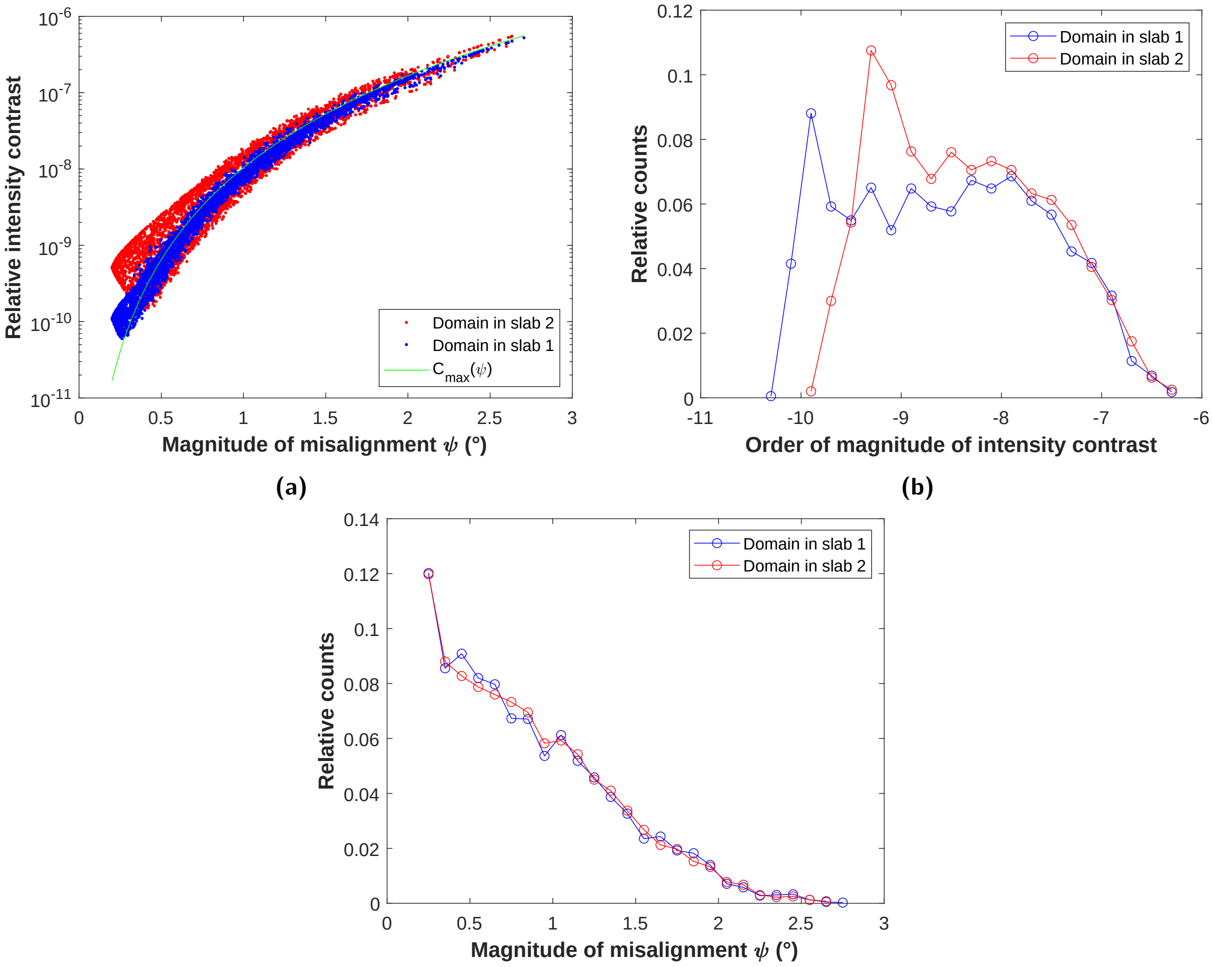

**(a)** **(b)**

**(c)**

**Figure 5.17:** Impact of crystal domain on the pre-pulse contrast of the Beta amplifier with and without polarization rotation betwen amplification passes: (a) dependence of strongest pre-pulse relative contrast on misalignment $\psi$, (b) strongest pre-pulse intensity contrast histogram, (c) distribution of $\psi$ from randomly generated misalignments.

## 5.8 Impact of gain medium birefringence on pre-pulse contrast of regenerative amplifiers

The geometry of the amplifier and the parameters of the gain medium determine the impact of the post-pulses from birefringence on the pre-pulse contrast performance. Regenerative pre-amplifiers, operating with focused beams, typically use Brewster-cut crystals to minimize the impact of normal incidence multiple reflections, and provide additional polarization cleaning. Depolarization of the main pulse increases amplifier loss, and may lead to generation of pre-pulses by direct extraction to the amplifier output. Such pre-pulses occur at nanosecond delays corresponding to the round trip time of the resonator cavity, and can be filtered by a pulse picker.

In regenerative amplifier with birefringent gain medium, the direction of linear polarization with respect to the amplifier crystal depends on precision of alignment of the polarizer and the crystal, and a post-pulse can be introduced. With ideal alignment, the pulse has p polarization upon incidence on the amplifier crystal. At Brewster angle, the reflection is minimal for p polarization. If the alignment is not perfect, the incident pulse has also s polarization component. In case of Ti:sapphire regenerative amplifier, such as e.g. [77], the reflectivity $R$ for the s polarization on the surfaces of the crystal is around 25%. The amplitude of the pulse electric field intensity coupled to ordinary and extraordinary polarization is $\sin\theta$ and $\cos\theta$, respectively. The angle $\theta$ is the angle between the pulse polarization plane and the incidence plane. The ordinary and extraordinary pulse in the Ti:sapphire crystal are amplified by small signal gain $G_\sigma$ and $G_\pi$ in the first passes. The pulse passes through the gain medium two times before passing through the injection polarizer, where part of the post-pulse re-combines with the main pulse. The expected relative intensity of the pre-pulse generated due to B-integral $B_0$ is then

$$C_{-1}(\theta) = \frac{1}{27} B_0^2 \frac{G_\sigma^2}{G_\pi^2} (1-R)^4 \sin^2\theta \tan^2\theta \tag{5.42}$$

This equation assumes intensity distribution given by a $\mathrm{TEM}_{00}$ of the amplifier cavity and a gaussian spectrum of the pulse, hence the factor 1/27. Figure 5.18 shows the calculated relative intensity contrast of the first order pre-pulse from misalignment of the pulse polarization on the Brewster cut crystal in a Ti:sapphire regenerative amplifier. Different curves are plotted for different values of the peak B-integral in the amplifier. The expected misalignment of the crystal in regenerative amplifiers is $<1°$, and the relative intensity of the pre-pulse is expected below $10^{-10}$. The delay of the pre-pulse for a 10 mm thick crystal is around 560 fs, and such pre-pulses are expected to be weaker than the picosecond coherent pedestals.

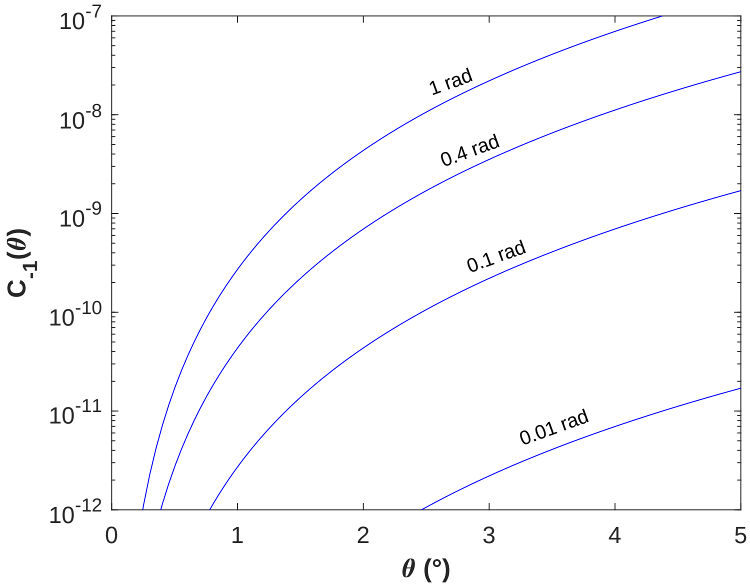

**Figure 5.18:** Relative intensity contrast of first order pre-pulse from birefringence in Ti:sapphire regenerative amplifier.

# Chapter 6

# Improvements of pre-pulse contrast on the L3-HAPLS laser system

From the time of the installation of the L3-HAPLS laser in ELI Beamlines and integration with the petawatt compressor, first commissioning experiments were performed in two of the experimental halls [A2, A3]. The results of the experiments and measurements of the laser contrast indicated the need for mitigation of several pre-pulse contrast defects. This chapter is dedicated to the summary of the measurements and improvements that have been performed to date.

The first commissioning experiments performed with the L3-HAPLS laser identified several pre-pulse contrast defects present in the nanosecond range - see figure 6.1. The experiments performed with the output pulses from the L3-HAPLS laser require pre-pulse contrast better than $10^{-10}$ with the current 0.5 PW performance, and $10^{-11}$ once the output of the laser is increased to 1 PW.

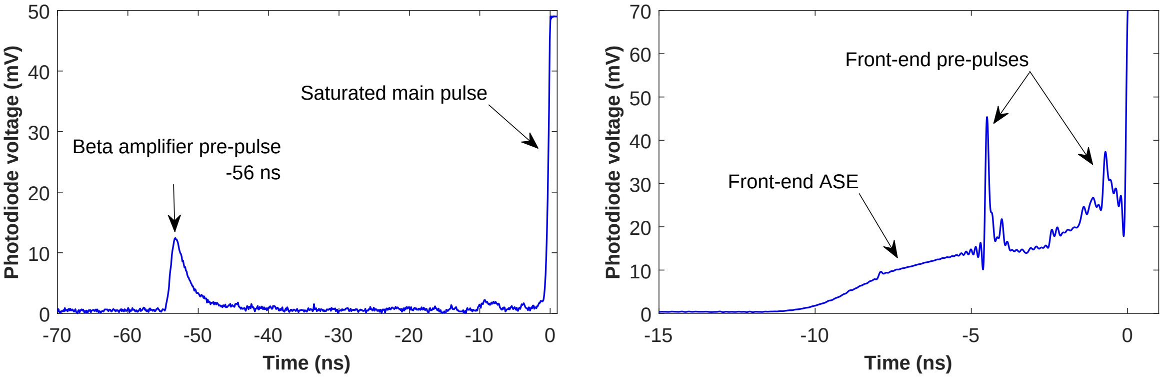

**(a)** Long time scale **(b)** Short time scale

**Figure 6.1:** Photodiode measurements of the initial nanosecond pre-pulses and ASE at the output of the L3-HAPLS laser system: (a) long time scale and (b) short time scale.

A fast photodiode (EOT ET4000, >12.5 GHz bandwidth) and oscilloscope (Keysight DSOS604A, 6 GHz bandwidth) were used for the measurements identifying these pre-pulses in the nanosecond range. First of the contrast defect that was identified was a pre-pulse appearing at 56 ns before the main pulse. The oscilloscope trace from a photodiode measurement identifying this pre-pulse in the focused beam in the E4 experiment is shown in figure 6.1a. The origin of this pre-pulse is in the Beta amplifier, and its source and mitigation are described in detail in section 6.1. On a shorter time scale of ≈10 ns before the main pulse, the photodiode measurement revealed a presence of a rising pedestal overlapping with several pre-pulses. This pedestal and pre-pulses originate in the front-end.

The investigation and the effort to eliminate these pre-pulses and the pedestal are summarized in section 6.2. Compared to picosecond pre-pulses and coherent pedestals, the nanosecond pre-pulses and pedestals have high impact on the laser-matter interaction, since the interaction of pre-pulse light with the target creates pre-plasma that has enough time to significantly expand before the arrival of the main pulse. The main pulse then interacts with a low-density plasma, or the target is completely destroyed before the main pulse arrives. Reduction of such pre-pulses is high priority for opening the experimental capability of the L3-HAPLS laser to the user community.

## 6.1 Mitigation of the pre-pulse originating in the Beta amplifier

The pre-pulse at -56 ns is produced in the Beta amplifier due to an imperfection of the MRF polishing of the Ti:sapphire crystals. The MRF polishing was performed to reduce any transmitted wavefront aberrations originating from crystal lattice aberrations, and maintain excellent focusability of the beam on target [78]. As an unintended by-product of the polishing, the surface of the crystals contains very fine scratches (see figure 6.2) that are primarily oriented in horizontal direction in the final amplifier head assembly. Due to this defect of the MRF polished surfaces, part of the energy of the light passing through the amplifier head is scattered in a wide angle in the plane perpendicular to the direction of the defects.

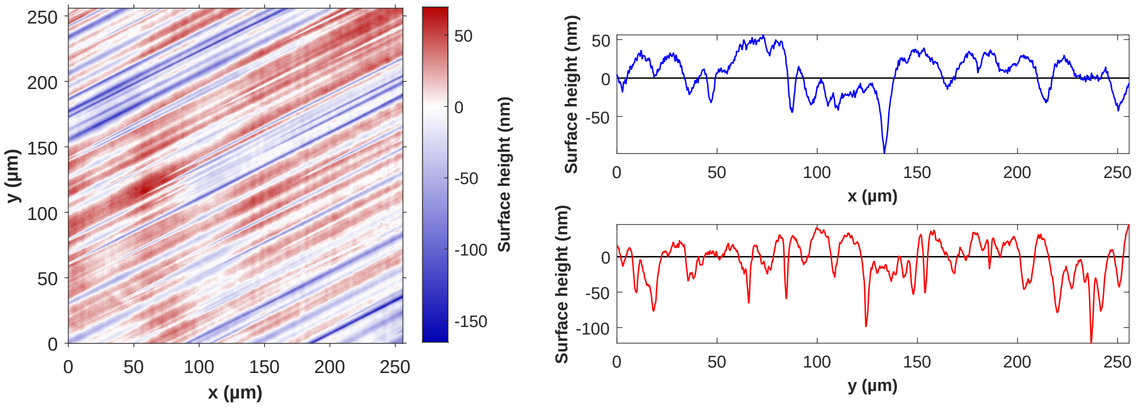

**(a)** **(b)**

**Figure 6.2:** Surface height of the spare Beta amplifier crystal processed with MRF polishing, measured using the Olympus OLS5000-SAF laser scanning confocal microscope. (a) data for 250×250 $\mu$m area, (b) horizontal and vertical profiles at the center of the data set.

The geometry of the multiplexing of amplification passes through the Beta amplifier is shown in figure 6.3. The direction of the scattering coincides with the direction of multiplexing of the four amplification passes. The full relay-imaging of the system ensures that both the amplified pulse and the scattered light are returning to the amplifier head. On each pass through the head, part of the scattered light is therefore coupled into the direction of all the other passes. This cross-coupling leads to the generation of the 56 ns pre-pulse. It also creates a post-pulse delayed by 56 ns, and part of the pulse energy is directed upstream towards the Alpha amplifier and the front-end. The delay of the pre-pulse and post-pulse corresponds to the round trip time of the amplifier, which is 56.4 ns (note that one round trip contains two passes through the amplifier head).

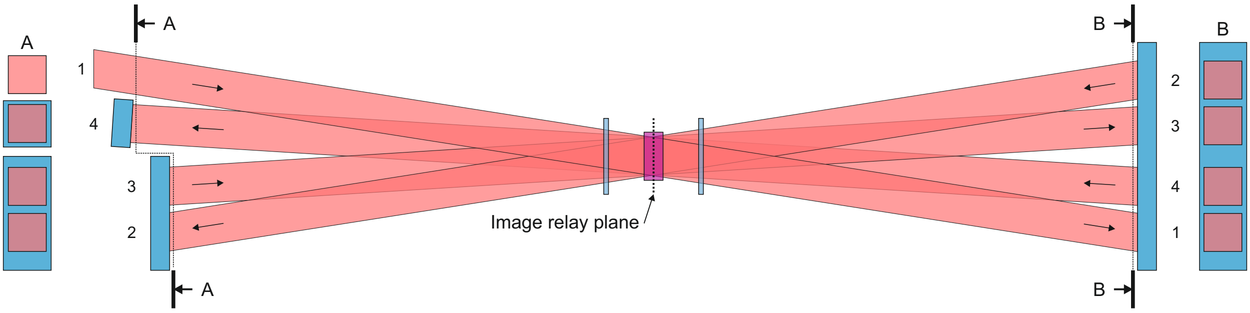

**Figure 6.3:** Schematic diagram showing the geometry of the multiplexing of amplification passes through the Beta amplifier of the L3-HAPLS laser system. The thick black lines with the arrows indicate the direction of the front views on the multiplexing mirrors. The numbers next to the mirrors mark the pass number. The arrows on the beams indicate the propagation direction.

**Table 6.1:** Summary of the amplifier head scatter couplings in the Beta amplifier and their impact on the laser system.

| From pass | To pass | Direction | Results in | Delay (ns)* |
|---|---|---|---|---|
| 1 | 2 | Backward | Back-propagation | 0 |
| 1 | 3 | Forward | Pre-pulse | -56.4 |
| 1 | 4 | Backward | Back-propagation | 112.9 |
| 2 | 1 | Backward | Back-propagation | 0 |
| 2 | 3 | Backward | Back-propagation | 112.9 |
| 2 | 4 | Forward | Pre-pulse | -56.4 |
| 3 | 1 | Forward | Post-pulse | 56.4 |
| 3 | 2 | Backward | Back-propagation | 112.9 |
| 3 | 4 | Backward | Back-propagation | 225.8 |
| 4 | 1 | Backward | Back-propagation | 112.9 |
| 4 | 2 | Forward | Post-pulse | 56.4 |
| 4 | 3 | Backward | Back-propagation | 225.8 |

* The delay is relative to the main pulse for forward direction, and to the first backward propagating pulse from scattering for backward direction.

The full mitigation of the pre-pulse requires replacement of the amplifier crystals, since the main source is the scattering. Temporarily, the problem was solved by adjusting the multiplexing of the amplification passes through the amplifier head. The passes 1 and 4 were set to propagate through the head at a different horizontal angle than the passes 2 and 3. The nominal size of the collimated beam passing through the amplifier head is 50×50 mm. The horizontal size of the multiplexing mirrors is 60 mm, and the HR coating spans all the way to the edges. A horizontal offset of 6 mm was therefore possible, corresponding to an angular offset of 0.24°. This offset ensured that the focal spot of the scattered light coupled from pass 1 to pass 3 and from pass 2 to pass 4 was no longer overlapping with the main spot in the focal plane of the output telescope of the amplifier, and could be filtered by a proper beam stop.

The origin of the pre-pulse allowed for inserting a beam block into the path of the main beam after passing through the amplifier head and producing the scatter. This enabled for studying the intensity distribution of the pre-pulse in the focal plane of the OAP in one of the experimental chambers. The relative intensity of the residual pre-pulse light in focus on target was measured to be on the order of $10^{-10}$ after the horizontal multiplexing angle was introduced.

Apart from for the contrast degradation and backward-propagating light, the scattering on the Beta amplifier head crystal surfaces contributes significantly to the amplifier loss. The percentage of energy loss per amplification pass was calculated from the total passive transmission of the amplifier, which was measured to be 57.85%. Including the AR and HR coatings reflectivity, the total loss per pass is 12.8 %. Subtracting the design reflectivity of the coatings, the loss from scattering is 10.8%. This extra loss is significant. The numerical model of the Beta amplifier, described in chapter 5, was used to evaluate the impact of this loss on the amplifier performance. The calculation of the amplifier output energy without the scattering loss indicates that at the current full performance, the energy of the pulse from the amplifier could be 4-5 J higher.

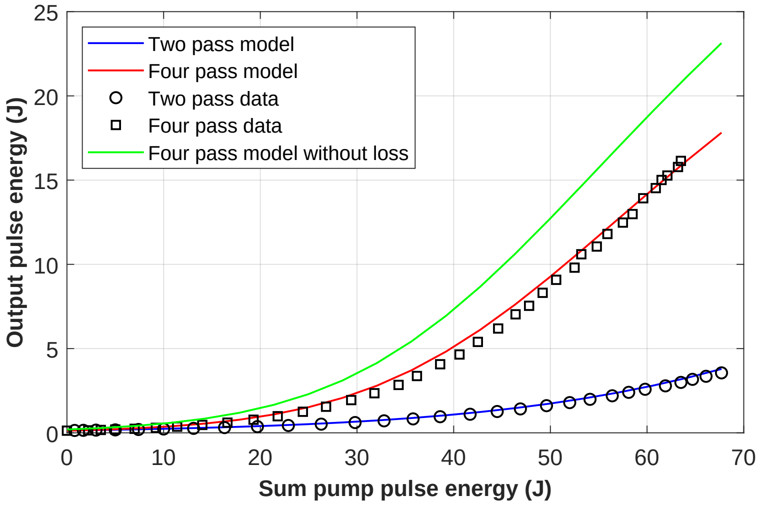

**Figure 6.4:** Impact of the crystal scattering loss on the Beta amplifier performance.

## 6.2 Mitigation of pre-pulses originating in the front-end

The pre-pulses and the rising pedestal in the nanosecond range before the main pulse all originate in the commercial front-end. A block diagram of the front-end is shown in figure 6.5. A Ti:sapphire femtosecond oscillator is used to seed the system. The oscillator operates at 80 MHz repetition rate, and its cavity length is actively stabilized to synchronize the repetition rate with an external electronic oscillator. This stabilization of jitter with respect to the system timing ensures improved temporal stability of the entire laser chain. The pulses from the oscillator are stretched in a high-dispersion bulk glass stretcher prior to amplification. The first stage multi-pass amplifier amplifies the 80 MHz pulse train from the oscillator in the first four amplification passes. The strongest pulse is selected by a pulse picker with two polarizers, and its spectrum and spectral phase is shaped by the first dazzler. The pulse picking reduces the repetition rate to 100 Hz. The selected pulses are then re-injected into the amplifier for additional five passes of amplification. Before the XPW, the pulse is compressed by a combination of a transmissive grating compressor and chirped mirrors. The XPW stage limits ASE and pre-pulses from the first stage amplifier and broadens the pulse spectrum by SPM. After contrast cleaning in the XPW, the pulse is stretched in the main stretcher and amplified in the second stage amplifier. At the input to the second amplifier, the spectrum and spectral phase are shaped by the second dazzler. The amplifiers in the front-end operate at 100 Hz, and both are pumped by a single commercial Q-switched frequency-doubled laser (Photonic Industries).

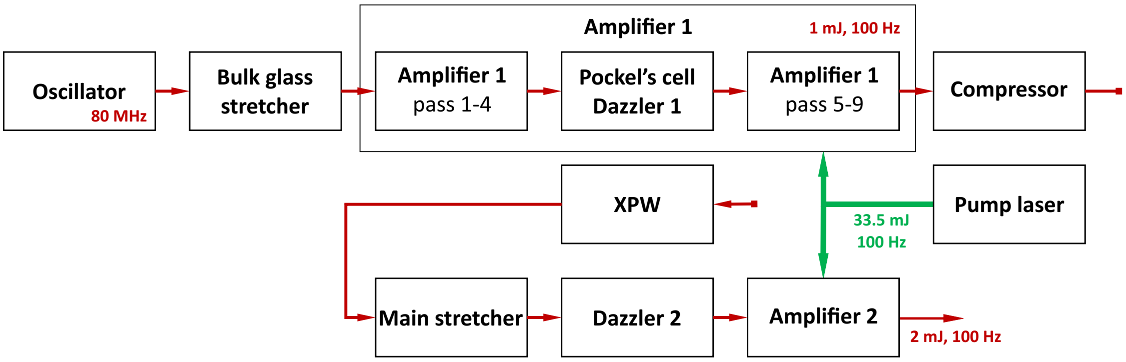

**Figure 6.5:** Block diagram of the L3-HAPLS laser front-end.

### 6.2.1 Improvement of the XPW performance

A typical photodiode trace of the nanosecond background before the output pulse from the first amplifier is shown in figure 6.6. The measurement shows the presence of 80 MHz pre-pulses leaking through the Pockel's cell selecting the strongest pulse from the amplified pulse train. Figure 6.6a shows that the residual pulses from the pulse train can be minimized by the Pockel's cell alignment. Figure 6.6b shows in a closer view the last 80 MHz period before the main pulse. There are clearly visible additional pre-pulses at -9 ns and -4.5 ns, and also an increasing rising edge of the Pockel's cell transition from 0 V to the half-wave voltage. The switching time of the Pockel's cell used is around 3.5 ns.

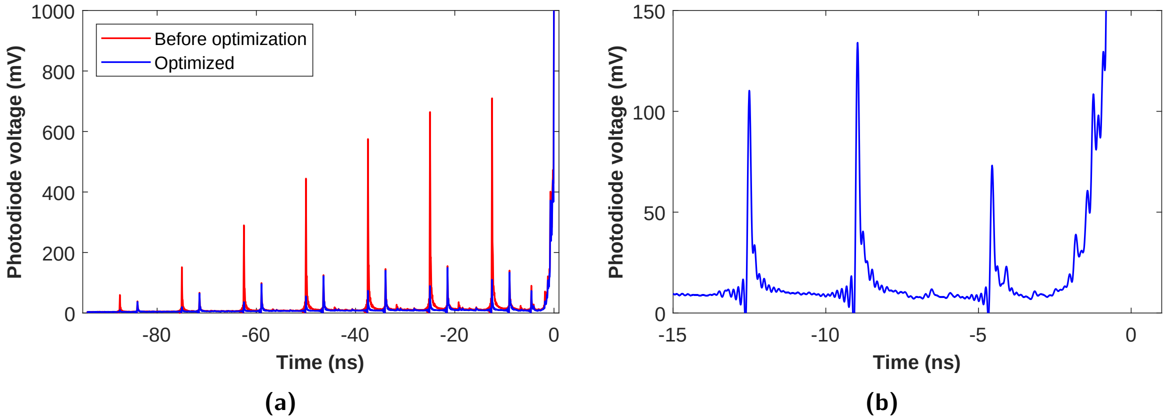

**Figure 6.6:** Photodiode trace of the prepulses in the output beam of the first amplifier in the L3-HAPLS front-end; (a) optimization of extinction of the 80 MHz pulse train by iterative pulse picker alignment, (b) close view within one 80 MHz period.

A comparison of the first amplifier pre-pulse background with the photodiode trace shown in figure 6.1b indicates that the pre-pulses at times less than 5 ns before the main pulse originate in the first amplifier, and are not extincted by the XPW and Pockel's cell between Alpha and Beta amplifiers.

The XPW stage of the front-end contains a $BaF_2$ crystal for the cross-polarized wave generation and spectrum broadening. The beam quality in the $BaF_2$ crystal is improved by propagation through a hollow-core fibre (HCF) in order to maximize the XPW efficiency. The nonlinear crystal and the HCF are located between two crossed polarizers. The achievable contrast improvement by the XPW is given by the extinction ratio of the polarizers for input pre-pulse contrast ratios below $10^{-3}$ [49]. For the thin film polarizers used in the L3-HAPLS front-end, the contrast ratio of >200:1 is declared. The initial performance of the XPW is shown in figure 6.7a, showing an improvement of the contrast between 1 and 2 orders of magnitude.

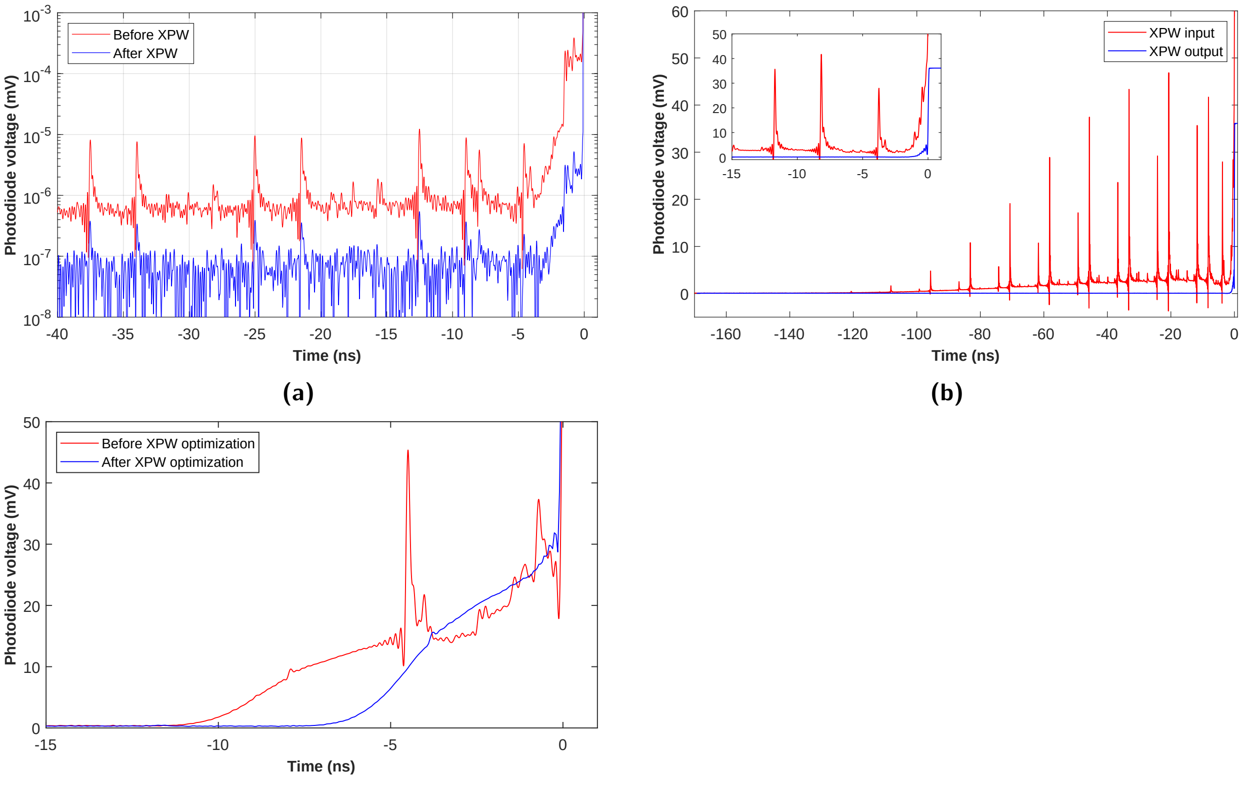

**(a)**

**(b)**

**(c)**

**Figure 6.7:** Nanosecond contrast improvement by the XPW stage; (a) with thin film polarizers, (b) with the output polarizer replaced with Glan-Taylor polarizer, (c) impact of the improvement on the pre-pulse background at the output of the L3-HAPLS laser system.

To increase the XPW performance, the output polarizer was replaced with a Glan-Taylor polarizer (ThorLabs GL15-B) having an extinction ratio declared by the manufacturer as $10^5$:1. The reason for replacing only the output polarizer and not the one at the input is that the intensity in the input beam is large enough for significant SPM, which would adversely impact the required compression of the pulse at the $BaF_2$ crystal. The polarization state of the output of the first amplification stage is well defined due to Brewster angle incidence on the amplifier crystal and on the input windows of the crystal housing. The photodiode trace of the pre-pulse background after the replacement of the output polarizer is shown in figure 6.7b. The measurement shows no measurable pre-pulses in front of the main pulse after the installation of the Glan-Taylor polarizer.

The pre-pulse background at the output of the L3-HAPLS laser system was measured after the improvement of the XPW performance. The comparison of the resulting pre-pulse background with the initial state is shown in figure 6.7c. The difference in the duration of the rising pedestal is a result of optimization of the trigger timing delay for the pulse picker between the Alpha and Beta amplifier. The amplitude of the pedestal is different due to a different alignment of the photodiode between the two measurements. It is clear that the pre-pulses generated in the first amplifier inside the front-end no longer propagate past the output polarizer of the XPW. The remaining contrast problem originating in the front-end is therefore the rising pedestal.

### 6.2.2 Reduction of the rising pedestal

The origin of the rising pedestal shown in figure 6.7c was traced to the second multi-pass amplifier of the front-end. The disadvantage of using a single pump laser for pumping both of the front-end amplifiers is that the pump pulse arrives into the second amplifier much earlier than the seed pulse. There is therefore enough time for ASE build-up. From the moment when energy is stored in the amplifier crystal, ASE starts to be generated. The amplifier contains two metal plate masks with holes to allow through only the individual amplification passes, and block the majority of the ASE from returning into the gain medium. However, the ASE that overlaps with the multiplexing of the amplifier is returned and passes through the gain medium several times. The ASE at the output of the amplifier is the superposition of the ASE emitted into the direction of all the amplification passes. The ASE overlapping with the final pass direction goes directly to the amplifier output. The ASE emitted into the remaining passes goes through the gain medium several times and appears at the amplifier output with a corresponding delay and amplification.

The extent of the ASE before the amplified pulse depends on several factors. Since population inversion needs to be established in the gain medium before the first pass of the seed pulse, the ASE will be present at the amplifier output at minimum during the propagation of the seed pulse through the amplifier. The energy is typically stored into the gain medium during a time interval corresponding to the duration of the pump pulse, leading to presence of amplifier gain already before the arrival of the seed pulse. If the pump pulse arrives too early, the extent of the ASE will be even longer, and the initial gain for the amplification of the seed pulse will be reduced through the ASE. The rate at which the gain is reduced depends on the geometry of the pumped volume in the gain medium, and on the amount of the ASE being returned into the gain medium by the multiplexing optics. Typically, the relaxation of the gain will be shorter than the fluorescence life time in the gain medium, which is 3.2 $\mu$s for Ti:sapphire. The evolution of gain in a multi-pass amplifier with a single pump pulse is shown in figure 6.8.

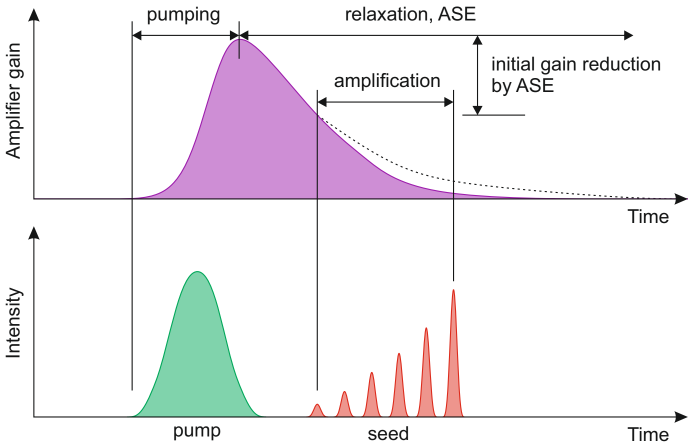

**Figure 6.8:** Evolution of the gain in a multi-pass amplifier, and impact of pumping early pumping of the gain medium.

A typical temporal dependence of the ASE from the second amplifier is shown in the figure 6.9. The graph on the left shows the ASE from an unseeded amplifier, while the graph on the right shows ASE with a low energy seed injected into the amplifier. The rising edge of the ASE pulse corresponds to the duration of the pump pulse, which is specified as 120 ns for the Photonics Industries model DM50 pump laser. The falling edge is significantly shorter than the fluorescence life time of the Ti:sapphire due to the amplification of the spontaneous emission within the length of the gain medium and through multiple passes. The delay of the seed pulse with respect to the peak of the ASE is 76 ns.

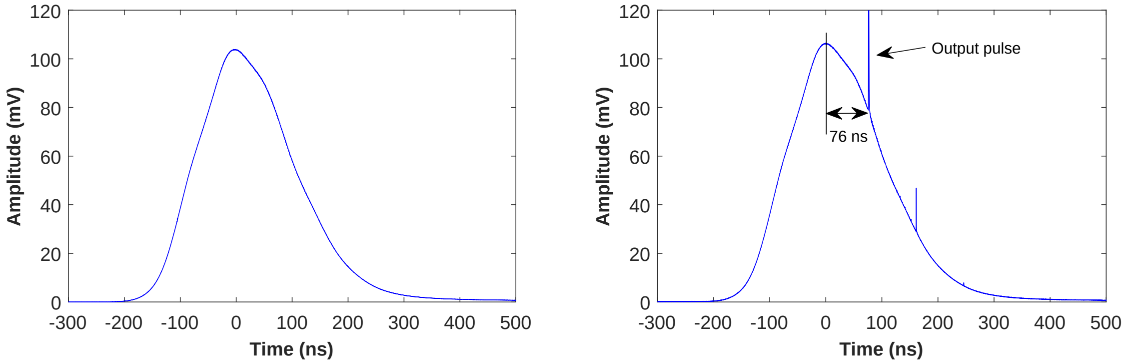

**Figure 6.9:** Typical unseeded (left) and low-energy seed (right) ASE of the L3-HAPLS front-end, measured with a photodiode.

The rising ASE pedestal shown in the figure 6.7c is the front-end ASE which is not suppressed by the pulse picker between the Alpha and Beta amplifier. The Pockel's cell used for the pulse picking has large clear aperture in order to support propagation of the 1 cm diameter beam from the Alpha amplifier. The size of the Pockel's cell limits the achievable rise time to 5-8 ns.

In order to reduce the ASE to an acceptable level for the laser-matter interaction experiments, several steps were performed. The first effort was to install an additional pulse picker with a very fast rise time of 250 ps at the output of the front-end. This pulse picker would allow for reducing the ASE and any pre-pulses in times >250 ps before the main pulse. Unfortunately, the Pockel's cell was damaged during the testing and had to be sent for repair. In the meantime, the performance of the second amplifier stage was investigated with the goal to reduce the intensity of the ASE.

The intensity of the ASE depends on the geometry of the pumped area in the gain medium, on its material properties, and on the gain [79, 80]. Changing the parameters of the gain medium would require reconstructing the amplifier. As was discussed above, the ASE extent cannot be reduced much below the sum of the the pump pulse duration and the time required for the seed pulse to traverse the amplifier. In the case of the L3-HAPLS laser front-end, the strongest pulse selected in the first amplifier travels through the remaining 5 passes of the amplifier, XPW, and stretcher in approximately 100 ns. The pump pulse for the second amplifier therefore arrives into the gain medium approximately 100 ns earlier than would be optimal. During this period, the energy stored in the Ti:sapphire crystal decays, and the initial gain for the first pass of the seed pulse is reduced. It is critical to ensure that this decay is as small as possible, since the rate of the decay drives the amount of extra energy that needs to be stored in the gain medium to achieve the desired energy of the output pulse, and consequently the amount of ASE emitted by the amplifier before the amplification of the seed pulse. To minimize the decay due to ASE, coupling of the ASE was investigated. The strongest impact on the decay and on the intensity of the ASE in the amplifier output has any mechanism returning the ASE overlapping with the amplifier multiplexing and propagating in the oposite direction as the seed pulse. A simple test was performed by simultaneously observing the unseeded ASE beam profile and spectrum at the output of the front-end, and blocking the beam path at the input to the amplifier between different components in the beam path. This test has revealed a coupling of the backward-propagating ASE into forward direction through scattering on an alignment iris aperture. Figure 6.10 illustrates this coupling.

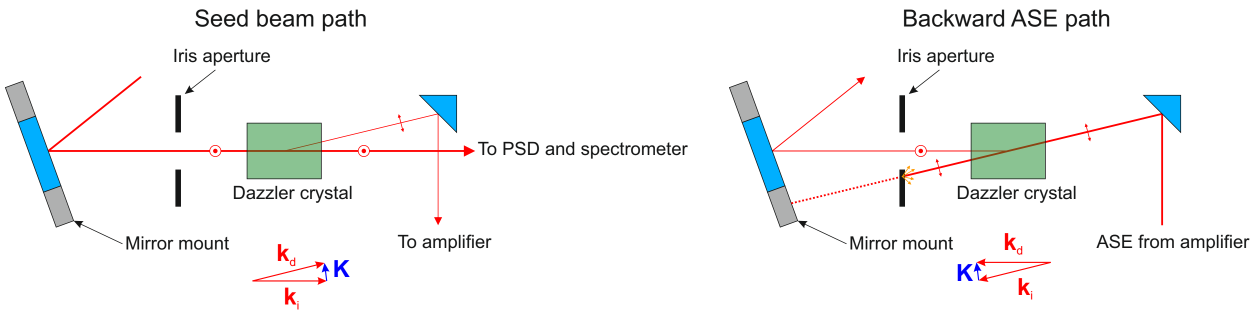

**Figure 6.10:** Coupling of the backward-propagating ASE into forward direction in the L3-HAPLS second front-end amplifier.

The beam path just before injection into the second amplifier contains a dazzler for shaping of the pulse spectrum and optimizing dispersion [72, 73]. The dazzler uses diffraction on a grating induced by an acoustic wave in a birefringent crystal. The diffracted beam propagates at a different angle than the incident beam, and its polarization is perpendicular to the polarization of the incident beam. The diffraction efficiency is driven by the intensity of the acoustic wave, and for the dazzler used in the front-end it is below 10 %. Figure 6.10 also shows the Bragg condition for efficient diffraction. $\mathbf{k}_i$, $\mathbf{k}_d$ and $\mathbf{K}$ denote the wave vectors of the incident, diffracted and acoustic waves. It is clear that any coupling of the diffracted backward ASE is reduced by a square of the diffraction efficiency compared to the coupling from the undiffracted ASE. The undiffracted backward ASE beam was originally terminated on a metal frame of the iris aperture referencing the position of the input beam. The scattering from this metal frame was coupled back into the amplifier and significantly increased the ASE intensity and reduced the amplifier gain. The reference iris was removed and the ASE beam was blocked by an absorbing filter with a low scattering material blocking the reflected and transmitted beam after incidence on the filter.

The impact of mitigation of the ASE coupling is shown in figure 6.11. In both measurements, seed pulse with very low intensity was injected into the amplifier for comparison of the performance. The top two graphs show the photodiode trace in the original configuration, and the bottom graphs show the configuration with ASE coupling removed. There are several differences showing the improvement in amplifier performance without the coupling: the ASE has much lower intensity, the relaxation time is longer, and the signal of the amplified main pulse is significantly stronger. The peak of the ASE appears 100 ns before the main pulse, while with the coupling the ASE was at peak 76 ns before the main pulse. The slower decay and higher energy of the main pulse indicate that the initial gain for the seed pulse is higher since more energy remains stored in the gain medium. The difference in the position of the ASE peak with respect to the pulse matches the time required for the coupled backward ASE to traverse the amplifier, which is approximately 24 ns.

Since the decay of amplifier gain between the pump pulse and arrival of the seed pulse was reduced, the pump pulse energy could be decreased to obtain the same energy of the output pulse. In order to allow for reducing the pump pulse energy (and consequently the ASE intensity) even further, the energy of the seed pulse was increased by increasing the output of the first amplifier and the XPW stage. The dependence of the XPW output pulse energy and efficiency on the energy of the input pulse are shown in figure s 6.12a and 6.12b, respectively. The energy of the first stage amplifier was increased by 10 %, yielding a 15 % increase in the energy at the XPW output. In order to increase

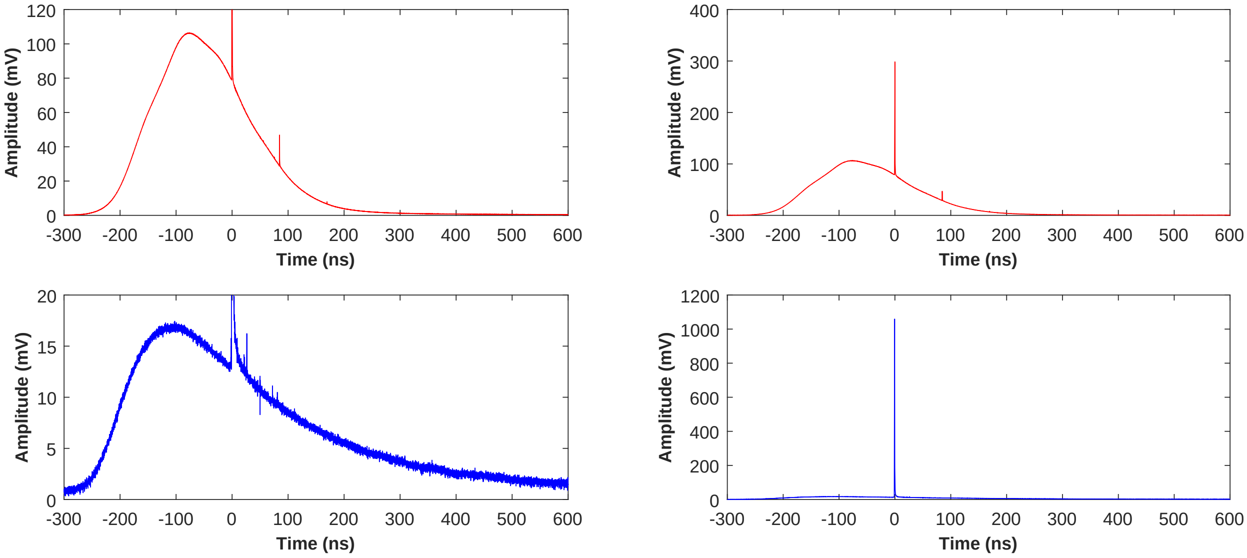

**Figure 6.11:** Impact of the mitigation of the ASE coupling on the output of the second front-end amplifier with low energy seed pulse: (red) with ASE coupling, (blue) without ASE coupling.

the XPW efficiency further, the position of the crystal with respect to the output of the HCF could be adjusted. The overall transmission of the XPW could be increased this way to around 20 % [50]. The disadvantage of this approach is reduced life time of the XPW crystal. This option was therefore left as a backup solution.

The output pulse energy and energy of the unseeded ASE as a function of the pump pulse energy in the second front-end amplifier is shown in figure 6.13. The ASE energy data were fit with an exponential function. The fit of the output pulse energy data is a quadratic fit and serves only for visual guidance. The energy of the pump pulse was set initially to 27 mJ, corresponding to maximum output energy of 3 mJ from the amplifier. With this configuration, the front-end was operated at output energy of 2 mJ set by the amplitude of the RF signal on the dazzler 2. After removing the ASE coupling and increasing the seed pulse energy, the pump pulse was reduced to 23 mJ, which allowed for reducing the ASE by a factor of 5 and maintaining the required performance of the front-end.

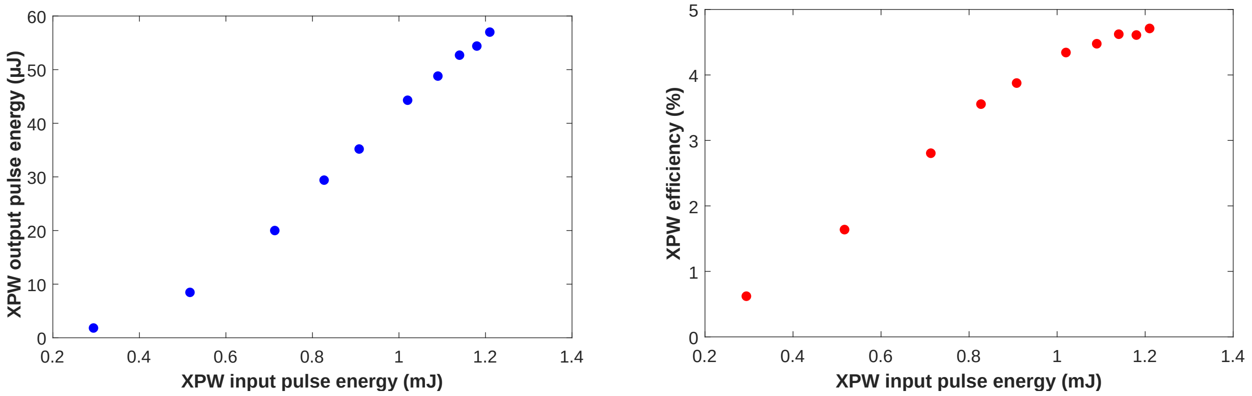

**(a)** **(b)**

**Figure 6.12:** Characteristics of the L3-HAPLS laser front-end XPW stage: (a) output energy vs. input energy, (b) XPW efficiency vs. input energy.

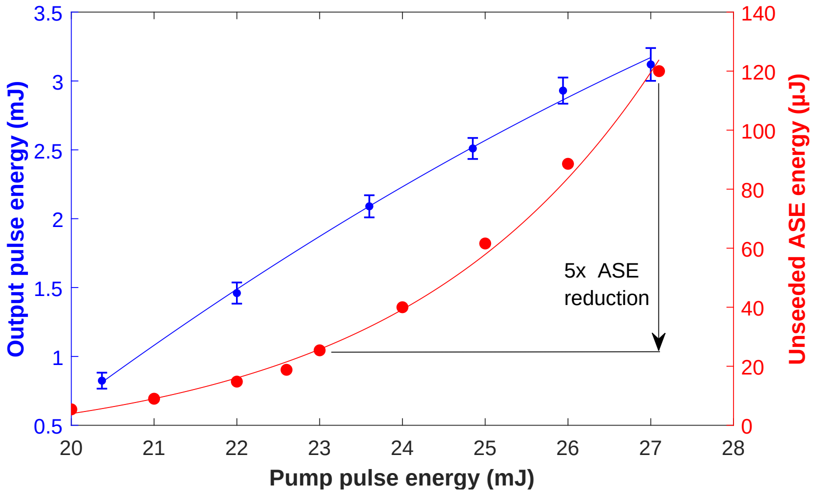

**Figure 6.13:** Pulse energy and unseeded ASE energy at the output of the second front-end amplifier as a function of the pump pulse energy. The data were measured after the ASE coupling was removed.

After the above described contrast improvements were implemented, the performance of the L3-HAPLS system was tested through proton acceleration in the E4 experiment. In the initial configuration, the proton acceleration was limited to 1 MeV proton energy. After the improvements, the achievable energy increased to 18 MeV. While this improvement is significant and allowed for basic commissioning of the proton acceleration experiment, the laser design parameters should allow for acceleration of protons to 30 MeV. An additional reduction of the pre-pulse background was therefore necessary.

### 6.2.3 Installation of a fast pulse picker

As was mentioned in the previous section, the fast Pockel's cell for reducing the front-end pre-pulses was damaged due to low damage threshold of the AR coatings during the initial test. In order to reduce the fluence of the beam in the Pockel's cell location, the output telescope of the front-end, which is reducing the beam size, was replaced with flat mirrors - see figure 6.14. This allowed for increasing the size of the beam to the limit allowed by the 5 mm clear aperture of the Faraday rotators. The Pockel's cell has a clear aperture of 6 mm. The change in the beam size after the isolators was compensated by the focal length of lens L1. The collimation of the beam in the rest of the system was restored by adjusting the distance of the lens L1 from the lens L2.

The configuration of the pulse picker and its location is shown in figure 6.14. The setup with a single polarizer was selected since the polarization at the output of the front-end is well defined due to the Brewster angle incidence on the second front-end amplifier crystal and entrance windows of the amplifier head vacuum chamber. The section of isolators originally contained three Faraday rotators with three thin film polarizers. The first polarizer after the Pockel's cell was replaced by a Glan-Taylor polarizer for better extinction and easier optimization of alignment. The change in material dispersion was compensated by the dispersion of the dazzler 2.

The alignment of the pulse picker was optimized for maximum extinction. The opening window of the Pockel's cell was measured using a photodiode located in the front-end beam transmitted through the pulse picker. The ASE was used as the light source for the measurement. The result is shown in figure 6.15b. The rising and falling edge of the Pockel's cell opening window comprise a fast and a slower transition. Taking into account both the parts, the 10 %-90 % rise and fall time were

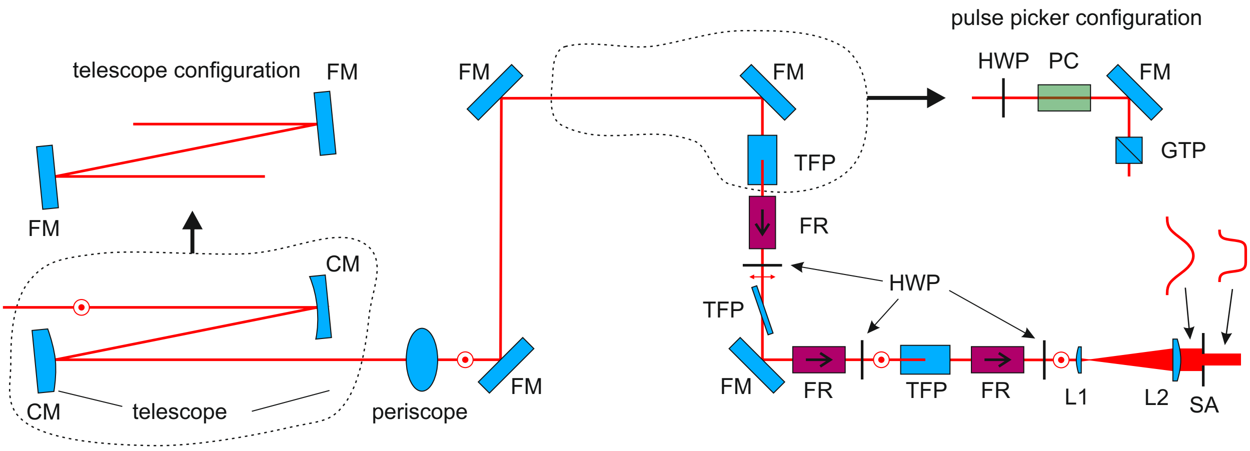

**Figure 6.14:** Schematic layout of the beam path configuration changes for implementation of a fast pulse picker for improvement of the nanosecond contrast: FM - flat mirror, CM - curved mirror, TFP - thin film polarizer, FR - Faraday rotator, HWP - half-waveplate, L1 and L2 - plano-convex lenses, SA - serrated aperture, GTP - Glan-Taylor polarizer.

measured as 528 ps and 359 ps, respectively. The values are higher than the 250 ps specification for the combination of the high voltage driver and the Pockel's cell. The fast part of the rising edge could be assumed if the modulation of the stretched pulse spectrum due to the slow part of the rising edge was compensated by the dazzler 2. The measurement also indicates that the Pockel's cell does not fully close after the falling edge. The principle of operation of the Leysop UPC Pockel's cell is shown schematically in figure 6.15a. The Pockel's cell contains two DKDP crystals, and each of the crystals is connected to one of the two high voltage outputs of the driver. The driver generates a fast voltage step (approximatelly 250 ps) followed by a very slow decay to 0 V. The two cables connecting the DKDP crystals to the driver have lengths $l_1$ and $l_2$. The high voltage steps arrive to the two crystals with a delay $\Delta t$ corresponding to the difference in the cable lengths. In ideal case, the voltage applied to each crystal should be equal to the half-wave voltage $U_\pi$. The reason for the pulse picker transmission not fully returning to the initial value is a difference in the voltage applied to each crystal. As a result, any post-pulses from the front-end are not fully reduced by the pulse picker. The post pulses are not impacting the target in the experiments.

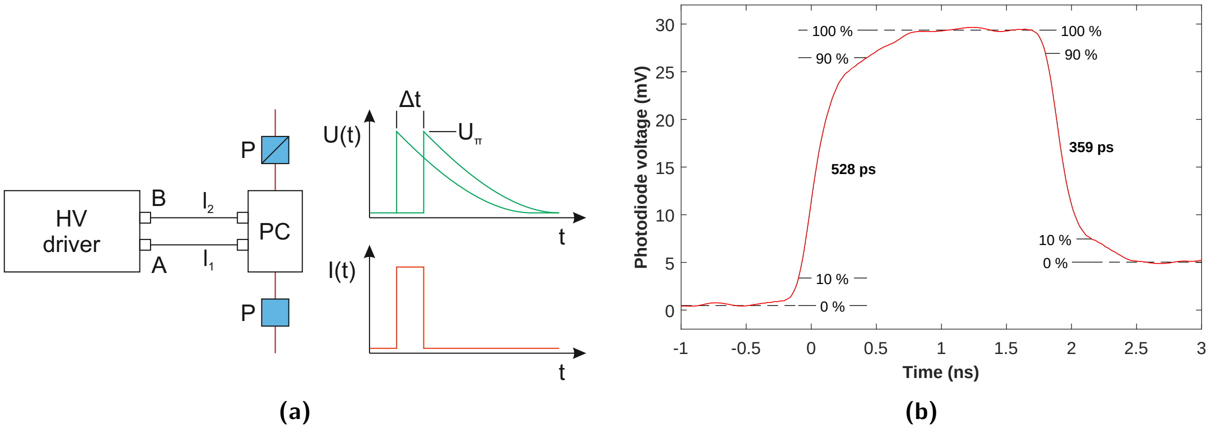

**Figure 6.15:** Operating principle of the fast Pockel's cell (Leysop UPC) (a), and measurement of the Pockel's cell rise and fall time (b).

For the jitter measurement, the transmission window of the Pockel's cell was moved onto the ASE in front of the Pulse by adjusting the trigger delay for the high voltage driver. The jitter was measured using a fast photodiode and oscilloscope. The main pulse was partially transmitted by the pulse picker due to the imbalance of the high voltages applied to the Pockel's cell crystals. The oscilloscope was triggered from the main pulse. The resulting oscilloscope trace with persistence measured over 1 minute is shown in figure 6.16. The vertical markers indicate the expected minimum and maximum duration of the residual rising ASE pedestal after the pulse picker, and the duration of the effective high transmission window. Setting the rising edge of the Pockel's cell closer to the pulse would have negative impact on the stability of the rising edge of the stretched pulse. The transmission window of the pulse picker is 1.2 ns with the cable length difference of 40 cm. The stretched pulse has a duration of 600-700 ps, depending on the bandwidth set by the dazzler 2.

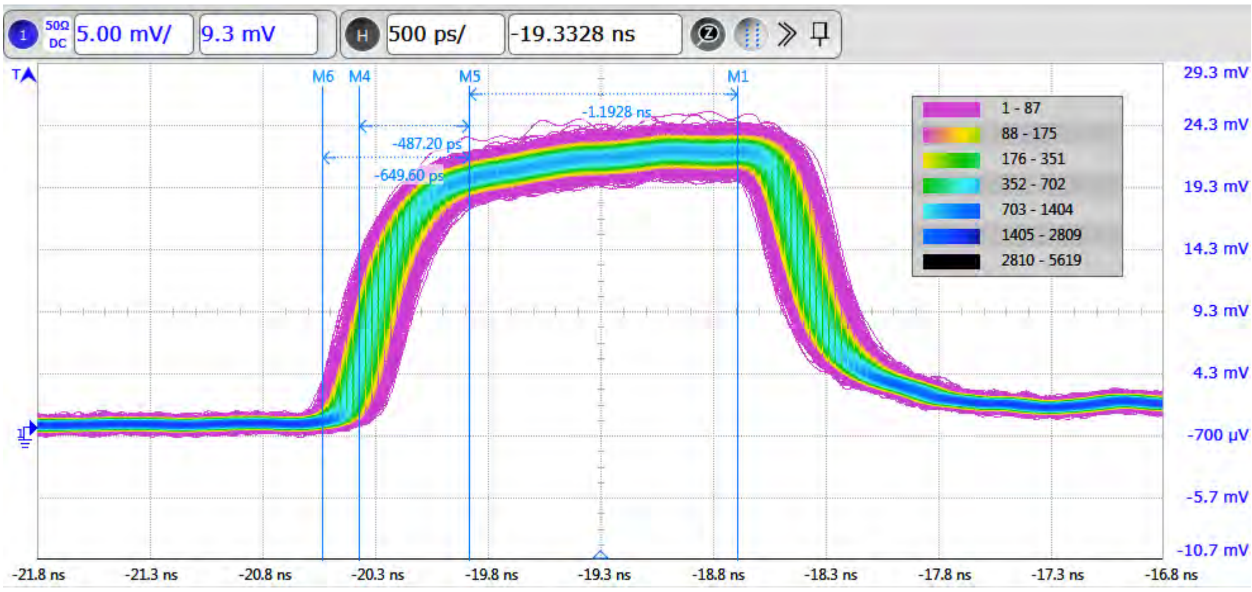

**Figure 6.16:** Jitter measurement of the fast pulse picker with respect to the front-end output laser pulse. The markers show minimum and maximum transmitted ASE pedestal and the duration of the Pockel's cell opening.

The characteristics of the rising pedestal with the fast pulse picker installed were measured in the same configuration as before the installation for comparison. The results of the measurements are shown in figure 6.17. The timing of the Pockel's cell rising edge was adjusted and the optimum position was found - see figure 6.17a. As the comparison between the ASE pedestal with and without the pulse picker indicates, significant reduction was achieved. The oscilloscope with the photodiode create a measurement artefact approximately 1 ns before the main pulse signal, which manifests as an oscillating voltage rise. This artefact decreases and increases in amplitude when increasing the vertical resolution of the oscilloscope channel, indicating that it is not a real signal from the photodiode.

The improvements of the nanosecond contrast proved critical for opening the potential of the L3-HAPLS laser to the user community, and for enabling high quality research. The reduction of pre-pulses and ASE improved the energy of accelerated protons in the E4-ELIMAIA experiment from original 3 MeV to 18 MeV. Preliminary measurements after installation of the fast pulse picker indicate additional improvement to 24 MeV before optimization of the proton source - see figure 6.18. The graph on the left shows the improvement of the ASE background measured by photodiode in the experimental setup in E4 at 10 J shot energy. The graph on the right shows the corresponding energy distribution of the integrated proton flux.

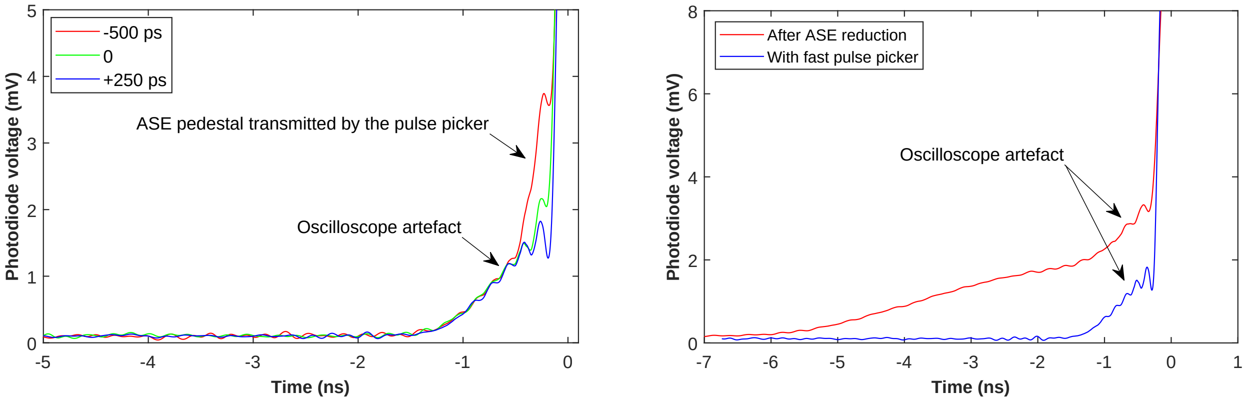

**(a)** **(b)**

**Figure 6.17:** Photodiode measurement of the improved rising ASE pedestal: (a) fast pulse picker timing optimization (b) comparison before and after fast pulse picker installation.

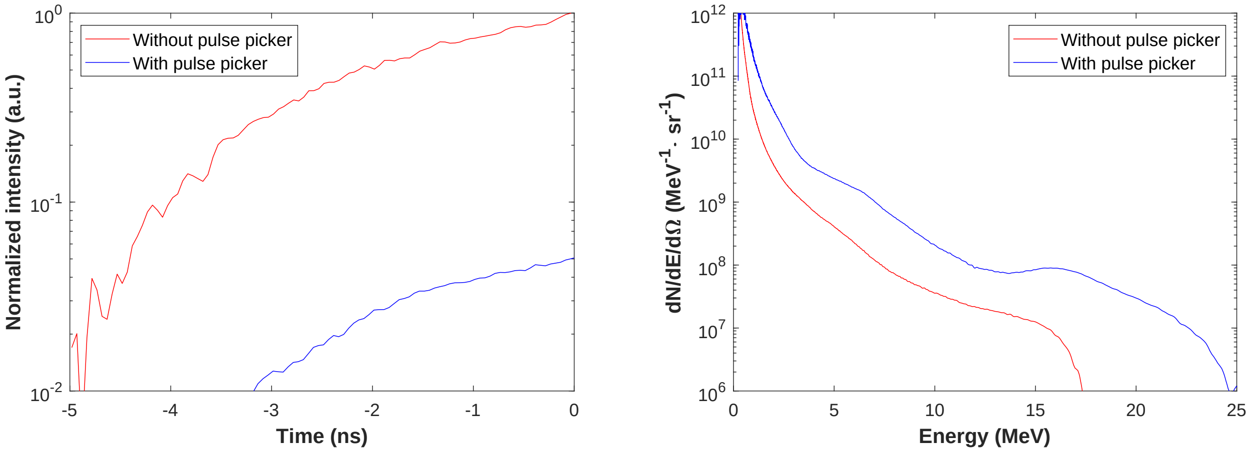

**Figure 6.18:** Improvement of the accelerated proton energy in the E4-ELIMAIA station with the installation of the fast pulse picker to reduce front-end ASE. ASE background measured at 10 J energy using a photodiode (left), energy distribution of the integrated proton flux (right). Graphs courtesy of the E4-ELIMAIA team.

## 6.3 Picosecond contrast measurements and planned improvements

Since the most impacting pre-pulses have been reduced and the ASE pedestal was reduced in time, the focus of the contrast improvements is shifting towards the picosecond contrast. The contrast within 200 ps before the main pulse was measured at the output of the commercial front-end and at the output of the main compressor. The results of the measurements are shown in figures 6.19 and 6.20. Both measurements were performed before the improvements of nanosecond contrast, and need to be repeated in order to capture the impact of those changes. It is expected that the installation of the fast pulse picker and the Glan-Taylor polarizer after XPW may introduce post-pulses due to double reflection. The measurement at the output of the compressor was performed at the full system output energy of approximately 1 J, which impacts especially the relative intensity of the pre-pulses depending on pulse energy and B-integral. The ASE background of the power amplifiers at full performance also remains to be evaluated by the Sequoia.

The first inset graph in figure 6.19 shows the dynamic range limit of the Sequoia, given by the PMT

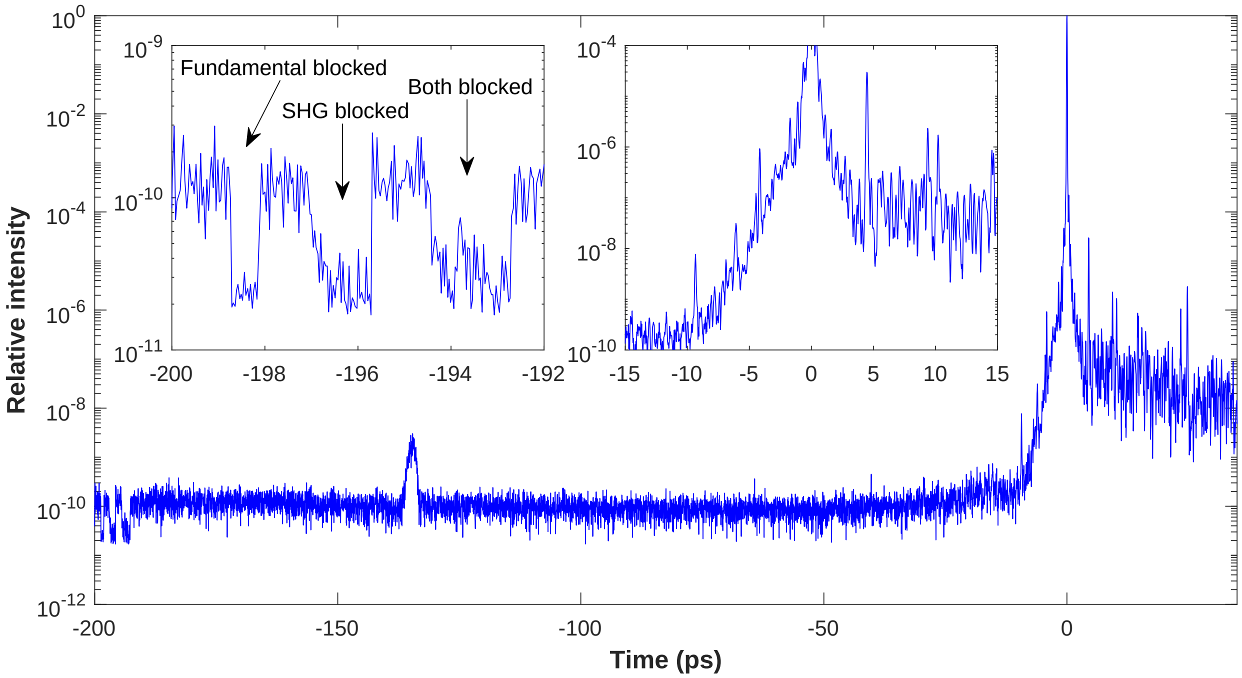

**Figure 6.19:** Sequoia measurement of the picosecond contrast of the L3-HAPLS laser front-end. The left-hand inset graph shows the noise floor of the photomultiplier tube (PMT), and the right-hand inset shows detail of the contrast close to the main pulse.

noise. The fundamental frequency beam, the second harmonic beam, and then the input beam to the Sequoia were blocked to measure the noise level and verify that the signal measured by the PMT is from the third harmonic sum frequency. The second inset shows the ±15 ps range around the main pulse. The picosecond coherent pedestal from stretcher gratings and mirrors decreases below $10^{-10}$ relative intensity within 10 ps, which is an excellent result. The measurement indicates a presence of ASE with the relative intensity of $1{\cdot}10^{-10}$. Several pre-pulses are present within 10 ps from the main pulse. The pre-pulse signal at -135 ps requires additional investigation, mainly due to its large delay and significant energy content.

Figure 6.20 shows the measured contrast at the output of the main compressor. Several additional pre-pulses are present around -60 ps and between -30 ps and -40 ps (see the left-hand inset graph). Their relative intensity at full system performance needs to be evaluated. The comparison of the two measurements - the front end and the full system output - is shown in figure 6.21, indicating that most of the pre-pulses are originating in the front-end. Further investigation of the picosecond contrast and removing remaining pre-pulses impacting the laser-matter interaction are the next steps in preparation for offering the L3-HAPLS experimental capabilities to the international user community.

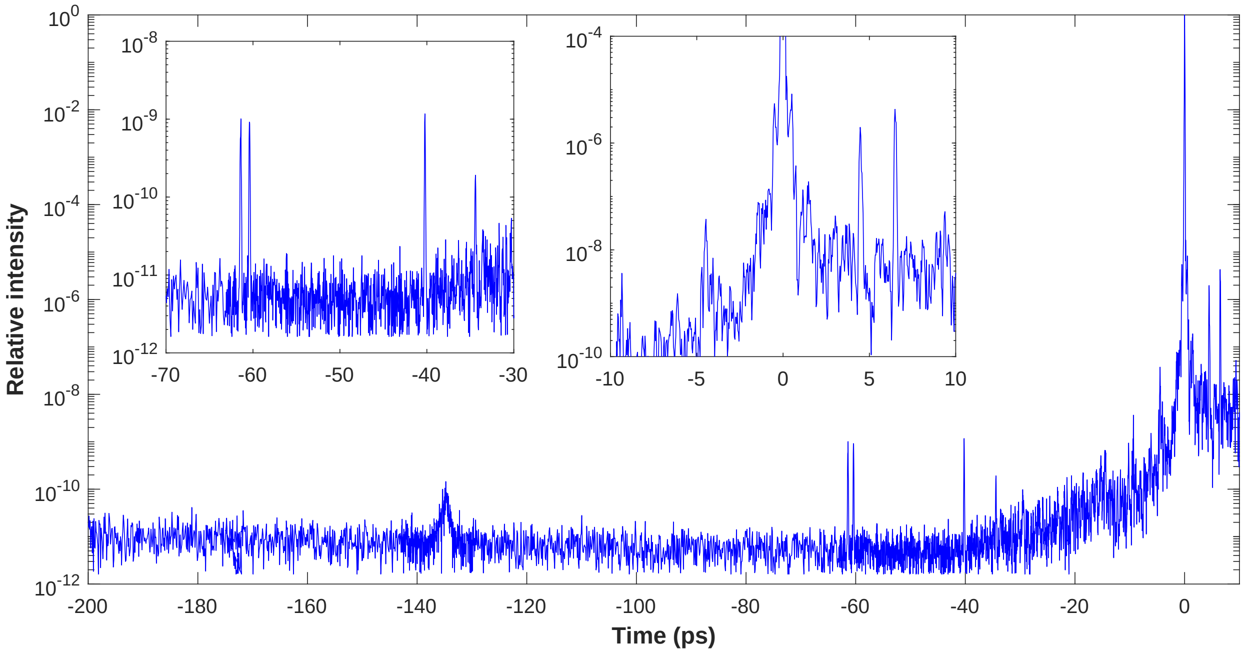

**Figure 6.20:** Sequoia measurement of the picosecond contrast after the L3-HAPLS laser compressor. The insets show in detail selected areas of the contrast.

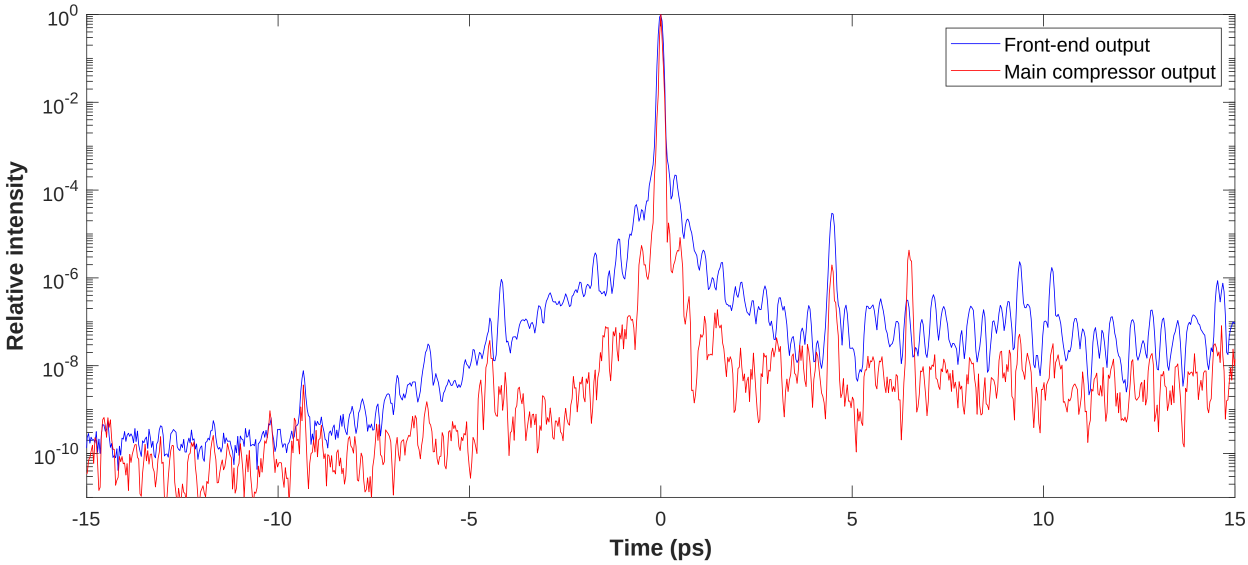

**Figure 6.21:** Comparison of the picosecond contrast at the output of the front-end and main compressor, measured by Sequoia.

# Conclusions

The pre-pulse contrast is an important characteristic of the high-focused-intensity lasers. It has similar significance for the laser-matter interaction experiments as the focusability of the laser beam and compressibility of the laser pulse. These parameters together define the limitations on the quality of research that can be done with the laser system. It is therefore a priority of every facility focusing on research and applications of ultra-relativistic interactions to ensure that their laser systems are competitive and offer to the users unique parameters.

The ELI Beamlines facility is currently in the phase of commissioning of the experimental infrastructure with the lasers developed in house and purchased from external suppliers. One of the laser systems is the L3-HAPLS laser - an all-diode pumped repetition rate petawatt laser. This laser is the first Ti:sapphire laser system utilizing multi-slab architecture for efficient cooling of the final amplifier. The study of the impact of multiple birefringent crystals in the laser head on the pre-pulse contrast, conducted within this thesis, provides an important insight for future development of this technology. The improvements of the initial pre-pulse contrast of the L3-HAPLS laser system are contributing to the quality of future research at ELI Beamlines.

## Summary of the main results

The primary goal of this thesis was to investigate the impact of birefringence in the gain media of high-focused-intensity CPA laser systems on the pre-pulse contrast performance. A numerical model was prepared to calculate this impact. The model was benchmarked with the measured pulse energy data of the L3-HAPLS power amplifiers, and the implementation of the numerical model was verified by comparing calculated data with measurements of pre-pulse contrast of the L3-HAPLS laser system with an artificially introduced post-pulse from a Ti:sapphire slab. This comparison confirmed that misalignment of the birefringent gain medium produces post-pulses at an expected delay given by the difference in group velocities and thickness of the birefringent medium, and that the presence of such post-pulses leads to generation of pre-pulses due to modulation of spectral phase.

The benchmarked and validated numerical model was used to calculate the impact of different imperfections in power amplifiers of the L3-HAPLS laser system. The first result of the calculation for system with ideal alignment showed the impact of wavelength-dependent phase retardation in waveplates and in Pockel's cells. Polarization component orthogonal to the main pulse polarization is generated, which is subsequently delayed in the amplifier gain medium and produces a post-pulse. If the system contains misalignments, this post-pulse superimposes with the main pulse and produces a corresponding pre-pulse. Rotation of polarization in the telescopes for relay-imaging and multiplexing of the amplification passes, misalignment of individual slabs in multiple-slab amplifier head configuration, and inhomogeneity of c-axis direction in the gain medium all lead to generation of pre-pulses. The nature of the origin of such pre-pulses limits their delay with respect to the main pulse - the maximum delay is given by the total length of the gain medium traversed by the seed pulse in all amplification passes, and by the difference in group velocity for ordinary and extraordinary wave at the laser wavelength. For power amplifiers utilizing Ti:sapphire, the pre-pulses from birefringence occur within 10 ps in front of the main pulse for the typical lengths of the gain media. The relative intensity contrast of pre-pulses from birefringence depends on the relative intensity of the corresponding post-pulses and on the B-integral accumulated during propagation through the amplifier system. The post-pulse is generated through a cascaded process of depolarization and subsequent re-combination of the polarization components, as shown in figure 3.3. The relative intensity of the post-pulse is therefore a combination of misalignment in both steps of this process. For small misalignemtns it is a product of the squares of the corresponding misalignment angles in radians. By this approach, an approximate equation for the expected pre-pulse contrast was identified that allows for estimation of the strongest pre-pulse intensity of an amplifier for given misalignment without the need for complicated modelling.

The c-axis direction in large aperture Ti:sapphire slabs for a final amplifier of a petawatt-class laser system was characterized by an extended cross-polarized imaging method developed as a part of this thesis. The results of this measurement confirmed presence of areas with variations of the c-axis direction originating from imperfection of the crystal growth. The impact of such imperfection on the contrast of the petawatt amplifier was evaluated with the numerical model. The presence of crystal domains impacts the contrast of a multi-slab amplifier especially for small overall misalignments, and it sets the minimum achievable pre-pulse intensity. The time delay of pre-pulses from inhomogeneity of c-axis direction is the same as for multi-slab misalignments. Their relative intensity is proportional to the relative size of the domain area with respect to the amplified beam, and to the offset angle of the c-axis with respect to the rest of the crystal. Placement of the slab with inhomogeneity within the multiple slabs plays an important role, and the calculations indicate that the impact of the domain is smaller when it is located in one of the outer slabs of the amplifier head.

The main conclusions from the evaluation of the impact of gain medium birefringence are following: in homogeneous single-crystal or perfectly aligned multi-slab amplifier systems, the intensity of pre-pulses from birefringence is driven by imperfection of phase retardation in waveplates and Pockel's cells together with polarization rotation in complex beam paths. The relative intensity depends on parameters of the laser system. In the model case of the L3-HAPLS laser, it is expected $<10^{-10}$ at 2 ps before the main pulse. The misalignment of multiple slabs and inhomogeneity of c-axis direction from crystal growth increase the pre-pulse intensity within 10 ps of the main pulse up to $5\cdot10^{-7}$ with individual slab misalignments $<1°$. The impact of the pre-pulses is lower than the impact of other pre-pulses in nanosecond and picosecond range, since the generated pre-plasma has significantly less time to expand. Depending on the strength of the coherent pedestal, the pre-pulses from birefringence may be below it's level.

The results of the numerical calculation and measurements were presented at the SPIE conference in Prague [B1], and published as a paper in the Applied Optics journal [A1].

The secondary goal was to improve the pre-pulse contrast of the L3-HAPLS laser system. The nanosecond contrast was investigated first, since it has higher impact due to longer pre-pulse delays. Three main contrast defects were identified - pre-pulse at -56 ns, pre-pulses within 10 ns in front of the main pulse, and a rising nanosecond pedestal.

The pre-pulse at -56 ns was identified to originate from scattering on surface micro-roughness defects from magneto-rheological finishing of the slabs in the Beta amplifier. A temporary solution to eliminate the impact was identified and implemented, limiting the relative intensity of the pre-pulse light in focal plane of the OAP in the experimental area to $<10^{-10}$. In addition to the pre-pulse, the scattering introduces significant loss in the amplifier, which reduces the output energy of the L3-HAPLS laser system, and stretches the requirements for the pump laser of the Beta amplifier. The final solution of the problems connected with the scattering is replacement of the amplifier crystals. The crystals characterized in chapter 4 are the most likely candidates to be re-polished and used as the replacement slabs for the Beta amplifier. The numerical model and measurement techniques developed in this thesis will be a valuable asset for the design of the replacement, and ensuring that the impact of birefringence on the pre-pulse contrast is minimized.

The pre-pulses and rising ASE pedestal within 10 ns before the main pulse originate in the commercial front-end. The intensity contrast of the pre-pulses was reduced by optimization of the performance of the XPW contrast cleaner. The ASE pedestal was reduced by removing coupling of ASE and optimizing the gain and loss of the second multi-pass amplifier of the front-end. A fast pulse picker with rise time of 300-400 ps was installed to reduce the extent of the rising pedestal in time. This improvement was verified by proton acceleration experiment in the E4 experimental hall.

The results of the investigation and mitigation of the nanosecond pre-pulse contrast defects on the L3-HAPLS laser system provided important improvements of the laser system performance, critical for enabling the laser-matter experiments and opening the experimental capacity to external users. The experience and expertise needed for making the necessary improvements on the laser system were gained from cooperation on the assembly and commissioning of the L3-HAPLS laser during a year-long business trip to the Lawrence Livermore National Laboratory [B4], and during re-commissioning of the laser after shipping to ELI Beamlines [B3].

## Contribution of the author

My contribution to the work presented in this thesis includes the following: I have derived the analytical expressions for the mirroring of post-pulses to pre-pulses using frequency domain approach rather than through the response functions presented in [15]. I have developed the numerical model and calculated the impact of birefringent media on pre-pulse contrast of the L3-HAPLS and similar laser systems. I have developed the method for extraction of the local crystallographic c-axis direction from measurements of a-cut uniaxial crystals between crossed polarizers, and performed the measurements of large aperture Ti:sapphire crystals. I have performed the investigation of the pre-pulse contrast of the L3-HAPLS laser system and implemented the improvements to reduce the pre-pulses and the ASE pedestal. Some of the improvements, such as the adjustment of the multiplexing of the Beta amplifier, were designed by me. Other improvements were consulted with my colleagues and with the designer of the front-end.

I have gained the required detailed knowledge of the L3-HAPLS laser system when I was contributing to the commissioning of the system at LLNL and at ELI Beamlines, and through the operation of the system for the first commissioning experiments. My main contribution to the development of the laser was the assembly and alignment of the optical components in the Beta amplifier, including the alignment and commissioning of the beam diagnostics.

Other work I performed during the doctoral studies, which is not related to the contrast of high-focused-intensity lasers, includes design, assembly, alignment, and testing of a femtosecond OPA system to generate 150 fs pulses at the wavelength of the L4 laser (1057 nm) for testing of diagnostics and laser-induced damage threshold (LIDT). The results of this work were presented at a conference [B5] by my colleague who finalized the characterization of the output pulse during my business trip to LLNL.

# Publications related to this work

## Articles in peer-reviewed journals

[A1] **J. Cupal**, T. Spinka, E. Sistrunk, B. Rus, and C. Häfner, "Temporal prepulse contrast degradation in high-intensity CPA lasers from anisotropy of amplifier gain media," Appl. Opt. **60**, 8408 (2021).

[A2] T. Chagovets, J. Viswanathan, M. Tryus, F. Grepl, A. Velyhan, S. Stanček, L. Giuffrida, F. Schillaci, **J. Cupal**, L. Koubíková, D. Garcia, J. Manzagol, P. Bonnay, F. Souris, D. Chatain, A. Girard, and D. Margarone, "A Cryogenic Hydrogen Ribbon for Laser Driven Proton Acceleration at Hz-level Repetition Rate," Front. Phys. **9** (2022).

[A3] M. Tryus, F. Grepl, T. Chagovets, A. Velyhan, L. Giuffrida, S. Stanček, V. Kantarelou, V. Istokskaia, F. Schillaci, M. Žáková, J. Pšikal, M. Nevrkla, C. Lazzarini, G. Grittani, L. Goncalves, M. Nawaz, **J. Cupal**, L. Koubíková, S. Buck, and D. Margarone, "TERESA Target Area at ELI Beamlines," Quantum Beam Sci. **4**, 37 (2020).

## Conference contributions

[B1] **J. Cupal**, T. Spinka, E. Sistrunk, B. Rus, and C. Haefner, "Temporal pre-pulse generation in high-intensity CPA lasers from imperfect domain orientation in anisotropic crystals," in *Short-pulse High-energy Lasers and Ultrafast Optical Technologies,* vol. 11034 P. Bakule and C. L. Haefner, eds., International Society for Optics and Photonics (SPIE, 2019), pp. 24 – 33.

[B2] C. L. Haefner, A. Bayramian, S. Betts, R. Bopp, S. Buck, **J. Cupal**, M. Drouin, A. Erlandson, J. Horáček, J. Horner, J. Jarboe, K. Kasl, D. Kim, E. Koh, L. Koubíková, W. Maranville, C. Marshall, D. Mason, J. Menapace, P. Miller, P. Mazurek, A. Naylon, J. Novák, D. Peceli, P. Rosso, K. Schaffers, E. Sistrunk, D. Smith, T. Spinka, J. Stanley, R. Steele, C. Stolz, T. Suratwala, S. Telford, J. Thoma, D. VanBlarcom, J. Weiss, and P. Wegner, "High average power, diode pumped petawatt laser systems: a new generation of lasers enabling precision science and commercial applications," in *Research Using Extreme Light: Entering New Frontiers with Petawatt-Class Lasers III,* vol. 10241 G. Korn and L. O. Silva, eds., International Society for Optics and Photonics (SPIE, 2017), pp. 1 – 5.

[B3] T. Spinka, E. Sistrunk, A. Bayramian, J. Armstrong, S. Baxamusa, S. Betts, D. Bopp, S. Buck, K. Charron, **J. Cupal**, R. Demaret, R. Deri, J.-M. Nicola, A. Erlandson, E. Fulkerson, C. Gates, J. Horner, J. Horáček, J. Jarboe, and C. Haefner, "Commissioning results of the world's first diode-pumped 10 Hz PW laser," in *2017 Conference on Lasers and Electro-Optics Europe European Quantum Electronics Conference (CLEO/Europe-EQEC),* (2017), pp. 1–1.

[B4] E. Sistrunk, T. Spinka, A. Bayramian, P. Armstrong, S. Baxamusa, S. Betts, D. Bopp, S. Buck, K. Charron, **J. Cupal**, R. Demaret, R. Deri, J.-M. Nicola, M. Drouin, A. Erlandson, S. Fulkerson, C. Gates, J. Horner, J. Horáček, and C. Haefner, "All Diode-Pumped, High-repetition-rate Advanced Petawatt Laser System (HAPLS)," in *Conference on Lasers and Electro-Optics,* (Optica Publishing Group, 2017), p. STh1L.2.

[B5] A. R. Meadows, **J. Cupal**, P. Hříbek, M. Ďurák, D. Kramer, and B. Rus, "Femtosecond optical parametric amplification in BBO and KTA driven by a Ti:sapphire laser for LIDT testing and diagnostic development," in *High-Power, High-Energy, and High-Intensity Laser Technology III,* vol. 10238 J. Hein, ed., International Society for Optics and Photonics (SPIE, 2017), pp. 16 – 25.

[B6] B. Rus, P. Bakule, D. Kramer, J. Naylon, J. Thoma, M. Fibrich, J. T. Green, J. C. Lagron, R. Antipenkov, J. Bartoníček, F. Batysta, R. Baše, R. Boge, S. Buck, **J. Cupal**, M. A. Drouin, M. Ďurák, B. Himmel, T. Havlíček, P. Homer, A. Honsa, M. Horáček, P. Hríbek, J. Hubáček, Z. Hubka, G. Kalinchenko, K. Kasl, L. Indra, P. Korous, M. Košelja, L. Koubíková, M. Laub, T. Mazanec, A. Meadows, J. Novák, D. Peceli, J. Polan, D. Snopek, V. Šobr, P. Trojek, B. Tykalewicz, P. Velpula, E. Verhagen, Vyhlídka, J. Weiss, C. Haefner, A. Bayramian, S. Betts, A. Erlandson, J. Jarboe, G. Johnson, J. Horner, D. Kim, E. Koh, C. Marshall, D. Mason, E. Sistrunk, D. Smith, T. Spinka, J. Stanley, C. Stolz, T. Suratwala, S. Telford, T. Ditmire, E. Gaul, M. Donovan, C. Frederickson, G. Friedman, D. Hammond, D. Hidinger, G. Chériaux, A. Jochmann, M. Kepler, C. Malato, M. Martinez, T. Metzger, M. Schultze, P. Mason, K. Ertel, A. Lintern, C. Edwards, C. Hernandez-Gomez, and J. Collier, "ELI-beamlines: progress in development of next generation short-pulse laser systems," in *Research Using Extreme Light: Entering New Frontiers with Petawatt-Class Lasers III,* vol. 10241 G. Korn and L. O. Silva, eds., International Society for Optics and Photonics (SPIE, 2017), pp. 14 – 21.

[B7] M. Ďurák, P. K. Velpula, D. Kramer, **J. Cupal**, T. Medřík, J. Hřebíček, J. Golasowski, D. Peceli, M. Kozlová, and B. Rus, "Laser-induced damage threshold tests of ultrafast multilayer dielectric coatings in various environmental conditions relevant for operation of ELI beamlines laser systems," (SPIE, 2016), pp. 1 – 6.

[B8] M. Ďurák, D. Kramer, P. K. Velpula, A. R. Meadows, **J. Cupal**, and B. Rus, "Comparison of different LIDT testing protocols for PW and multi-PW class high-reflectivity coatings," in *Laser-Induced Damage in Optical Materials 2016,* vol. 10014 G. J. Exarhos, V. E. Gruzdev, J. A. Menapace, D. Ristau, and M. Soileau, eds., International Society for Optics and Photonics (SPIE, 2016), pp. 70 – 82.

[B9] M. Ďurák, D. Kramer, P. K. Velpula, **J. Cupal**, T. Medřík, J. Hřebíček, J. Golasowski, D. Peceli, L. Fekete, V. Štepán, M. Kozlová, and B. Rus, "Ultrafast beam dump materials and mirror coatings tested with the ELI beamlines LIDT test station," in *Laser-Induced Damage in Optical Materials: 2015,* vol. 9632 G. J. Exarhos, V. E. Gruzdev, J. A. Menapace, D. Ristau, and M. Soileau, eds., International Society for Optics and Photonics (SPIE, 2015), pp. 254 – 265.

# References

[1] National Academies of Sciences, Engineering, and Medicine, *Opportunities in Intense Ultrafast Lasers: Reaching for the Brightest Light*.

[2] W. Sibbett, A. A. Lagatsky, and C. T. A. Brown, "The development and application of femtosecond laser systems," Opt. Express **20**, 6989–7001 (2012).

[3] C. M. Brenner, S. R. Mirfayzi, D. R. Rusby, C. Armstrong, A. Alejo, L. A. Wilson, R. Clarke, H. Ahmed, N. M. H. Butler, D. Haddock, A. Higginson, A. McClymont, C. Murphy, M. Notley, P. Oliver, R. Allott, C. Hernandez-Gomez, S. Kar, P. McKenna, and D. Neely, "Laser-driven x-ray and neutron source development for industrial applications of plasma accelerators," Plasma Phys. Control. Fusion **58**, 014039 (2016).

[4] A. Macchi, M. Borghesi, and M. Passoni, "Ion acceleration by superintense laser-plasma interaction," Rev. Mod. Phys. **85**, 751–793 (2013).

[5] H. Daido, M. Nishiuchi, and A. S. Pirozhkov, "Review of laser-driven ion sources and their applications," Reports on Prog. Phys. **75**, 056401 (2012).

[6] J. W. Yoon, Y. G. Kim, I. W. Choi, J. H. Sung, H. W. Lee, S. K. Lee, and C. H. Nam, "Realization of laser intensity over $10^{23}$ W/cm$^2$," Optica **8**, 630–635 (2021).

[7] D. Raffestin, L. Lecherbourg, I. Lantuéjoul, B. Vauzour, P. E. Masson-Laborde, X. Davoine, N. Blanchot, J. L. Dubois, X. Vaisseau, E. d'Humières, L. Gremillet, A. Duval, C. Reverdin, B. Rosse, G. Boutoux, J. E. Ducret, C. Rousseaux, V. Tikhonchuk, and D. Batani, "Enhanced ion acceleration using the high-energy petawatt PETAL laser," Matter Radiat. at Extrem. **6**, 056901 (2021).

[8] D. Margarone, G. A. P. Cirrone, G. Cuttone, A. Amico, L. Andò, M. Borghesi, S. S. Bulanov, S. V. Bulanov, D. Chatain, A. Fajstavr, L. Giuffrida, F. Grepl, S. Kar, J. Krasa, D. Kramer, G. Larosa, R. Leanza, T. Levato, M. Maggiore, L. Manti, G. Milluzzo, B. Odlozilik, V. Olsovcova, J.-P. Perin, J. Pipek, J. Psikal, G. Petringa, J. Ridky, F. Romano, B. Rus, A. Russo, F. Schillaci, V. Scuderi, A. Velyhan, R. Versaci, T. Wiste, M. Zakova, and G. Korn, "ELIMAIA: A Laser-Driven Ion Accelerator for Multidisciplinary Applications," Quantum Beam Sci. **2** (2018).

[9] J. Badziak, "Laser-driven ion acceleration: methods, challenges and prospects," J. Physics: Conf. Ser. **959**, 012001 (2018).

[10] W. Bang, B. I. Cho, M. H. Cho, M. S. Cho, M. Chung, M. S. Hur, G. Kang, K. Kang, T. Kang, C. Kim, H. N. Kim, J. Kim, K. B. Kim, K. N. Kim, M. Kim, M. S. Kim, M. Kumar, H. Lee, H. W. Lee, K. Lee, I. Nam, S. H. Park, V. Phung, W. J. Ryu, S. Y. Shin, H. S. Song, J. Song, J. Won, and H. Suk, "Review of laser-plasma physics research and applications in Korea," J. Korean Phys. Soc. (2022).

[11] D. Neely, P. Foster, A. Robinson, F. Lindau, O. Lundh, A. Persson, C. Wahlstrom, and P. Mckenna, "Enhanced proton beams from ultrathin targets driven by high contrast laser pulses," Appl. Phys. Lett. **89** (2006).

[12] S. Mangles, A. Thomas, M. Kaluza, O. Lundh, F. Lindau, A. Persson, Z. Najmudin, C. Wahlstrom, C. Murphy, C. Kamperidis, K. Lancaster, E. Divall, and K. Krushelnick, "Effect of laser contrast ratio on electron beam stability in laser wakefield acceleration experiments," Plasma Phys. Control. Fusion **48** (2006).

[13] A. Flacco, T. Ceccotti, H. George, P. Monot, P. Martin, F. Réau, O. Tcherbakoff, P. d'Oliveira, F. Sylla, M. Veltcheva, F. Burgy, A. Tafzi, V. Malka, and D. Batani, "Comparative study of laser ion acceleration with different contrast enhancement techniques," Nucl. Instruments Methods Phys. Res. Sect. A: Accel. Spectrometers, Detect. Assoc. Equip. **620**, 18 – 22 (2010).

[14] C. Hooker, Y. Tang, O. Chekhlov, J. Collier, E. Divall, K. Ertel, S. Hawkes, B. Parry, and P. P. Rajeev, "Improving coherent contrast of petawatt laser pulses," Opt. Express **19**, 2193–2203 (2011).

[15] N. Didenko, A. Konyaschenko, A. Lutsenko, and S. Tenyakov, "Contrast degradation in a chirped-pulse amplifier due to generation of prepulses by postpulses," Opt. Express **16**, 3178–3190 (2008).

[16] S. Keppler, A. Sävert, J. Koerner, M. Hornung, H. Liebetrau, J. Hein, and M. Kaluza, "The generation of amplified spontaneous emission in high-power CPA laser systems," Laser Photonics Rev. **10**, 264 (2016).

[17] L. E. Hargrove, R. L. Fork, and M. A. Pollack, "Locking of He–Ne Laser Modes Induced by Synchronous Intracavity Modulation," Appl. Phys. Lett. **5**, 4–5 (1964).

[18] M. DiDomenico, "Small-Signal Analysis of Internal (Coupling-Type) Modulation of Lasers," J. Appl. Phys. **35**, 2870–2876 (1964).

[19] A. Yariv, "Internal Modulation in Multimode Laser Oscillators," J. Appl. Phys. **36**, 388–391 (1965).

[20] D. Strickland and G. Mourou, "Compression of amplified chirped optical pulses," Opt. Commun. **56**, 219–221 (1985).

[21] M. D. Perry, D. Pennington, B. C. Stuart, G. Tietbohl, J. A. Britten, C. Brown, S. Herman, B. Golick, M. Kartz, J. Miller, H. T. Powell, M. Vergino, and V. Yanovsky, "Petawatt laser pulses," Opt. Lett. **24**, 160–162 (1999).

[22] "ICUIL world map of ultra-high intensity laser facilities," https://www.easymapmaker.com/map/ICUIL_World_Map_v3. Accessed: 2022-03-08.

[23] C. Danson, D. Hillier, N. Hopps, and D. Neely, "Petawatt class lasers worldwide," High Power Laser Sci. Eng. **3**, e3 (2015).

[24] C. N. Danson, C. Haefner, J. Bromage, T. Butcher, J.-C. F. Chanteloup, E. A. Chowdhury, A. Galvanauskas, L. A. Gizzi, J. Hein, D. I. Hillier, N. W. Hopps, Y. Kato, E. A. Khazanov, R. Kodama, G. Korn, R. Li, Y. Li, J. Limpert, J. Ma, C. H. Nam, D. Neely, D. Papadopoulos, R. R. Penman, L. Qian, J. J. Rocca, A. A. Shaykin, C. W. Siders, C. Spindloe, S. Szatmári, R. M. G. M. Trines, J. Zhu, P. Zhu, and J. D. Zuegel, "Petawatt and exawatt class lasers worldwide," High Power Laser Sci. Eng. **7**, e54 (2019).

[25] F. Lureau, G. Matras, O. Chalus, C. Derycke, T. Morbieu, C. Radier, O. Casagrande, S. Laux, S. Ricaud, G. Rey, and et al., "High-energy hybrid femtosecond laser system demonstrating 2 × 10 PW capability," High Power Laser Sci. Eng. **8**, e43 (2020).

[26] T. M. Spinka and C. Haefner, "High-Average-Power Ultrafast Lasers," Opt. Photon. News **28**, 26–33 (2017).

[27] G. Cheriaux, P. Rousseau, F. Salin, J. P. Chambaret, B. Walker, and L. F. Dimauro, "Aberration-free stretcher design for ultrashort-pulse amplification," Opt. Lett. **21**, 414–416 (1996).

[28] E. Treacy, "Optical pulse compression with diffraction gratings," IEEE J. Quantum Electron. **5**, 454–458 (1969).

[29] P. F. Moulton, "Spectroscopic and laser characteristics of Ti:$Al_2O_3$," J. Opt. Soc. Am. B **3**, 125–133 (1986).

[30] D. B. Joyce and F. Schmid, "Progress in the growth of large scale Ti:sapphire crystals by the heat exchanger method (HEM) for petawatt class lasers," J. Cryst. Growth **312**, 1138 – 1141 (2010).

[31] F. Batysta, R. Antipenkov, T. Borger, A. Kissinger, J. T. Green, R. Kananavičius, G. Chériaux, D. Hidinger, J. Kolenda, E. Gaul, B. Rus, and T. Ditmire, "Spectral pulse shaping of a 5 Hz, multi-joule, broadband optical parametric chirped pulse amplification frontend for a 10 PW laser system," Opt. Lett. **43**, 3866–3869 (2018).

[32] G. Cheriaux, R. Antipenkov, F. Batysta, T. Borger, G. Friedman, J. Green, D. Hammond, J. Heisler, A. Jochmann, and M. Kepler, "Progress on ELI-Beamlines 10 PW Laser System," The Rev. Laser Eng. **46**, 125 (2018).

[33] M. Hornung, H. Liebetrau, S. Keppler, A. Kessler, M. Hellwing, F. Schorcht, G. A. Becker, M. Reuter, J. Polz, J. Körner, J. Hein, and M. C. Kaluza, "54 J pulses with 18 nm bandwidth from a diode-pumped chirped-pulse amplification laser system," Opt. Lett. **41**, 5413–5416 (2016).

[34] M. Siebold, F. Roeser, M. Loeser, D. Albach, and U. Schramm, "PEnELOPE: a high peak-power diode-pumped laser system for laser-plasma experiments," in *High-Power, High-Energy, and High-Intensity Laser Technology; and Research Using Extreme Light: Entering New Frontiers with Petawatt-Class Lasers,* vol. 8780 G. Korn, L. O. Silva, and J. Hein, eds., International Society for Optics and Photonics (SPIE, 2013), pp. 31 – 44.

[35] D. Albach, M. Loeser, M. Siebold, and U. Schramm, "Performance demonstration of the PEnELOPE main amplifier HEPA I using broadband nanosecond pulses," High Power Laser Sci. Eng. **7**, e1 (2019).

[36] F. Lureau, G. Matras, O. Chalus, C. Derycke, C. Radier, O. Casagrande, S. Ricaud, and C. S. Boisson, "10 PetaWatt Laser System for Extreme Light Physics," in *OSA High-brightness Sources and Light-driven Interactions Congress 2020 (EUVXRAY, HILAS, MICS),* (Optical Society of America, 2020), p. HTh2B.3.

[37] J. H. Sung, S. K. Lee, T. J. Yu, T. M. Jeong, and J. Lee, "0.1 Hz 1.0 PW Ti:sapphire laser," Opt. Lett. **35**, 3021–3023 (2010).

[38] T. J. Yu, S. K. Lee, J. H. Sung, J. W. Yoon, T. M. Jeong, and J. Lee, "Generation of high-contrast, 30 fs, 1.5 PW laser pulses from chirped-pulse amplification Ti:sapphire laser," Opt. Express **20**, 10807–10815 (2012).

[39] J. H. Sung, H. W. Lee, J. Y. Yoo, J. W. Yoon, C. W. Lee, J. M. Yang, Y. J. Son, Y. H. Jang, S. K. Lee, and C. H. Nam, "4.2 PW, 20 fs Ti:sapphire laser at 0.1 Hz," Opt. Lett. **42**, 2058–2061 (2017).

[40] Z. Gan, L. Yu, S. Li, C. Wang, X. Liang, Y. Liu, W. Li, Z. Guo, Z. Fan, X. Yuan, L. Xu, Z. Liu, Y. Xu, J. Lu, H. Lu, D. Yin, Y. Leng, R. Li, and Z. Xu, "200 J high efficiency Ti:sapphire chirped pulse amplifier pumped by temporal dual-pulse," Opt. Express **25**, 5169–5178 (2017).

[41] H. Kiriyama, A. S. Pirozhkov, M. Nishiuchi, Y. Fukuda, K. Ogura, A. Sagisaka, Y. Miyasaka, M. Mori, H. Sakaki, N. P. Dover, K. Kondo, J. K. Koga, T. Z. Esirkepov, M. Kando, and K. Kondo, "High-contrast high-intensity repetitive petawatt laser," Opt. Lett. **43**, 2595–2598 (2018).

[42] R. W. Boyd, "Chapter 1 - The Nonlinear Optical Susceptibility," in *Nonlinear Optics (Third Edition),* R. W. Boyd, ed. (Academic Press, Burlington, 2008), pp. 1–67, third edition ed.

[43] N. Stuart, D. Bigourd, R. Hill, T. Robinson, K. Mecseki, S. Patankar, G. New, and R. Smith, "Direct fluorescence characterisation of a picosecond seeded optical parametric amplifier," Opt. Commun. **336**, 319–325 (2015).

[44] S. Luan, M. H. R. Hutchinson, R. A. Smith, and F. Zhou, "High dynamic range third-order correlation measurement of picosecond laser pulse shapes," Meas. Sci. Technol. **4**, 1426–1429 (1993).

[45] F. Tavella, K. Schmid, N. Ishii, A. Marcinkevičius, L. Veisz, and F. Krausz, "High-dynamic range pulse-contrast measurements of a broadband optical parametric chirped-pulse amplifier," Appl. Phys. B **81**, 753–756 (2005).

[46] V. A. Schanz, F. Wagner, M. Roth, and V. Bagnoud, "Noise reduction in third order cross-correlation by angle optimization of the interacting beams," Opt. Express **25**, 9252–9261 (2017).

[47] Y. Wang, J. Ma, J. Wang, P. Yuan, G. Xie, X. Ge, F. Liu, X. Yuan, H. Zhu, and L. Qian, "Single-shot measurement of $>10^{10}$ pulse contrast for ultra-high peak-power lasers," Sci. Reports **4**, 3818 (2014).

[48] A. Jullien, A. Ricci, F. Böhle, J.-P. Rousseau, S. Grabielle, N. Forget, H. Jacqmin, B. Mercier, and R. Lopez-Martens, "Carrier-envelope-phase stable, high-contrast, double chirped-pulse-amplification laser system," Opt. Lett. **39**, 3774–3777 (2014).

[49] A. Jullien, S. Kourtev, O. Albert, G. Cheriaux, J. Etchepare, N. Minkovski, and S. Saltiel, "Highly efficient temporal cleaner for femtosecond pulses based on cross-polarized wave generation in a dual crystal scheme," Appl. Phys. B **84**, 409–414 (2006).

[50] A. Ricci, A. Jullien, J.-P. Rousseau, Y. Liu, A. Houard, P. Ramirez, D. Papadopoulos, A. Pellegrina, P. Georges, F. Druon, N. Forget, and R. Lopez-Martens, "Energy-scalable temporal cleaning device for femtosecond laser pulses based on cross-polarized wave generation," Rev. Sci. Instrum. **84**, 043106 (2013).

[51] L. P. Ramirez, D. Papadopoulos, M. Hanna, A. Pellegrina, F. Friebel, P. Georges, and F. Druon, "Compact, simple, and robust cross polarized wave generation source of few-cycle, high-contrast pulses for seeding petawatt-class laser systems," J. Opt. Soc. Am. B **30**, 2607–2614 (2013).

[52] A. Yogo, K. Kondo, M. Mori, H. Kiriyama, K. Ogura, T. Shimomura, N. Inoue, Y. Fukuda, H. Sakaki, S. Jinno, M. Kanasaki, and P. R. Bolton, "Insertable pulse cleaning module with a saturable absorber pair and a compensating amplifier for high-intensity ultrashort-pulse lasers," Opt. Express **22**, 2060–2069 (2014).

[53] C. Liu, Z. Wang, W. Li, Q. Zhang, H. Han, H. Teng, and Z. Wei, "Contrast enhancement in a Ti:sapphire chirped-pulse amplification laser system with a noncollinear femtosecond optical-parametric amplifier," Opt. Lett. **35**, 3096–3098 (2010).

[54] U. Teubner, U. Wagner, and E. Förster, "Sub-10 fs gating of optical pulses," J. Phys. B: At. Mol. Opt. Phys. **34**, 2993–3002 (2001).

[55] C. Thaury, F. Quéré, J.-P. Geindre, A. Levy, T. Ceccotti, P. Monot, M. Bougeard, F. Réau, P. d'Oliveira, P. Audebert, R. Marjoribanks, and P. Martin, "Plasma mirrors for ultrahigh-intensity optics," Nat. Phys. **3**, 424 (2007).

[56] S. Inoue, K. Maeda, S. Tokita, K. Mori, K. Teramoto, M. Hashida, and S. Sakabe, "Single plasma mirror providing $10^4$ contrast enhancement and 70% reflectivity for intense femtosecond lasers," Appl. Opt. **55**, 5647–5651 (2016).

[57] D. E. Rivas, A. Borot, D. E. Cardenas, G. Marcus, X. Gu, D. Herrmann, J. Xu, J. Tan, D. Kormin, G. Ma, W. Dallari, G. D. Tsakiris, I. B. Földes, S. W. Chou, M. Weidman, B. Bergues, T. Wittmann, H. Schröder, P. Tzallas, D. Charalambidis, O. Razskazovskaya, V. Pervak, F. Krausz, and L. Veisz, "Next Generation Driver for Attosecond and Laser-plasma Physics," Sci. Reports **7**, 5224 (2017).

[58] I. W. Choi, C. Jeon, S. G. Lee, S. Y. Kim, T. Y. Kim, I. J. Kim, H. W. Lee, J. W. Yoon, J. H. Sung, S. K. Lee, and C. H. Nam, "Highly efficient double plasma mirror producing ultrahigh-contrast multi-petawatt laser pulses," Opt. Lett. **45**, 6342–6345 (2020).

[59] R. Trebino, K. DeLong, D. Fittinghoff, J. Sweetser, M. Krumbuegel, B. Richman, and D. Kane, "Mesuring Ultrashort Laser Pulses in the Time-frequency Domain using Frequency-resolved Optical Gating," Rev. Sci. Instruments **68**, 3277–3295 (1997).

[60] J. Čtyroký, "Základy krystalooptiky," Podklady k přednáškám (2014).

[61] M. Bass, C. DeCusatis, J.M.Enoch, V. Lakshminarayanan, G. Li, C. MacDonald, V.N.Mahajan, and E. Van Stryland, *Handbook of Optics*, vol. 5 (2010), 3rd ed.

[62] W. Koechner, *Solid-State Laser Engineering*, Springer Series in Optical Sciences (Springer, New York, NY, 2006), 6th ed.

[63] V. Parfenov, V. Shashkin, and E. Stepanov, "Numerical investigation of thermally induced birefringence in optical elements of solid-state lasers," Appl. Opt. **32**, 5243–5255 (1993).

[64] M. Ostermeyer, D. Mudge, P. J. Veitch, and J. Munch, "Thermally induced birefringence in Nd:YAG slab lasers," Appl. Opt. **45**, 5368–5376 (2006).

[65] M. D. Vido, P. D. Mason, M. Fitton, R. W. Eardley, G. Quinn, D. Clarke, K. Ertel, T. J. Butcher, P. J. Phillips, S. Banerjee, J. Smith, J. Spear, C. Edwards, and J. L. Collier, "Modelling and measurement of thermal stress-induced depolarisation in high energy, high repetition rate diode-pumped Yb:YAG lasers," Opt. Express **29**, 5607–5623 (2021).

[66] X. Yin, M. Jiang, Z. Sun, Y. Hui, H. Lei, and Q. Li, "Effect of thermally induced birefringence on performance of KD*P electro-optics crystal with rectangular shape," Appl. Opt. **56**, 2893–2900 (2017).

[67] Y. Lumer, I. Moshe, Z. Horovitz, S. Jackel, G. Machavariani, and A. Meir, "Thermally induced birefringence in nonsymmetrically pumped laser rods and its implications for attainment of good beam quality in high-power, radially polarized lasers," Appl. Opt. **47**, 3886–3891 (2008).

[68] S. Cho, J. Jeong, and T. J. Yu, "Jones calculus modeling and analysis of the thermal distortion in a Ti:sapphire laser amplifier," Opt. Express **24**, 14362–14373 (2016).

[69] J. Jeong, S. Cho, S. Hwang, B. Lee, and T. J. Yu, "Modeling and Analysis of High-Power Ti:sapphire Laser Amplifiers–A Review," Appl. Sci. **9** (2019).

[70] J. Goodman, *Introduction to Fourier Optics*, Electrical Engineering Series (McGraw-Hill, 1996).

[71] G. N. Lawrence, *Optical Modeling*, vol. 11 of *Applied optics and optical engineering* (Academic Press, 1992).

[72] P. Tournois, "Acousto-optic programmable dispersive filter for adaptive compensation of group delay time dispersion in laser systems," Opt. Commun. **140**, 245–249 (1997).

[73] F. Verluise, V. Laude, Z. Cheng, C. Spielmann, and P. Tournois, "Amplitude and phase control of ultrashort pulses by use of an acousto-optic programmable dispersive filter:pulse compression and shaping," Opt. Lett. **25**, 575–577 (2000).

[74] D. F. Edwards and R. H. White, "Potassium Dihydrogen Phosphate ($KH_2PO_4$, KDP) and Three of Its Isomorphs," in *Handbook of Optical Constants of Solids,* E. D. Palik, ed. (Academic Press, Burlington, 1997), pp. 1005–1020.

[75] M. Akselrod and F. Bruni, "Modern trends in crystal growth and new applications of sapphire," J. Cryst. Growth **360**, 134–145 (2012).

[76] L. M. Frantz and J. S. Nodvik, "Theory of Pulse Propagation in a Laser Amplifier," J. Appl. Phys. **34**, 2346–2349 (1963).

[77] S. Bock, F. M. Herrmann, T. Püschel, U. Helbig, R. Gebhardt, J. Lötfering, R. Pausch, K. Zeil, T. Ziegler, A. Irman, T. Oksenhendler, A. Kon, M. Nishuishi, H. Kiriyama, K. Kondo, T. Toncian, and U. Schramm, "Characterization of Accumulated B-Integral of Regenerative Amplifier Based CPA Systems," Crystals **10** (2020).

[78] A. Bayramian, J. Armstrong, G. Beer, R. Campbell, B. Chai, R. Cross, A. Erlandson, Y. Fei, B. Freitas, R. Kent, J. Menapace, W. Molander, K. Schaffers, C. Siders, S. Sutton, J. Tassano, S. Telford, C. Ebbers, J. Caird, and C. Barty, "High-average-power femto-petawatt laser pumped by the Mercury laser facility," J. Opt. Soc. Am. B **25**, B57–B61 (2008).

[79] O. Svelto, S. Taccheo, and C. Svelto, "Analysis of amplified spontaneous emission: some corrections to the Linford formula," Opt. Commun. **149**, 277–282 (1998).

[80] G. J. Linford, E. R. Peressini, W. R. Sooy, and M. L. Spaeth, "Very Long Lasers," Appl. Opt. **13**, 379–390 (1974).

# Appendix A

# Dispersion properties of common optical materials

**Table A.1:** Material dispersion parameters of common materials used in petawatt-class lasers.

| Material, polarization | $D_0$ (rad/cm) | $D_1$ (rad/fs·cm) | $D_2$ (rad/fs$^2$·cm) | $D_3$ (rad/fs$^3$·cm) | $D_4$ (rad/fs$^4$·cm) |
|---|---|---|---|---|---|
| N-BK7 | $1.187\cdot10^5$ | $5.092\cdot10^4$ | $4.465\cdot10^2$ | $3.210\cdot10^2$ | $-1.060\cdot10^2$ |
| Fused silica | $1.141\cdot10^5$ | $4.894\cdot10^4$ | $3.616\cdot10^2$ | $2.750\cdot10^2$ | $-1.143\cdot10^2$ |
| SF11 | $1.386\cdot10^5$ | $6.042\cdot10^4$ | $18.750\cdot10^2$ | $12.400\cdot10^2$ | $3.830\cdot10^2$ |
| SF56 | $1.432\cdot10^5$ | $6.259\cdot10^4$ | $22.358\cdot10^2$ | $14.133\cdot10^2$ | $5.034\cdot10^2$ |
| DKDP, o | $1.177\cdot10^5$ | $5.059\cdot10^4$ | $3.531\cdot10^2$ | $3.732\cdot10^2$ | $-2.134\cdot10^2$ |
| DKDP, e | $1.148\cdot10^5$ | $4.916\cdot10^4$ | $3.741\cdot10^2$ | $2.500\cdot10^2$ | $-6.562\cdot10^1$ |
| Ti:Al$_2$O$_3$, o | $1.382\cdot10^5$ | $5.943\cdot10^4$ | $5.804\cdot10^2$ | $4.212\cdot10^2$ | $-1.556\cdot10^2$ |
| Ti:Al$_2$O$_3$, e | $1.376\cdot10^5$ | $5.915\cdot10^4$ | $5.663\cdot10^2$ | $4.140\cdot10^2$ | $-1.556\cdot10^2$ |
| MgF$_2$, o | $1.080\cdot10^5$ | $4.610\cdot10^4$ | $1.978\cdot10^2$ | $1.374\cdot10^2$ | $-0.504\cdot10^2$ |
| MgF$_2$, e | $1.089\cdot10^5$ | $4.651\cdot10^4$ | $2.055\cdot10^2$ | $1.441\cdot10^2$ | $-0.544\cdot10^2$ |
| SiO$_2$, o | $1.208\cdot10^5$ | $5.185\cdot10^4$ | $4.170\cdot10^2$ | $3.155\cdot10^2$ | $-1.301\cdot10^2$ |
| SiO$_2$, e | $1.216\cdot10^5$ | $5.213\cdot10^4$ | $4.576\cdot10^2$ | $2.910\cdot10^2$ | $-0.734\cdot10^2$ |
| CaCO$_3$, o | $1.295\cdot10^5$ | $5.584\cdot10^4$ | $7.809\cdot10^2$ | $5.417\cdot10^2$ | $-1.182\cdot10^2$ |
| CaCO$_3$, e | $1.164\cdot10^5$ | $4.979\cdot10^4$ | $3.964\cdot10^2$ | $2.106\cdot10^2$ | $-0.130\cdot10^2$ |